Alma Mater Studiorum – University of Bologna

SCHOOL OF SCIENCE
Department of Industrial Chemistry “Toso Montanari”

Second cycle degree in

Low Carbon Technologies and Sustainable Chemistry

Classe LM-71 - Scienze e Tecnologie della Chimica Industriale

Effect of preparation method on Indium-based materials, and their activity for CO_2 hydrogenation to methanol

Experimental degree thesis

CANDIDATE	**SUPERVISORS**
Giovanni Tizzanini	**Prof.** Patricia Benito Martin
	Prof. Louise Olsson

CO-SUPERVISORS

Prof. Derek Creaser, **Dr.** Phuoc Hoang Ho, **Dr.** Sreetama Ghosh

---

Academic Year 2020-2021

Abstract

Methanol synthesis through CO_2 hydrogenation reaction seems to be a promising approach to mitigate the excess of CO_2 anthropogenic emissions in the atmosphere and substitute the traditional syngas-based CH_3OH synthesis process. In_2O_3 has recently attracted growing interest as a highly selective and stable catalyst for this reaction, and zirconia has been reported as a potential support to significantly improve In_2O_3 catalytic activity. In this work, the effect of the preparation methods on the material and catalytic properties of both pure In_2O_3 and mixed In_2O_3-ZrO_2 were investigated. Three main methods were employed, namely the solution combustion, urea hydrolysis, and coprecipitation using three different precipitating agents (ammonia solution, sodium carbonate, and sodium oxalate). Additionally, the role of Pd was also studied with a series of In_2O_3-ZrO_2-Pd samples prepared by the urea hydrolysis method. Various characterization techniques were used to characterize the physicochemical properties of the catalysts, including X-Ray diffraction (XRD), Scanning Electron Microscopy (SEM) Energy-Dispersive X-ray (EDX), N_2 physisorption, CO chemisorption, H_2-TPR, O_2-TPD, CO_2-TPD, and X-ray Photoelectron Spectroscopy (XPS). The catalytic tests were performed in a flow-plug reactor at 40 bar.

The preparation method and the composition strongly influenced the physicochemical properties of the materials and their catalytic performances. In general, the ZrO_2 introduction significantly improved the performance of the pure In_2O_3. Pd played a role as a promoter although the effect was not significantly pronounced in the tested samples due to a substantially narrow range of the Pd loadings. Indeed, among the In_2O_3-ZrO_2-Pd samples, the max yield of methanol at 300 °C was obtained with the sample IZP-0.50, having a medium loading among the three tested catalysts. The absolute max yield of methanol production was achieved with the catalyst prepared with the coprecipitation using sodium carbonate at 300 °C which was comparable with those reported in the literature: this catalyst had a STY of 107.54 mmol g_{In}^{-1} h^{-1}.

Keywords

In_2O_3

CO_2 hydrogenation

Methanol synthesis

Preparation method

ZrO_2

Palladium

Contents

1. Introduction

It is now taken for granted that the emission of greenhouse gasses (GHGs), such as CO_2, CH_4, and many other molecules, are driving the average global temperature to unprecedented temperatures that will cause serious harm to nature’s equilibria and therefore humankind. Regrettably, CO_2-emitting technologies have been a true nerve center of the economic and social growth of the human population, and they are now the backbone of the present-day society, together with other resources-depleting activities (e.g., fossil fuel extraction, mining, …). The concern about GHGs emissions has recently increased the public, institutional and scientific consideration on more sustainable technologies, especially in energy production and in renewable energies (REs): the energy collected from renewable resources that are naturally replenished, such as sunlight, wind, rain, tides, waves and geothermal heat.

Figure 1 United Nations Sustainable Development Goals (SDGs).[1]

An important step forward in the institutional role in the climate change topic was made in December 2015, at the Conference of Parties in Paris (COP21), where delegates from 195 countries agreed to ‟pursue efforts to limit the (global average) temperature increase to 1.5 °C above pre-industrial levels, recognizing that this would significantly reduce the risks and impacts of climate change”. This agreement went down in history as the ‟Paris Agreement”, and was signed after the publication, in September 2015, of the United Nations Sustainable Development Goals, known as SDGs (Figure 1), for a social, economic, and climatic sustainable future.[1] In order to reach a carbon zero-emission future, a transition to renewable and non-fossil-based energy sources is essential. During the COP21 a second scenario, called ‟2-degree scenario” (or 2DS), was discussed to be the ‟point of no return”, beyond which climate change will most probably be strongly destabilizing and unreversible. In this perspective, the average world temperature cannot increase to 2 °C above the pre-industrial levels.[2]

Sadly, the complete turn point of this transition now appears to be further than the prefixed by the 2DS and current data is showing us that humankind is on the edge of the cliff for a climate disaster. Anthropogenic emissions need to peak within 5 years from now to maintain realistically the COP21 targets; and primary sources consumption needs to drop to a quarter the current use, before 2100.[3]

1.1 Scenarios

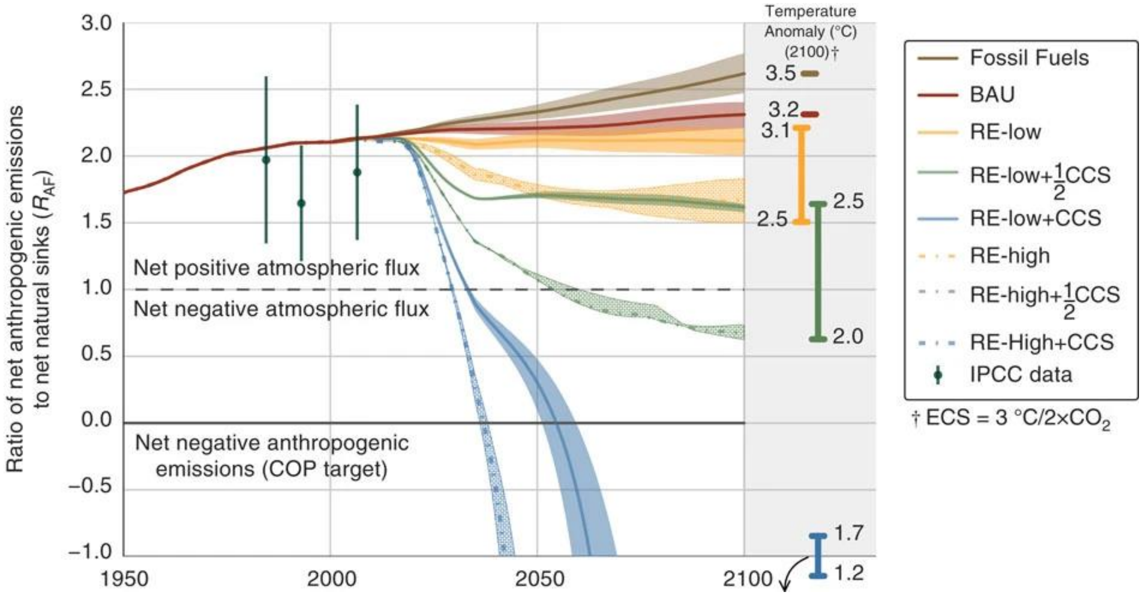

Figure 2 Ratios are calculated annually as the ratio between anthropogenic net C emissions, to net C sequestration by global plant, soil, and ocean systems. The shaded areas represent the scenarios sensitivity. Global surface temperature anomalies projections (DT) in 2,100 are indicated at the right, where each colored bar treats the RE-Low and RE-High scenarios as the endpoints of a continuous range of energy sector decarbonization.[3]

By examining Figure 2, taken by the work of Walsh, *et al.*,[3] with a business-as-usual (BAU) scenario, therefore by keeping the same current growth trends in decarbonization, we would reach a peak after 2050, missing target maximum temperature increase of 1.5 °C. The term “decarbonization” stands for an abatement in the carbon net emission by a multitude of anthropogenic activities. Even the REs scenarios, where REs grow is virtually boosted at 5.0%

annually, in line with aggressive climate action, will not be enough to respect the target. Full decarbonization relies on the coupling of CCS (Carbon Capture and Sequestration, or CCSU that stands for Carbon Capture, Sequestration, and Utilization, or CSS[4] that stands for Carbon Sequestration and Storage) technologies, bioenergy production, and REs implementation. With a full industry transition, humans will need to couple the capture of the anthropogenic CO_2 excess to avoid going beyond the point of no return.

1.2 Carbon Capture, Storage and Utilization (CCSU)

Anthropogenic carbon dioxide capture and storage is much different from the natural processes behind natural carbon sinks: it has been estimated that approximately 50% of anthropogenic CO_2 emissions are reabsorbed by the oceans and terrestrial land sinks, taking, respectively, 25% each.[5] This seems to play a role of assistance, but these natural carbon sinks act like an ecological buffer, via chemical and ecological feedbacks, which is slowly going to deteriorate the more CO_2 we are going to emit. Furthermore, this carbon dioxide adsorbed by ecological sinks remains an extra amount, out of balance, that causes problems, as soil and ocean acidification, and therefore we are going to need to answer for this distress anyway.[6]

1.2.1 Carbon Capture

Two are the methods for carbon capture: Direct Air Capture (DAC), from the atmosphere, and point-source capture, from the flue gasses of one-point sources of emission, such as industrial plants, power generators, and vehicles. On paper, the DAC is the most tempting, since the capture station can be installed anywhere, its dimensions do not need to respect any plant and no existing plant would need the implementation to adapt to the carbon capture; but the low concentration of CO_2 in the atmosphere (slightly above 400 ppm) is a huge thermodynamic obstacle.[7]

On the other hand, the point source capture would be more feasible and efficient, since the CO_2 concentration in the stripped outlet stream of a plant lays between 3 and 35%; the CO_2 capturing process can be performed by post-combustion, pre-combustion, or oxyfuel capture methods.[8] This system, however, is appliable only to large source points, like industrial plants and power generators, and not too small (but numerous) point sources as vehicles; furthermore, transport and storage infrastructures would need to be close to the point source where CO_2 is captured if the utilization plant is not closeby.[7]

The research field of carbon capture has gained attention in the scientific community in recent years, nevertheless, several issues need to be solved, such as low efficiency in CO_2 capturing, lack of legislation, processes costs, and real environmental sustainability of the processes.

1.2.2 Storage versus Utilisation

Two are the possibilities of CO_2 employment of the post-capture application: direct carbon storage (CCS) or carbon utilization (CCU). The CCS option is coarser, but it has a high-volume potential over the overall human emissions, while the CCU is a more elegant solution (from the circular carbon economy point of view: “avoiding” emissions by reusing spent CO_2) but a smaller impact by the percentage on the volumetric emissions.[9] It is most likely that we are going to need a combination of the two techniques in the soon future, the so-called CCSU, to actualize the scenarios, even if chemical production from CO_2 will probably have a relatively minor role to play in terms of volume for CO_2 emission reduction. Having said that, its weight cannot be discounted because of the potential economic benefits and the increasing demand for the several carbon-based chemicals derived from fossil fuel sources (thus termed petrochemicals) that can be produced from CO_2; furthermore, the storage facilities for CO_2 are limited.

1.3 Chemical valorization

The CCU intrinsically includes the concept of chemical valorization: the CO_2 is introduced back in the industry from a worthless and harmful scrap molecule to a more complex form of value-added products, such as biofuels, that have become a huge priority, or base chemicals, like methanol.[8] Carbon dioxide has also long been identified as one potential vector molecule to inject REs and their surplus peaks, into the energy chain, like other possible energy vectors (H_2, ammonia, ...), while contributing to close the carbon cycle connected to CO_2 emissions and produce chemicals that can be easily inserted in the chemical production chain.[4] REs can be used or stocked directly in these processes (as solar thermal energy or geothermal heat), but most commonly it is converted into a secondary energy medium, as electricity, which is widespread and easy to introduce in the electricity grids.

Engaging now the chemical valorization route, a distinction must be drawn between base and fine chemicals: base chemicals are large volume products and thus with a higher effective fossil fuel consumption, that is potentially easier and larger to replace with REs direct inputs; fine chemicals, on the other hand, generally do not incorporate RE, except by an intermediate formation of chemicals, such as methanol, and their production is rather limited in terms of volume of products, and will thus have a minor impact in terms of CO_2 and REs consumption.[10]

Hereafter is shown a schematic overview (Figure 3) of the possible CO_2 conversion products, mostly base chemicals, their routes, and the potential ways to incorporate REs in these processes: methanol is the most interesting product, as a widely used raw material in the chemical industry and a possible intermediate to produce olefins.

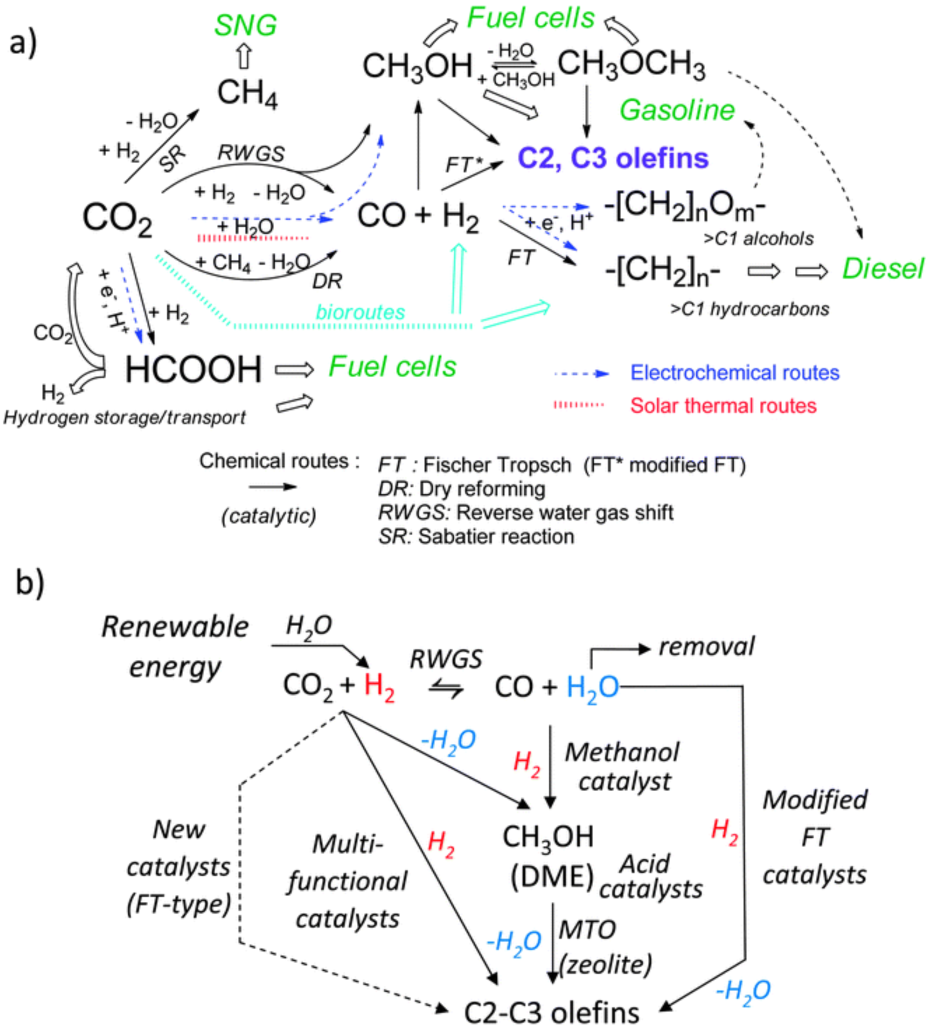

Figure 3 (a) Schematic overview of CO_2 conversion routes and potential REs integration. The RE is either direct (solar thermal) or indirect (renewable H_2 production, electrochemical routes). (b) Different possible routes to synthesize light olefines from CO_2 and H_2.[10]

1.3.1 Hydrogen’s role

It is clear that H_2 is a key molecule for this class of reactions, and we are now widely aware that a carbon-free society will not be possible without a renewable H_2 economy: as it is outlined in Figure 3, H_2 is an energy and electron carrier, a fundamental base chemical and a key connector of REs and the chemical industry, in particular for the CO_2 valorization processes discussed previously; therefore, it is necessary to develop better and more efficient processes to produce H_2 from REs.[11,12] It is indeed true that most of the CO_2 reductions need hydrogenation, and for a sustainable application of CCU, hydrogen needs to be cheap and renewable. Currently, cheap H_2 comes from carbon-intensive fossil fuels-based processes (i.e., steam reforming of methane). A noncarbon-intensive approach for H_2 production is water electrolysis, which, however, is 3−4 times more expensive than H_2 produced from fossil sources,[7] and the sustainability problem is moved down the production chain from the raw materials to the energy used during the electrolysis. H_2 would need to be produced economically via water electrolysis using clean and/or renewable energy (e.g., wind, solar, nuclear, ...) to pursue the entire process sustainability.

1.3.2 Thermodynamics

Sadly, the stark reality of CO_2 needs to be addressed: its inertness and thermodynamic stability; carbon dioxide is the most stable end-product when dealing with carbon oxidation and the bigger is the thermodynamic “hurdle” we need to face, the harder the obstacle will be to cross. C-O bonds are stronger than C-H bonds, consequently, oxygenated products have higher stability compared with their hydrogenated counterparts (Figure 4). Furthermore, most of the products that can be obtained from CO_2 are liquid at atmospheric conditions, therefore the reactions are entropically unfavorable. The chemical transformation of CO_2 is thermodynamically more favorable when it is used as a co-reactant a molecule that has a higher Gibbs free energy such as H_2. Based on these energetic premises, we can deal with two different CO_2 conversion categories: when the more energetic secondary reactant supply enough energy to the reaction to be exothermic and work without a catalyst (carboxylates and lactones, carbamates, urea, isocyanates, and carbonates); and when the reaction is not enough energetically favorable and it needs a considerable source of external energy plus a catalyst to overcome the high activation energy of the C=O breaking.[7]

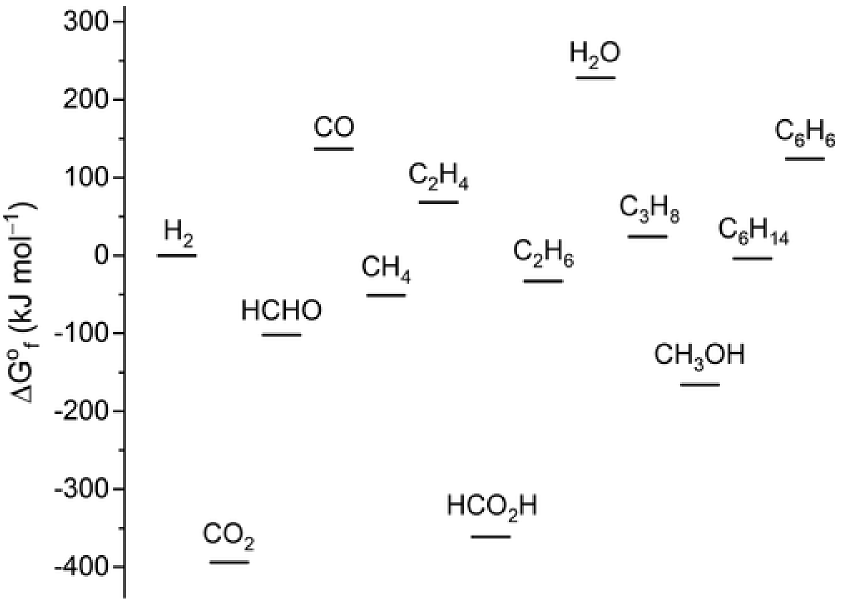

Figure 4 Gibbs free energy of formation ($\Delta G_{0,f}$) for simple carbon compounds at different oxidation states of carbon; H_2 and H_2O are included for their key role. Reprinted with permission from American Chemical Society.[7]

1.3.3 Current status of chemical valorization

The inertness and thermochemical stability of CO_2 lead the research to prioritize the study of new active, selective, and stable catalysts; multiple catalytic pathways are now a matter of investigation by research groups.

A young and alternative strategy for CO_2 transformation is photocatalysis, but the efficiency is substantially lower than the targeted amount for CO_2-involving reactions;[13] the research is mainly focused on thermal or electrochemical catalytic reduction.[14] So far, the electrochemical reduction has the huge advantage to extract the needed H_2 from the water molecule in the medium, allowing the avoidance of the use of gas H_2, but technical problems are still huge, as the small scale required and the difficulties in the scale-up process.[15] The traditional thermochemical processes are right now the most promising, thanks to the abundant pre-existing literature on other akin processes and the presence of industrial plants that can easily be adapted to CO_2 hydrogenation. Homogeneous catalysts are now out of the picture for many reasons (hard separation, poor process economy, and small processable volumes) and this leads to the research on heterogeneous catalysts.[16–18]

1.4 Methanol

Methanol (CH_3OH or MeOH) is the simplest alcohol in its family, liquid at ambient conditions, and a flammable, toxic and harmful chemical. It is one of the main C_1 (molecules containing one C atom) platform chemicals and together with ethylene, propylene, benzene, toluene, and xylenes, it is among the most demanded petrochemicals worldwide.[19] With an annual growth rate of 6 % between 2014 and 2019,[20] methanol had a production capacity of 157.27 million metric tons in 2020 and it is forecasted to double within 2030.[21]

Other than being a chemical commodity for the synthesis industry, it is also a fuel additive and a potential sustainable fuel itself. To tackle the problem of energy storage and, in parallel, the discontinuity and surplus peaks in renewable energies, methanol could be employed as an energy carrier molecule of the Power-to-X (PtX) processes that stock energy, such as the electricity peaks in renewables, in another storable form, as chemical energy; this compound can then be fed to another process (e.g., combustion, fuel cells, …). The PtX process can lead to liquid energy carriers (PtL), as in the case of methanol, or gaseous energy carriers (PtG), as in the case of methane, another potential candidate. Operational costs analysis suggests that methanol synthesis has the highest overall efficiency compared with methane since CH_3OH does not require compression and decompression, has a higher volumetric energy density, and lower transportation costs.[22]

1.4.1 Methanol synthesis history

In 1913 the German company BASF synthetized methanol from syngas (Reaction (1), a mixture of CO and H_2) obtained from coal, by using a zinc/chromium oxide catalyst;[23] 10 years later the same company built the first commercial methanol synthesis plant operating at very high temperature and pressure (300 - 400 °C, 250 - 350 atm).

$$(1)\ CO + 2H_2 \rightleftharpoons CH_3OH,\ \Delta H^\circ = -90.5\ kJ\ mol^{-1}$$

Years after, at the beginning of the 1960s Cu was discovered to be active toward the production of methanol from natural gas and naphtha[24] and the Imperial Chemical Industries achieved a new industrial process operating at milder conditions (200 - 300 °C, 50-100 atm). Since then, Cu-based materials have always been employed in industrial methanol production through syngas.[23]

The commercial heterogeneous catalyst Cu-ZnO-Al_2O_3 usually contains 50 – 70 atomic % CuO, 20 – 50 % ZnO and 5 – 20% of the Al_2O_3 promoter. The industrial catalyst is also able to convert to methanol a small percentage of CO_2 present in the gas inlet feed of the industrial process, bearing the water produced by RWGS reaction without its activity being affected. Considering the activity towards CO_2 and the present literature behind it, Cu-ZnO-Al_2O_3 was the first and most studied catalyst for CO_2 hydrogenation to methanol.[25]

1.4.2 Reaction conditions and thermodynamics

During the process of CO_2 hydrogenation to methanol, two reversible reactions are involved: CH_3OH is produced via CO_2 hydrogenation (Reaction (2)) while CO is generated via reverse water-gas shift reaction (RWGS, Reaction (3)):

(2) $CO_2 + 3H_2 \rightleftharpoons CH_3OH + H_2O$, $\Delta H° = -49.4\ kJ\ mol^{-1}$

(3) $CO_2 + H_2 \rightleftharpoons CO + H_2O$, $\Delta H° = +41.2\ kJ\ mol^{-1}$

The CO formed in the RWGS reaction may also react itself with H_2 to produce more methanol (Reaction (4)):

(4) $CO + 2H_2 \rightleftharpoons CH_3OH$, $\Delta H° = -90.5\ kJ\ mol^{-1}$

During the process we aim at the Reaction (2) and (4), exothermic and with an increase in the moles of the product: according to Le Châtelier’s principle, the favorable conditions are high pressure and low temperature. While the parasitic RWGS is endothermic and occurs without changes in the total number of molecules, therefore it is favored by high temperatures, while pressure has no thermodynamic effect on the reaction equilibrium. The industrial methanol synthesis employs a pressure of 50-100 bar,[26] but, although the thermodynamics lead to low temperatures reaction, the kinetic limits the hydrogenation and therefore force to use high temperatures to increase the methanol formation kinetics. As in every commercial process involving low conversion rates toward the products, the unreacted stream is cycled back into the reactor to increase the overall efficiency. Concerning the feed ratio, the H_2/CO_2 volumetric ratio employed is usually 3/1, but the increase of the ratio leads to a higher conversion of CO_2 to methanol due to the sensitivity of this reaction to hydrogen partial pressure.[27]

1.5 Catalysts for CO_2 hydrogenation to methanol

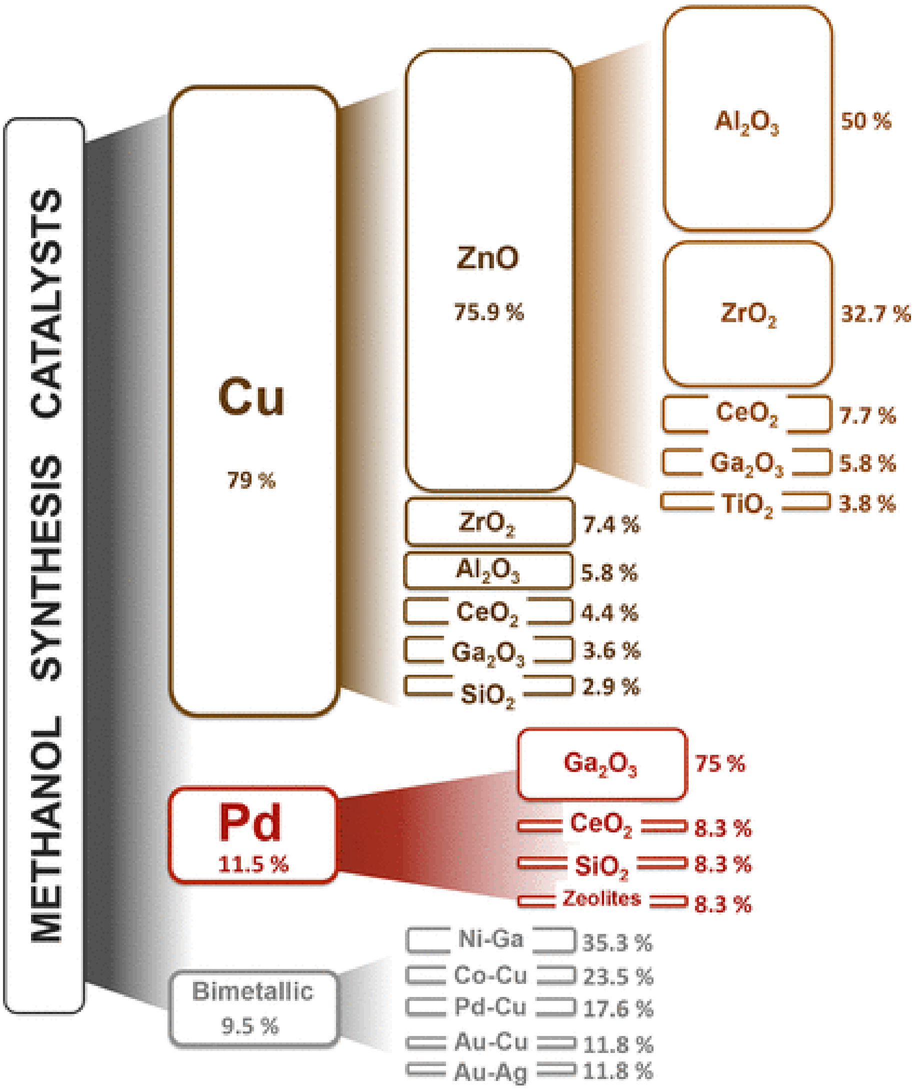

Figure 5 Types of catalyst material reported for CO_2 hydrogenation to methanol in ca. 200 paper published between 2006 and 2016. The marked percentages represent the amount of literature for each material in the whole revised literature. Reprinted with permission from Elsevier.[23]

Figure 5 displays the catalytic materials reported in almost 200 publications over 10 years, from 2006 to 2016 and it is taken from a review of Álvarez A., *et al.*, submitted the 07.12.2016.[23] The relative areas and percentages show how frequently those materials have been reported in the studied collection, and it emerges that the most relevant class of catalysts has been the Cu-based family, in particular the Cu-ZnO-Al_2O_3. This latter material, bearing in mind the activity towards CO_2 and the present literature behind it, was the first and therefore the most studied catalyst for CO_2 hydrogenation to methanol.[25]

1.5.1 Traditional Cu-ZnO-Al_2O_3 catalyst

As for CO hydrogenation to methanol, in the CO_2 counterpart Cu acts as the active species, ZnO is a promoter and a matrix that allows achieving a high dispersion of Cu, whereas the alumina (Al_2O_3) enhances the thermochemical stability of the solid. The ZnO role as a promoter is taken for granted, but its specific mechanism is still under debate: one possibility could be the important role of the Cu-ZnO interface in the CO_2 activation, while the second possibility is the role of a ZnCu bimetallic alloy formed by partial reduction during the reaction. The reaction over Cu is proven to be quite structure-sensitive, therefore the preparation method is a key point. Typically, the preparation is carried out with the simple and effective coprecipitation method (Figure 6), through which it is easy to reach a high dispersion and the high stability of the Cu species.[7]

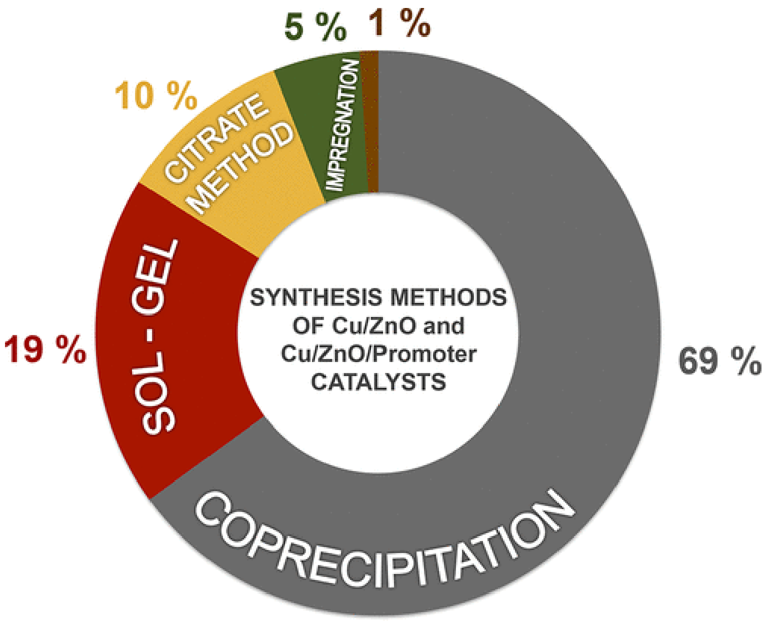

Figure 6 Synthesis methods of Cu−ZnO and Cu−ZnO−promoter catalysts. The marked percentages were calculated based on ca. 200 publications published between 2006 and 2016. Reprinted with permission of Elsevier.[23]

Although the catalyst has a low price and it is remarkably active towards the hydrogenation reaction, it also suffers from a rapid deactivation due to the water formation as one of the main by-products of the parasitic reaction of Reverse Water Gas Shift (RWGS),[28] that also reduces the selectivity of the catalyst towards CH_3OH. This is moreover the limiting factor behind the shallow percentage of CO_2 in the feed stream supported in the syngas-based process. One drawback of this catalyst is that it shows poor activity at low temperature (< 250 °C) and the presence of H_2O induces a strong temperature- and water-induced deactivation of Cu particles by carbon deposition, and Cu oxidation and sintering.[29] These limitations undermined the value of the catalyst for the reaction of hydrogenation, pushing the research to find new catalyst families or to stabilize the Cu-ZnO-Al_2O_3 from deactivation, for instance, the employment of membrane reactors that remove water during the reaction.[16,30]

1.5.2 New non-Cu-based catalysts

In recent years, some different catalytic systems were found to be more active and performant than the Cu-ZnO-Al_2O_3 system. These new catalyst families deal with the activity and stability issues of the traditional catalyst.

1.5.2.1 Intermetallic materials and oxides

Research has revealed that some intermetallic systems are more active than the conventional Cu-ZnO-Al_2O_3 catalyst towards the CO_2 hydrogenation to methanol, thanks to a reduced RWGS activity that hindered the methanol selectivity, different reaction kinetics, and higher stability of the standard catalyst. For instance, Ni-Ga catalysts (particularly Ni_5Ga_3) on silica showed high selectivity and suppression of the RWGS reaction.[31] A bimetallic In@Co system showed a superior performance thanks to an abundance in O-vacancies promoted by the Co support;[32] PdZn supported on CeO_2 had an excellent H_2-dissociation ability of the bimetallic alloy,[33] as well as Pd-Cu bimetallic catalyst, that showed a better mechanism of adsorption and dissociation of both CO_2 and H_2.[34] Intermetallic systems are also a cost-effective alternative unless noble metals are a substantial part of the chemical composition.

Metal oxides such as CeO_2, Ga_2O_3, ZrO_2, and TiO_2 exhibit a fair catalytic activity and methanol selectivity, while the activity of certain oxides, such as ZnO and most importantly In_2O_3, stands out;[35] this is going to be investigated later on in this thesis.

1.5.2.2 Pd-based catalysts

Like in many catalytic reactions, noble metals, such as Pd, are attractive and have already been employed (Figure 5) due to their attractive characteristic: stability, resistance to sintering and poisoning, strong tendency to form allows, and activity towards H_2 adsorption, splitting and spillover.[35–37] Pd has the remarkable capability of easily adsorbing the H_2 in H_2* (* represents a surface-adsorbed species) and split the molecule into two active H* (H_2-splitting); After this dissociative chemisorption happened the adsorbed atomic hydrogen is capable of migrating along the Pd surface and spill over the support material (hydrogen spillover). The support can then be reducible, as TiO_2, ZrO_2, or ZnO, or non-reducible, as SiO_2 or Al_2O_3.[38] These features allow Pd to move atomic hydrogen from sites to the reactive species and complete the catalytic cycle. Having said that, these catalysts suffer, however, from low selectivity, stringent high cost, and weak CO_2 binding.[39]

1.5.3 Role of the support

As well as metal-metal interactions, metal-support interactions can boost the stability and activity of a catalyst. For instance, Yang, *et al.*,[40] observed a stabilizing effect of Ce oxide on a system of Au NPs deposited over a CeO_x/TiO_2 support, thanks to CeO_x's electronic polarizing nature. As is going to be addressed later in this thesis (1.6.1 Active sites), oxygen vacant sites are important active sites in the activity of oxides and other active phases on CO_2 hydrogenation reaction. A support that drives the formation of oxygen vacancies is beneficial for CO_2 adsorption, stabilization of reaction intermediates, and lifespan of the catalyst. For example, a CeO_2 support showed this beneficial promotion of oxygen vacancies on a bimetallic PdZn alloy[33], just as a Co oxide,[32] or a monoclinic ZrO_2,[41] incremented the number of O vacant sites on In_2O_3 active phase supported on these oxides.

1.6 In_2O_3

Before its application in CO_2 hydrogenation, In_2O_3 was studied in the Methanol Steam Reforming (MSR) reaction, until a DFT calculation, published in 2013, suggested the potential of its catalytic application in methanol synthesis from CO_2.[35] The first methodical article that inquired into the likely active bulk In_2O_3 was the work of Martin O., *et al.*,[42] published in 2016, where the research group addressed already the promoting abilities of ZrO_2 support, and the key role of the oxygen vacancies in the catalyst activity and stability.

In_2O_3 exhibits higher methanol selectivity than Cu, Co, and noble metal catalysts and higher catalytic activity than other oxides, such as ZnO. It can also be easily supported and modified, giving accessibility to tailoring for reactants activation sites or stabilization of the intermediates. For instance, the support can influence the presence and abundance of O-vacancies on the surface of In_2O_3, largely accepted as critical role players in the catalyst activity.[43–46]

1.6.1 Active sites

During the hydrogenation reaction, In_2O_3 can be easily reduced to $In_2O_{3-\delta}$ generating a large number of oxygen vacancies (O_v) on its surface. Most of the studies on the catalytic activity of In oxide indicate that the missing O atom creates an ideal active site for the adsorption of one O atom from the CO_2 molecule and its consequent activation.[35] Furthermore O_v can stabilize key reaction intermediates and reduce the over-reduction of In_2O_3 to In metallic and its consequent deactivation.[47] A possible catalytic cycle involving O_v can be visualized in Figure 7: the two oxygen atoms are adsorbed in the O_v in the In_2O_3 surface lattice by the positively charged In atoms allowing a consecutive addition of protons obtained by the heterolytic splitting of H_2. During the reaction, methanol formation replenishes the oxygen vacancy sites, whereas H_2 helps to regenerate the vacancies. But not only O_v are active towards CO_2 hydrogenation: other types of active sites are reported as activation sites for the CO_2 molecule, such as metallic and acid-base sites.[48]

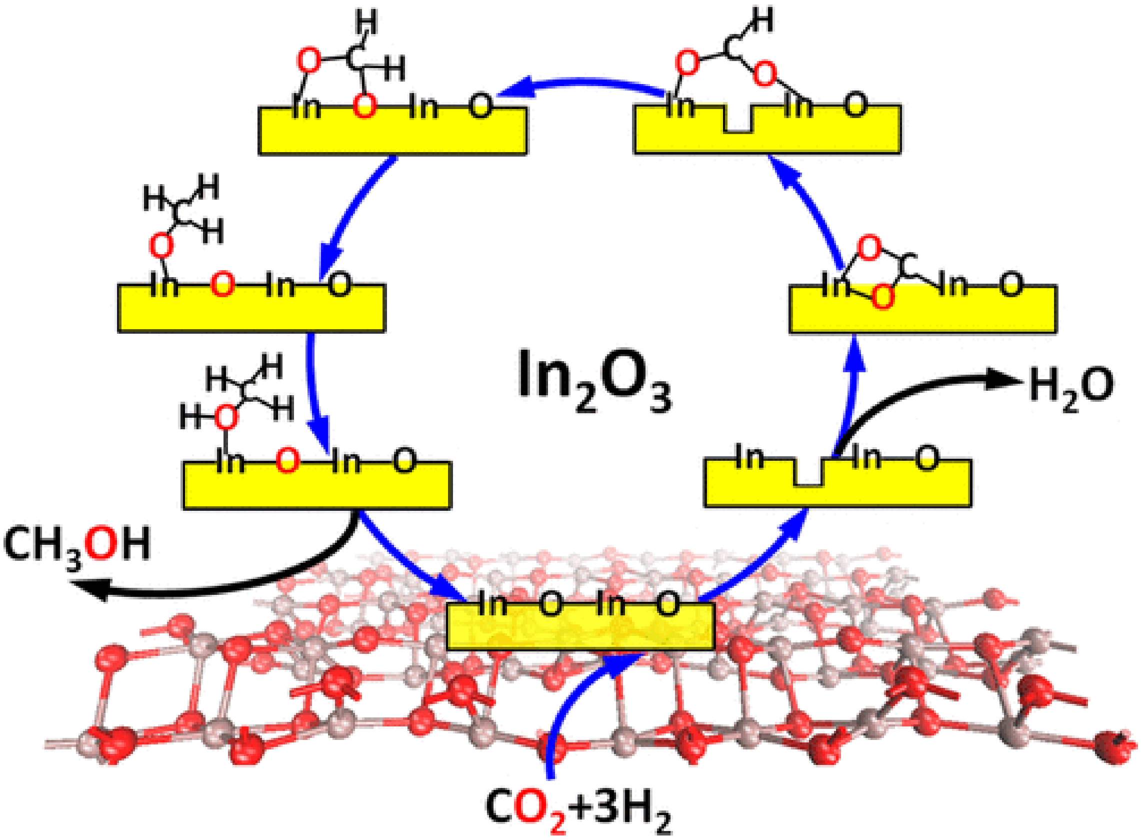

Figure 7 Active oxygen vacancy site for CO_2 hydrogenation to methanol on the defective In_2O_3(110) surface and one of its possible catalytic cycles. Reprinted with permission from Elsevier.[49]

Furthermore, In_2O_3 exhibits higher catalytic activity and methanol selectivity than other metal oxides, such as CeO_2, Ga_2O_3, ZnO, ZrO_2, and TiO_2.[50–52] The correlation of these oxides activity towards the reaction and their CO_2 adsorption energy is clear: the weaker the interaction between the oxides surface and CO_2, the poorer their catalytic activity; but in case this adsorption energy is too strong, like with ZnO,[53] could hinder the correct activation of the CO_2 molecule (Table 1).

Table 1 Calculated CO_2 and CO Adsorption Energies, $E_{ad\text{-}CO2}$ and $E_{ad\text{-}CO}$, on the Metal Oxide Surfaces.[35]

	$E_{ad\text{-}CO2}$ (eV)	$E_{ad\text{-}CO}$ (eV)
In_2O_3	–0.61	–0.89
ZnO	–1.26	–1.40
Ga_2O_3	–0.31	–0.81
CeO_2	–0.19	–0.28
ZrO_2	–0.24	–0.37
TiO_2	–0.17	–0.34

The methanol formation competes with the parasitic RWGS reaction, and the CO adsorption energies (Table 1) are directly related to the product distribution. A lower $E_{ad\text{-}CO}$ indicates that the generated CO can be desorbed more easily, resulting in a high CO selectivity.[35]

1.6.2 Reaction mechanism

Understanding the mechanism of the reaction is fundamental for the reaction optimization: by knowing all the reaction paths, its intermediates, the active sites, and active species, research can tailor the materials to boost the reaction activity through, for instance, stabilization of the key reaction intermediates or enhancement of active sites properties.

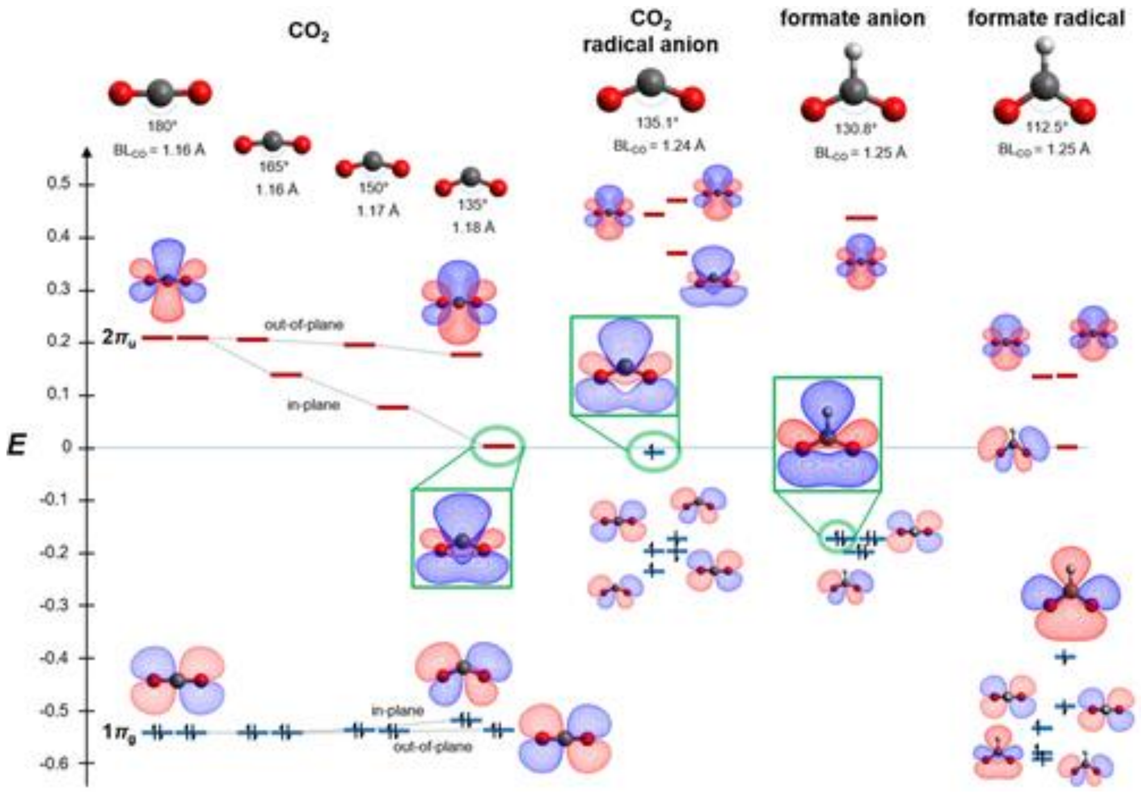

Figure 8 Orbital energy diagrams with characteristic OCO angle and CO bond length, for linear and bent forms of CO_2, radical CO^{2-}, formate ion, and formate radical. The energy scale is in Hartree.[54]

The activation of CO_2 starts from the linear equilibrium geometry of O=C=O: the molecule needs to be bent to break its symmetry and its chemical inertness (Figure 8). By inducing changes in its shape, we can modify the energy level of its molecular orbitals, elongating and weakening the C=O bonds; this makes the C atom more heterophilic and more prone to be attacked to form an active radical anion of CO_2.[54] On the other hand, hydrogen is dissociated on the In_2O_3 surface by heterolytic route, resulting in one negatively charged H (hydride) bound to In and one positively charged H (proton) bound to O.[35]

Experimental and theoretical studies have been carried out to understand the reaction's mechanism.[49,55–57] As shown in Figure 9 two possible reaction pathways are likely to happen, namely, the formate (HCOO*) path and the carboxyl (COOH*) path; in the first, CO_2 is hydrogenated by In−H to form a formate species, while in the second, CO_2 is protonated by O−H to form a bicarbonate species. A third less likely path, responsible for the parasitic RWGS reaction, may be possible, namely RWGS + CO-hydro pathway. Most studies have confirmed that the formate pathway ($CO_2 \rightarrow HCOO^* \rightarrow H_2CO^* \rightarrow H_3CO^* \rightarrow CH_3OH$) on oxygen vacancies of the In_2O_3 surface is the most favorable route, although the COOH* route and

RWGS + CO-hydro route may both be possible. However, the fundamental understanding of the active sites and reaction mechanism is still under investigation and needs to be clarified. Moreover, questions concerning In_2O_3 long-term stability with Time On Stream (TOS), the pathways of catalyst deactivation, and regeneration are still to be addressed.[58]

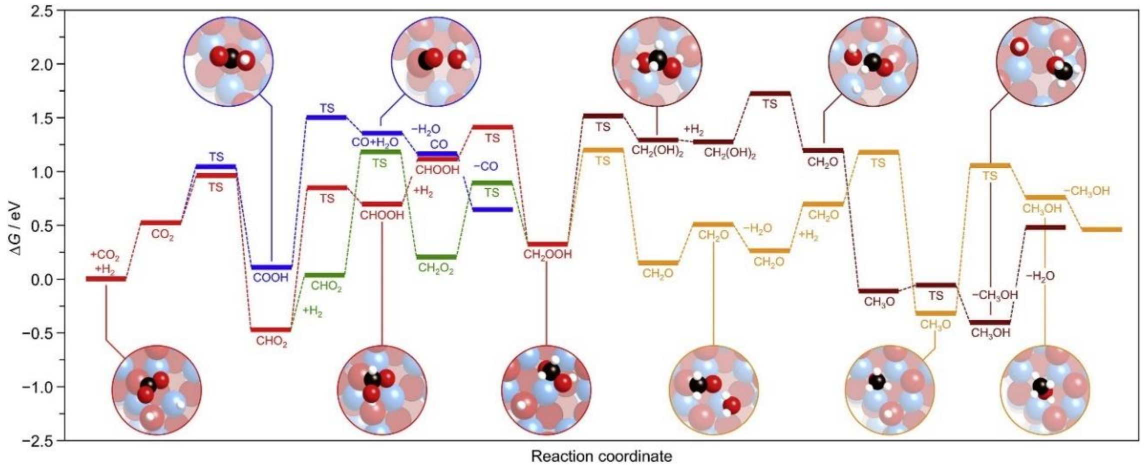

Figure 9 Gibbs energy profile for CO_2 hydrogenation through the most representative paths. C is represented as black, O as red, H as white, In as light blue. The hydrogenation of CO_2 to CH_2OOH is shown in red; from this species, the two possible routes to CH_3OH are depicted in orange and brown. The alternative formation of CH_2OOH from CHO_2 through the co-adsorption of two H_2 molecules is shown in green. RWGS reaction is marked in blue. Conditions: P = 5 MPa and T = 573 K. TS = transition state. Reprinted with permission from Elsevier. [56]

1.6.3 Support

As for the vast majority of heterogeneous catalysts, a support is indicated for various reasons: a general boost in the activity, cost reduction, increment in properties as surface area, porosity, catalyst stability, and therefore, minor deactivation. To boost In_2O_3 features, multiple carriers with distinct nature were explored. The optimal was achieved through the tuning of chemical, physical, and geometric properties of both ZrO_2 and In_2O_3,[41,59] that induced a remarkable improvement of the intrinsic activity of the unsupported oxide, with almost a 10-fold higher STY per gram of indium.[42]

1.6.3.1 ZrO_2

Gao, *et al.*,[52,60] synthesized by coprecipitation an indium−zirconium composite oxide with a higher specific surface area than the sole In_2O_3 and a reaction rate of approximately five times the one of bulk In_2O_3. When In_2O_3 is deposited on a ZrO_2 support, its activity and stability during CO_2 hydrogenation to methanol are increased.[42,55] DFT calculations showed that a ZrO_2

support can inhibit the dissociation of CO_2 into CO on In_2O_3, reducing the relevance of the RWGS kinetic pathway, stabilizing key intermediates of the formate pathway,[44] and enhancing the adsorption of CO_2.[61]

In addition to increasing the dispersion of the active phase, ZrO_2 also facilitates the formation of oxygen vacancies, and these can stabilize the key reaction intermediates and facilitate the adsorption and activation of the reactants on the In oxide surface.[42,44,52,60]

In the case of deposited In_2O_3 on ZrO_2, one possible O_v formation trigger could be the presence of Zr^{3+} species in ZrO_2 before the active phase deposition, which could abstract oxygen atoms from the active phase upon calcination or reaction.[41,42,62] Phase, morphology, and preparation method of the catalyst are key decisions on the catalytic potential of the material. A remarkable case is a study carried out by Frei, *et al.*,[41] where they observed a considerably higher activity for an active phase deposited on a monoclinic-ZrO_2 compared to a more common tetragonal-ZrO_2 support. Phase, morphology, and preparation methods will be displayed in the following chapters.

The india loading on the zirconia support has, obviously, a fundamental impact on the final material performances. In one distinctive article, Yuan C, *et al.*,[55] showed that by varying the indium loading between the narrow 0.1 -5 wt % range, the selectivity to both methanol and CO can reach 80 % in the broad temperature range 250 − 280 °C. It is proposed a synergic effect between highly dispersed india and the ZrO_2 substrate, which allows to highly tune the crystallinity of In_2O_3, the dimensions of the particles, and the reaction pathways that the reactants can take. Crystalline In_2O_3 in intimate contact with ZrO_2, prevails for loadings over 2.5 wt.%, while highly dispersed In_2O_3 dominates for loadings below 0.5 wt.%. At loadings of 2.5 − 5 wt.% the material bonds modestly with the formate pathway intermediates (*HCOO and *H_3CO), resulting in an optimized selectivity toward methanol. However, at lower indium loadings than 2.5 wt.%, strong bonding of *HCOO impedes methanol synthesis.

1.6.4 H_2-splitting promoter

In the hydrogenation of CO_2 to CH_3OH, the H_2dissociation step plays a crucial role in the reaction rate; however, the activity towards H_2 is limited for the sole In_2O_3 phase. Doping In_2O_3 with noble metals is a possible strategy to enhance the dissociation of H_2 and the H-spillover onto the In_2O_3 surface, hence increasing the reaction rate. Moreover, Pd-based catalysts have been already widely studied for the synthesis of CH_3OH from CO at low temperatures[63,64] and CO_2,[45,65–67] as is shown in Figure 5. Pd shows to be among the best choices, but other noble metals alternatives such as Au[68], Ir[69], Pt70, and Rh[71] have been studied.

The activation of hydrogen does not just play a role during the reaction, but it is also conducive to the formation of oxygen vacancies in the catalyst activation. The H-spillover from the noble metal to the In oxide can promote the formation of oxygen vacancies on the In_2O_3 by reduction of In^{3+} and snatching away O atoms by H_2O formation.[45]

The Pd species that is truly active during the hydrogenation of CO_2 to methanol is controversial: there is no evidence that the phase of Pd on the surface of In_2O_3 remains under reaction conditions because most of the characterization techniques are employable before the reaction and after it, *ex-situ*. It is, however, proven as true that InPd intermetallic compounds have a good ability to activate H_2 and they play a role in the hydrogenation reaction, with even 70 % higher rates as compared with the traditional Cu-ZnO-Al_2O_3 catalyst.[72–74] Despite the good activity it is important to notice that the formation of an InPd intermetallic phase means a significant amount of Pd and a major economic burden.

Another drawback of Pd employment is its activity for the parasitic RWGS reaction, in particular in the presence of a SiO_2 support:[74] high-nuclearity Pd clusters thermodynamically advantage the formation of CO over CH_3OH, therefore maintaining small particle sizes is fundamental.[35] Furthermore, bigger Pd particles retain more H_2O, thus facilitating In_2O_3 deactivation by sintering. To overcome this issue, Perez-Ramirez, *et al.*,[66] recently adopted a coprecipitation method to incorporate isolated Pd atoms in the In_2O_3 lattice. By doing so, Pd was embedded into indium oxide pockets, avoiding its clustering during the synthesis. When the solid was then calcined and exploited in the reaction the Pd atoms formed low-nuclearity Pd clusters on the In oxide surface. The apparent activation energy of the RWGS reaction was increased by -7 kJ mol^{-1} compared with a case with a catalyst with the same Pd loading prepared via dry impregnation method.

1.6.5 Phase and morphology

The phase and morphology of all the counterparts that participate during the reaction are central in the catalytic study of a material. With phase and morphology greatly vary properties of the heterogeneous catalyst, both micro-characteristics, such as the crystalline pattern, facets exposed to the reaction and types of O_v, and macro characteristics, like the total exposed surface area of the material and its porosity.

There are three crystal structures reported in the literature for In_2O_3: the cubic bixbyite-type phase (c-In_2O_3), the hexagonal corundum-type phase (h-In_2O_3), and the orthorhombic Rh_2O_3-type phase (o-In_2O_3).[75,76] The O_v on the different crystal phases (c- In_2O_3 and h- In_2O_3) exhibit different catalytic performances for CO_2 hydrogenation. For instance, Wang, *et al.*,[77] found that it is easier to adsorb H_2 and to form oxygen vacancies on the surface of c-In_2O_3, and these oxygen vacancies adsorb CO_2 strongly, compared with h-In_2O_3. Dang, *et al.*,[78] found the oxygen vacancies' properties varies with the crystal type and facet: h-In_2O_3 (104) facet can stabilize greatly key intermediates involved in methanol formation and give higher methanol selectivity c-In_2O_3. Besides, their results show that CO_2 adsorption strength follows the order of h-In_2O_3 (104) > c-In_2O_3 (110) > c-In_2O_3 (111) ≈ h-In_2O_3 (012). Shi *et al.*,[79] synthetized c-In_2O_3, h-In_2O_3, and a mixed cubic/hexagonal- In_2O_3 (c/h-In_2O_3) catalysts with a controllable hydrothermal/solvothermal method. They showed that c/h-In_2O_3 has a significant mixed-crystal effect resulting from the phase mixing, which leads to better textural properties, more O_v, higher CO_2 adsorption strength and capacity, and thus higher conversion of CO_2 and STY of CH_3OH (about 2 times higher), compared to single-phase In_2O_3 catalysts. Furthermore, after use, the mixed-phase oxide has no obvious change, being very stable and too difficult to reduce during the hydrogenation.

The phase of the ZrO_2 support drastically influences the extent of In_2O_3 reduction, its structural evolution during the hydrogenation, and, therefore, its activity. Notably, monoclinic ZrO_2 (m-ZrO_2) showed pronounced effects on deposited In_2O_3 due to the lattice mismatching and consequent tensile stress in the In_2O_3 lattice.[41] The phenomenon was not present on In_2O_3/t-ZrO_2 (tetragonal ZrO_2) which had a 1 order of magnitude lower STY. The tensile forces stabilized In^{2+}/In^{3+} sites in the In_2O_3, which create active In-O_v-In and In- O_v-Zr surface species, a key parameter in the high stability and activity of the In_2O_3/m-ZrO_2 catalyst.[47] Both t-ZrO_2 and m-ZrO_2 have enabled an epitaxial alignment, or epitaxy (a well-define crystalline deposition of a material over another crystalline seed), of the In_2O_3 on their surface, but only m-ZrO_2 has applied this unsettling tensile force.[41] Furthermore, CO_2 is activated to a greater extent on m-ZrO2 than on t-ZrO2, as was already proved for the similar Cu/ZrO_2 catalysts.[80,81]

Tsoukalou, *et al.*,[47] reported that the phase of ZrO_2 significantly affects the local structure, reducibility, and catalytic performance of In_2O_3 NPs deposited on a ZrO_2 support for the hydrogenation of CO_2 to methanol. For example, in contrast to m-ZrO_2, the a-ZrO_2 support promotes the rapid reduction of In_2O_3 to metallic In, leading to an almost inactive catalyst. The t-ZrO_2 support avoids the complete conversion to In^0, but the extent of reduction is substantial, with an average oxidation state of In below +2, associated with poor catalytic activity.

Adopting coprecipitation methods for the material synthesis, even the formation of an india−zirconia solid solution phase may also play a significant role in catalyst activity. Employing this promising preparation method, the maximum interaction between the two metal oxides is reached, yet solid solutions of In_2O_3 with t-ZrO_2 showed an inferior catalytic performance in comparison to supported In_2O_3/m-ZrO_2 and In_2O_3/t-ZrO_2 catalysts.[41,82,83]

As it was examined in the second half of the previous paragraph ”1.6.4 H_2-splitting promoter”, the promoter’s phase and morphology characteristics are crucial: either the presence of Pd^0 or intermetallic PdIn species, or the dimension and distribution of the particles can substantially vary the catalyst performances, such as RWGS pathway selection, or the H_2-splitting and hydrogen spillover final characteristics.

1.6.6 Preparation method

As in all the branches of heterogeneous catalysis, the synthesis method of the material, its post-synthesis, and activation treatment are the groundwork on which the performance of the catalyst stands. The method employed, all its conditions, from the initial to the final, the timings, and the chemicals employed are a few of the countless parameters that can influence the final performance of the material: the active phase mode of introduction on its support varies their same interaction, and phase and morphology of the solid largely depends on the preparation method conditions.

One clear example is given by Frei, *et al.*,[41] that demonstrate that an In_2O_3−ZrO_2 material synthesized via coprecipitation formed a solid solution which resulted in an inferior activity, whereas the deposition synthesis formed sub-nanometric islands of In_2O_3 under tensile stress, which triggered the formation of an excess of O_v and enhanced its activity. Again, Perez-

Ramirez, *et al.*,[66] adopted a coprecipitation method to incorporate Pd atoms in the In_2O_3 lattice and showed that Pd was embedded into indium oxide pockets, avoiding its clustering during the synthesis, and when the solid was then calcined, the Pd atoms formed low-nuclearity Pd clusters on the In oxide surface. These catalysts showed higher activity compared to the dry-impregnation counterpart.

1.7 Aim of the project

The primary objective of this thesis was to obtain a more in-depth understanding of the influence of two core parameters on the In_2O_3 activity for CO_2 hydrogenation to CH_3OH: the catalyst composition and its preparation method. 11 different catalysts were synthetized by 5 different preparation methods and 3 possible compositions, and this thesis work attempted to find a clear trend correlated to these two crucial parameters.

The compositions consisted of the sole In_2O_3, the mixed oxide (molar ratio 1:1), and In_2O_3-ZrO_2-Pd (with 0.25, 0.50, and 1.0 wt.% of Pd loading). We aimed to the comparison of the bulk oxide with its counterpart supported on ZrO_2, to detect any influence of zirconia; and the comparison of the mixed oxide In_2O_3-ZrO_2 with the equivalent In_2O_3-ZrO_2-Pd, to establish the noble metal promoter effect on the activity. All the catalysts were synthetized with a one-pot method between urea combustion, urea hydrolysis, and coprecipitation with three different precipitating agents, i.e.: NH_4OH, Na_2CO_3, and $Na_2C_2O_4$.

The catalyst's physicochemical properties, such as phase, morphology, superficial characteristics, and redox properties, were investigated by the use of multiple characterization techniques. The catalysts were then tested for CO_2 hydrogenation reaction under the same reactor conditions and, ultimately, the spent catalysts were characterized after the catalytic test to identify any detectable change in their nature.

2. Methods

2.1 Chemicals

All chemicals used for catalyst preparation were $In(NO_3)_3{\cdot}xH_2O$ (≥99.99%, Alfa Aesar), $ZrO(NO_3)_2{\cdot}yH_2O$ (≥99%, Sigma-Aldrich), $Pd(NO_3)_2$ solution (10% w/w (Pd content), Alfa Aesar), NH_4OH solution (25%, VWR Chemical), urea (≥99.5%, Sigma-Aldrich), Na_2CO_3 (≥99.5%, Sigma-Aldrich), $Na_2C_2O_4$ (≥99.5%, Sigma-Aldrich), absolute ethanol (VWR Chemical), NaOH (≥99%, VWR Chemical), $Cu(NO_3)_2{\cdot}3H_2O$ (99-104 %, Sigma-Aldrich), $Zn(NO_3)_2{\cdot}6H_2O$ (≥99%, Sigma-Aldrich), $Al(NO_3)_3{\cdot}9H_2O$ (≥98%, Sigma-Aldrich), and MilliQ water (MILLIPORE, Direct-Q 3 UV).

Thermogravimetric analysis (TGA) was used to determine the water content in the $In(NO_3)_3{\cdot}xH_2O$ and $ZrO(NO_3)_2{\cdot}yH_2O$ precursors (Figure 10). The values for x and y were found to be 3.2 and 6.0, respectively.

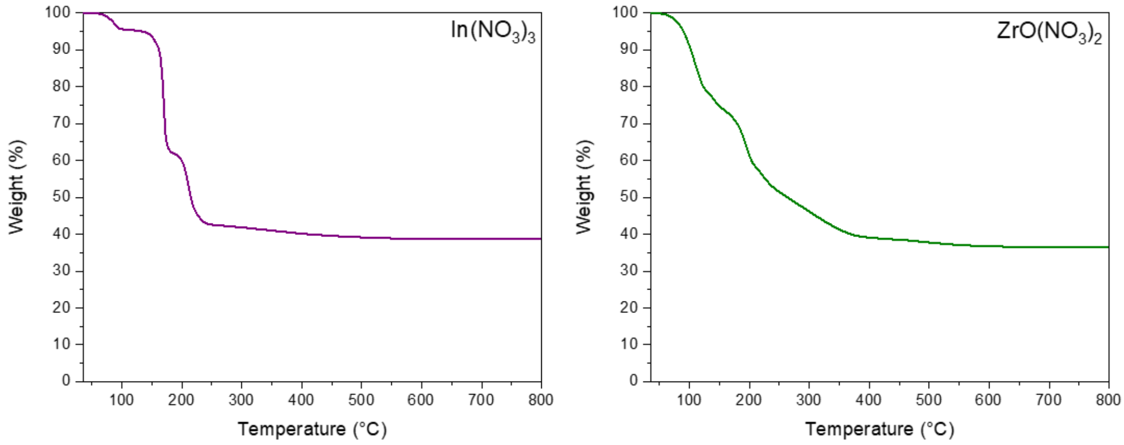

Figure 10 Weight loss profiles of the hydrate nitrate precursors of $In(NO_3)_3{\cdot}xH_2O$ (left) and $ZrO(NO_3)_2{\cdot}yH_2O$ (right) from TGA analysis.

2.2 Catalyst preparation

The synthesis protocol was designed to obtain about 4 g of each catalyst containing sole In_2O_3 and mixed oxides of In_2O_3-ZrO_2 (molar ratio 1:1), or In_2O_3-ZrO_2-Pd (with 0.25, 0.50, and 1.0 wt.% of Pd loading). The following synthesis methods were used: urea combustion, urea hydrolysis, and coprecipitation with three different precipitating agents, i.e.: NH_4OH, Na_2CO_3, and $Na_2C_2O_4$.

All the samples, with the only exception of the benchmark catalyst, were calcined under the same conditions: a temperature ramp from 20 to 500 °C with a heating rate of 5 °C min^{-1} and a calcination plateau at 500 °C for 6 h. The benchmark catalyst was calcined at 400 °C (heating rate 5 °C min^{-1}) for 6 h.

Table 2 displays the label assigned to each catalyst, according to their chemical composition and preparation method.

Table 2 Information on catalyst labels, composition, and the preparation methods

Acronym name	**Composition**	**Preparation method**
I-comb	In_2O_3	Urea combustion
I-ammo	In_2O_3	NH_4/EtOH precipitation
I-hydro	In_2O_3	Urea hydrolysis
IZ-comb	In_2O_3-ZrO_2	Urea combustion
IZ-ammo	In_2O_3-ZrO_2	NH_4/EtOH precipitation
IZ-hydro	In_2O_3-ZrO_2	Urea hydrolysis
IZ-carb	In_2O_3-ZrO_2	Na_2CO_3 precipitation
IZ-oxa	In_2O_3-ZrO_2	$Na_2C_2O_4$ precipitation
IZP-0.25	In_2O_3-ZrO_2-Pd (0.25 wt.%)	Urea hydrolysis
IZP-0.50	In_2O_3-ZrO_2-Pd (0.50 wt.%)	Urea hydrolysis
IZP-1.0	In_2O_3-ZrO_2-Pd (1.0 wt.%)	Urea hydrolysis
CZA-bench	CuO-ZnO-Al_2O_3	Na_2CO_3/NaOH precipitation

2.2.1 Urea combustion (SCS method)

In the pure In_2O_3 catalyst synthesis, 10.23 g $In(NO_3)_3 \cdot xH_2O$ and 8.65 g of urea were mixed with a minimum amount of Milli-Q water in a ceramic crucible and kept under stirring for 1 h. The ratio between urea and indium nitrate precursor corresponded to the fuel to oxidizer ratio (φ) of 2,[84] according to the reactions (5) and (6) stoichiometry:

(5) $2\ In(NO_3)_3 + 5\varphi\ CH_4N_2O + (\varphi - 1)\ O_2 \rightarrow In_2O_3 + (5\varphi + 3)\ N_2 + (3.2 + 10\varphi)\ H_2O + 5\varphi\ CO_2$

(6) $2\ ZrO(NO_3)_2 + 5\varphi/3\ CH_4N_2O + (\varphi - 1)\ O_2 \rightarrow ZrO_2 + (5\varphi/3 + 1)\ N_2 + (6 + 10\varphi/3)\ H_2O + 5\varphi/3\ CO_2$

After that, the crucible was transferred into an oven and the temperature was increased from 20 to 500 °C (heating rate of 5 °C min^{-1}) and held at 500 °C for 6 h. This heating method is commonly known as "volume combustion".

This method yields a yellowish In_2O_3 product in a form of light, fragile and foamy solid (Figure 11). The catalyst was denoted as *I-comb*, where "I" stands for In_2O_3 and "comb" stands for the combustion method.

Figure 11 Image of In_2O_3 material obtained by the combustion method (heating from 20 to 500 °C, followed by a 6 h plateau at 500 °C, a temperature ramp of 5 °C/min).

The mixed oxide In_2O_3-ZrO_2 was synthesized with the same protocol, using 7.08 g of $In(NO_3)_3 \cdot xH_2O$, 3.39 g of $ZrO(NO_3)_2 \cdot yH_2O$, and 7.99 g of urea. The catalyst was denoted as *IZ-comb*, where "IZ" stands for In_2O_3-ZrO_2.

2.2.2 Urea hydrolysis

In a typical synthesis, 10.23 g $In(NO_3)_3 \cdot xH_2O$ and 25.96 g of urea were mixed with 150 mL of Milli-Q water in a round bottom flask and kept under stirring for 30 min. The flask was then placed in a sand bath at 90 °C for 16 h. The top part of the flask was connected with a reflux system using cold water to condense the water vaporized from the solution (Figure 12).

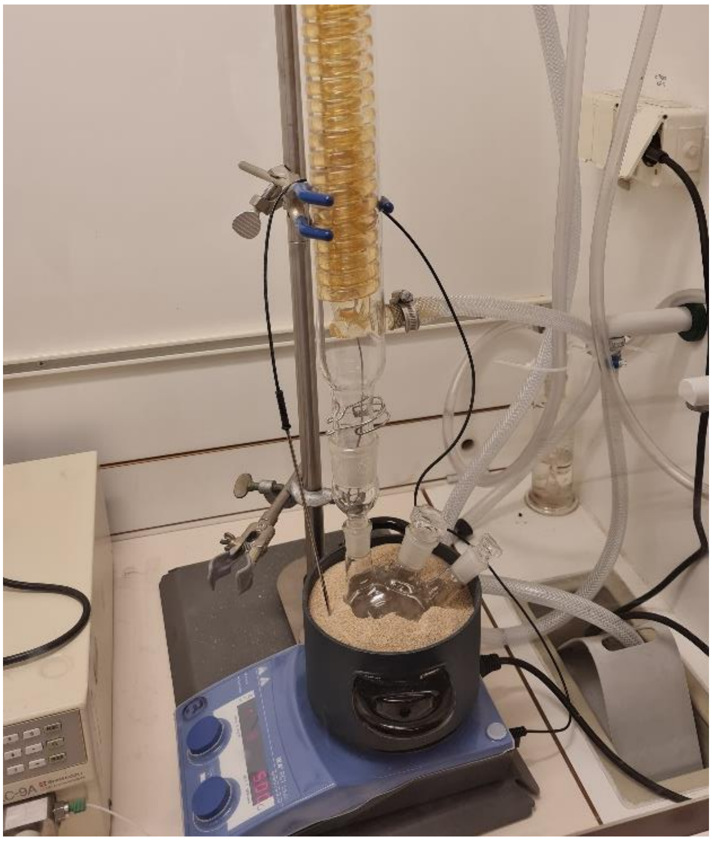

Figure 12 Urea hydrolysis method setup.

The final milky suspension was centrifugated and washed several times with a total of 1 L of distilled water. The solid product was dried at 80 °C for 16 h and subsequently calcined at 500 °C for 6 h (heating rate 5 °C min^{-1}). The catalyst was denoted as *I-hydro*, where "hydro" stands for the urea hydrolysis method.

A mixed oxide of In_2O_3-ZrO_2 catalyst was prepared with a similar protocol using 7.08 g of $In(NO_3)_3 \cdot xH_2O$, 3.39 g of $ZrO(NO_3)_2 \cdot yH_2O$, and 29.97 g of urea. This catalyst was denoted as *IZ-hydro*.

In addition, three samples containing different loadings of Pd (0.25 wt.%, 0.50 wt.%, 1.0 wt.%) were also prepared using the same protocol as *IZ-hydro* but given amounts of the $Pd(NO_3)_2$ precursor was added into the solutions before the heating step. The three catalysts containing Pd were labeled as IZP-0.25 (0.25 wt.%), IZP-0.50 (0.50 wt.%), and IZP-1.0 (1.0 wt.%), where "IZP" stands for In_2O_3-ZrO_2-Pd and the numbers stand for the weight loading of Pd in the catalysts. The preparation method is not stated, because the only Pd-containing catalysts were synthesized with the urea hydrolysis method.

2.2.3 Precipitation using NH_4OH/EtOH solution

In a typical synthesis,[41] 10.23 g $In(NO_3)_3 \cdot xH_2O$ was dissolved in 150 mL of Milli-Q water in a beaker and kept under stirring for 30 min. Then, a mixture of NH_4OH solution (25% in water) and absolute ethanol (volume ratio 1:2) was added dropwise into the $In(NO_3)_3$ solution until the pH reached around 9.2. The milky solution was kept under stirring for 30 min and then it was aged at 80 °C for another 30 min. Finally, the solution was centrifugated and washed with 1 L of water. The solid product was dried at 80 °C for 16 h and subsequently calcined at 500 °C for 6 h (heating rate 5 °C min^{-1}). The catalyst was denoted as *I-ammo*, where "ammo" stands for the employment of an ammonia solution.

A mixed oxide of In_2O_3-ZrO_2 was synthesized in a similar protocol using 7.08 g of $In(NO_3)_3 \cdot xH_2O$ and 3.39 g of $ZrO(NO_3)_2 \cdot yH_2O$. The catalyst was labeled as *IZ-ammo.*

2.2.4 Precipitation using Na_2CO_3

One sample containing mixed oxide of In_2O_3-ZrO_2 was prepared using 7.08 g of $In(NO_3)_3 \cdot xH_2O$ and 3.39 g of $ZrO(NO_3)_2 \cdot yH_2O$. The same procedure of the NH_4OH/EtOH precipitation was followed, however, a solution of Na_2CO_3 1 M was used as a precipitating agent to replace the mixture of NH_4OH/EtOH solution. The resulting mixture was aged at room temperature for 30 min. After that, the suspension was centrifugated and washed with 4 L of hot water (80 °C), until neutral pH, to remove Na as much as possible. The catalyst was labeled *IZ-carb*, where "carb" stands for the use of carbonate as a precipitating agent.

2.2.5 Precipitation using $Na_2C_2O_4$/NaOH

One sample of a mixed oxide of In_2O_3-ZrO_2 was prepared using 7.08 g of $In(NO_3)_3 \cdot xH_2O$ and 3.39 g of $ZrO(NO_3)_2 \cdot yH_2O$, similarly to the case of the precipitation using Na_2CO_3; however, a solution of $Na_2C_2O_4$ 0.3 M was used as a precipitating agent.[85] Note that the pH reached a plateau under the desired amount, with the addition of sodium oxalate. Therefore, it was necessary to add 25 mL of 3 M NaOH solution to reach the 9.2 pH during the precipitation. After a 30 min aging at room temperature, the suspension was filtered and washed with 4 L of hot water (80 °C) to remove Na as much as possible.

2.2.6 Benchmark catalyst CuZnAl

A benchmark catalyst containing mixed oxides of Cu, Zn, Al with a nominal molar ratio of Cu/Zn/Al = 60/30/10 was prepared by the coprecipitation method.[42,86] A nitrate solution (1.0 M, 65 mL) containing Cu/Zn/Al = 60/30/10 (molar ratio) was added dropwise into a beaker containing Na_2CO_3 solution (0.5 M, 26 mL) at 20 °C under stirring with a magnetic stirrer at 500 rpm. The pH was adjusted at 8.0 ± 0.1 by the addition of a solution of NaOH (3.0 M). Note that the amount of Na_2CO_3 was based on the charge balance of the hydrotalcite-like formulation when substituting a divalent cation (Cu^{2+} and Zn^{2+}) in the brucite structure with a trivalent cation (Al^{3+}) with an excess amount of 4-fold. The resulting suspension was aged for 2 h at 20 °C and subsequently filtered and washed with hot water (80 °C, 1.2 L) until neutral pH. The solid was dried at 60 °C for 24 h and it was then ground into a fine powder using a mortar. After that, the material was calcined at 400 °C (heating rate 5 °C min^{-1}) for 6 h. The catalyst was denoted as CZA-*bench*.

2.3 Characterization

2.3.1 Elemental analysis

Elemental compositions of the catalysts were analyzed using Inductively Coupled Plasma Sector Field Mass Spectrometry (ICP-SFMS).

The ICP-MS is a type of mass spectroscopy that uses inductively coupled plasma, electromagnetically produced, to atomize the sample forming atomic and polyatomic ions, which are then detected by the mass spectrometer.[87]

The measurements were performed by ALS Scandinavia (Luleå, Sweden).

2.3.2 X-ray diffraction (XRD)

X-ray diffraction (XRD) is a non-destructive analysis employed to analyze the structure of crystalline solid materials. X-rays are generated from a source, filtered to obtain monochromatic radiation, and radiate it at the sample (Figure 13). The X-rays can interact with the sample in various ways, but this analysis goes in search of constructive interference of the X-rays scattered from the sample, following Bragg’s Law (Equation 1):

Equation 1

$$n\,\lambda = 2d\,sin\theta$$

This law relates the wavelength of the incident electromagnetic radiation (λ) to the diffraction angle (θ) and the lattice spacing in a crystalline sample (d); n is the reflection order, which will always be an integer. The diffracted X-rays are detected by scanning the sample through a range of 2θ angles. Interpreting the diffraction pattern can give useful information, such as the sample's crystalline phases, the amount of amorphous solid, and the crystallites dimension; but the pattern reading can only be achieved by comparison of the above with standard reference patterns (e.g., Powder Diffraction Files, or PDFs).[88]

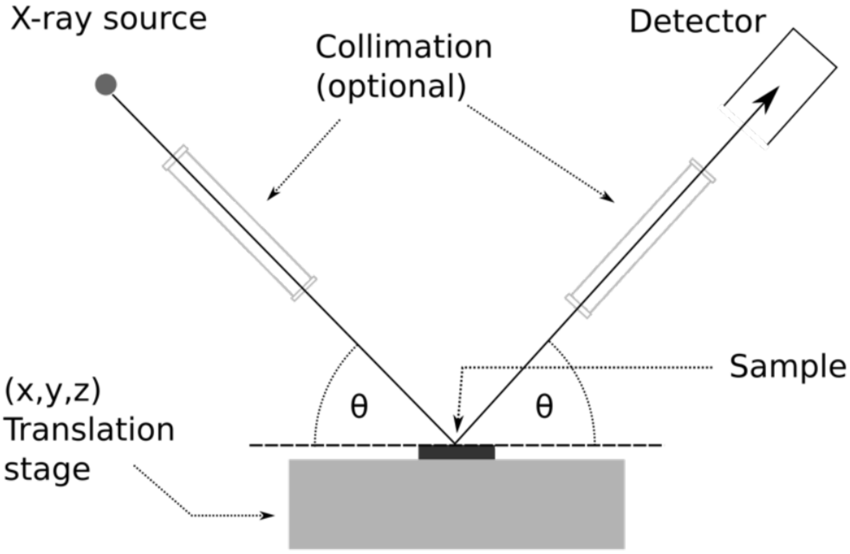

Figure 13 Schematic of an X-ray diffractometer.[89]

XRD measurements were performed for the fine powder of the catalysts using a D8 Advance Diffractometer (Bruker AXS, Germany). The diffractograms were recorded from 10 ° to 70 ° (2θ) with a step size of 0.02 ° (1 s per step). The X-ray source employed was a copper anode.

The average crystallite sizes of In_2O_3 denoted d_c, were determined using the Scherrer equation (Equation 2), where β is the full width at half maximum (FWHM) and the Bragg angles θ at In_2O_3 (431) reflection (2θ around 45.5 °) were determined from the XRD pattern. The wavelength λ of the CuK_α and the shape factor K_F were 0.15406 nm and 0.89, respectively.

Equation 2

$$d_c = \frac{K_F\lambda}{\beta\,cos\theta}.$$

2.3.3 Scanning electronic microscopy (SEM) and Energy-Dispersive X-ray (EDX)

SEM is a type of electron microscopy that produces three-dimensional images from the detection of an electron beam that interacted with the atoms in the sample, permitting a high scanning resolution. From an SEM instrument information on topography and composition can be drawn.

When the intense primary electron beam hits the sample, numerous interactions can happen (Figure 14) between the electrons and the atoms in the sample. Most of the time, the SEM instrument detects Secondary Electrons (SEs), generated as the products of the sample ionization, by the primary electrons. SEs are highly localized and they only escape from the upper surface of the sample, thus allowing to obtain the surface three-dimensional image by combining the position of the secondary beams and their intensity.

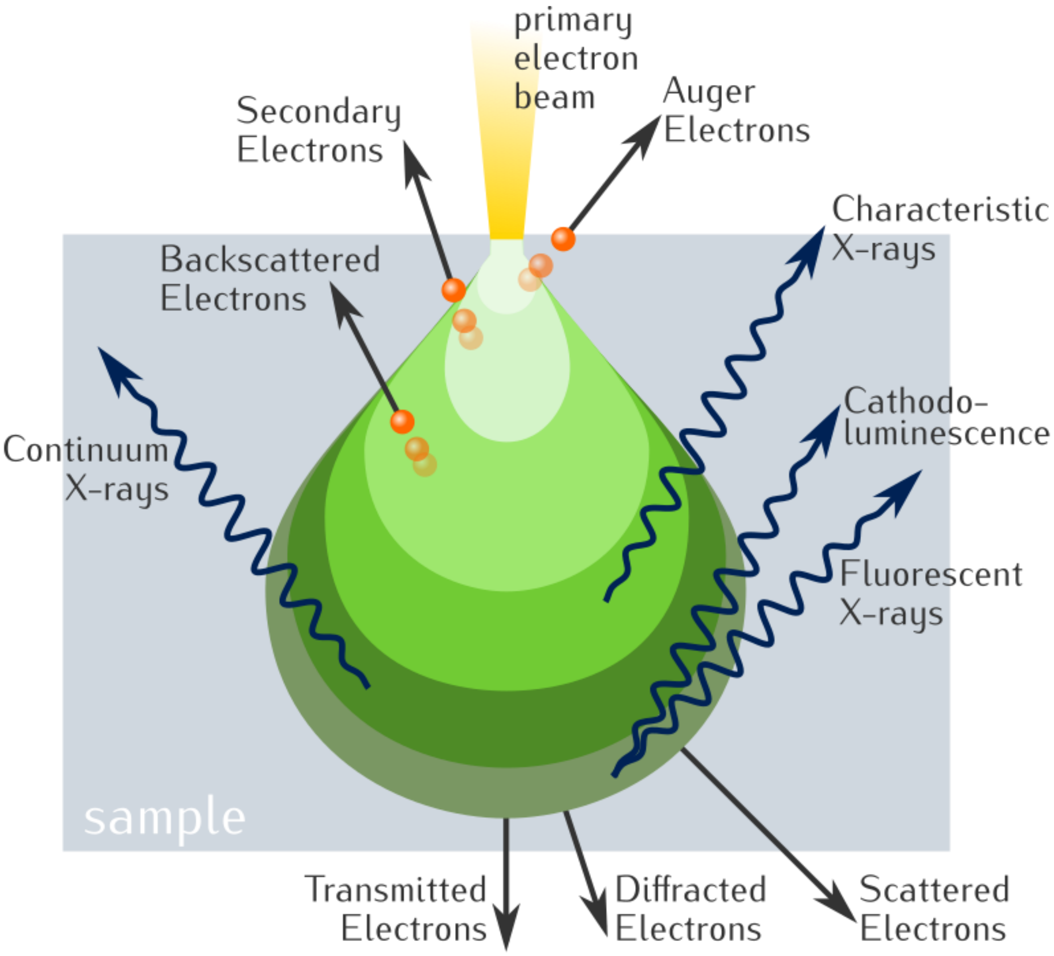

Figure 14 Electron-matter interaction depth and type of signal generated.[90]

The energy released after the ionization of the sample can cause the production of the so-called characteristic X-rays (Figure 14), specific for every element. Through the use of these, we can carry out an overall or a regional EDX scan to detect the morphological composition of the sample.[91]

SEM was used to investigate the morphology of the catalysts. High-resolution images were acquired using JEOL JSM-7800F Prime instrument equipped with an EDX (energy-dispersive X-ray) detector and an SXES (Soft X-ray emission spectrometer).

2.3.4 Nitrogen adsorption/desorption at -196 °C

The N_2 adsorption-desorption analysis is a common and simple method that investigates the surface properties of a solid, such as its Specific Surface Area (SA), Pore Size Distribution, the total volume of the pores, and the type of porosity, by the employment of liquid N_2 at -196 °C (77 K). The solid's surface (adsorbate) adsorbs the N_2 molecules (adsorbate) through Van der Waals forces, and different adsorbate layers are formed (multilayers). The BET (Brunauer-Emmett-Teller) model[92] is applied to obtain the material surface area (Equation 3), and its complementary BJH (Barret-Joyner-Halenda) model is used to obtain the pores size distribution (PSD).

The surface adsorption capacity of molecular nitrogen in a solid surface depends on its relative pressure (P/P_0) where P is the partial pressure of nitrogen and P_0 is the saturated vapor pressure of nitrogen under liquid N_2 temperature.[93]

Equation 3

$$SA_{BET} = n_m^a * L * \sigma_m$$

Where n_m^a is the material's monolayer capacity [mol], L is the Avogadro's number [molecules mol^{-1}] and σ_m is the N_2 cross-sectional area [m^2 $molecule^{-1}$].

The scheme of a typical BET instrument is shown in Figure 15:

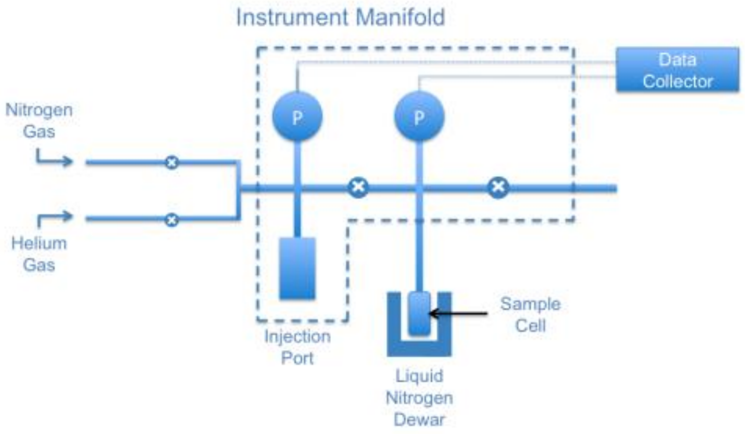

Figure 15 Schematic representation of an N_2 *adsorption-desorption instrument.*

The textural properties of the catalysts were investigated with nitrogen physisorption. The measurements were performed at -196 °C (77 K) using a Micromeritics Tristar instrument. In a typical measurement, approximately 0.2 g of powder catalyst was pre-treated at 250 °C for 8 h. The specific surface area (S_{BET}) was calculated using the Brunauer-Emmett-Teller (BET) multiple-point method in the relative pressure range p/p_0 from 0.05 to 0.3. The total pore volume (V_p) was calculated at $p/p_0 = 0.97$.

2.3.5 X-ray photoelectron spectroscopy (XPS)

XPS is a spectroscopy technique that studies the surface characteristics of a specimen by the employment of the photoelectric effect: the emission of electrons when electromagnetic radiation hits a material; as represented in Figure 16 when the electromagnetic radiation hits a surface, and its photons have higher energy than the material's electrons binding energy, the latter are ejected as characteristic photons. The electromagnetic radiation's wavelength used for this analysis is in the X-ray part of the spectra. This technique can provide qualitative and quantitative information about the surface of a material, such as the elemental composition and the chemical states of elements and chemical surroundings.[94]

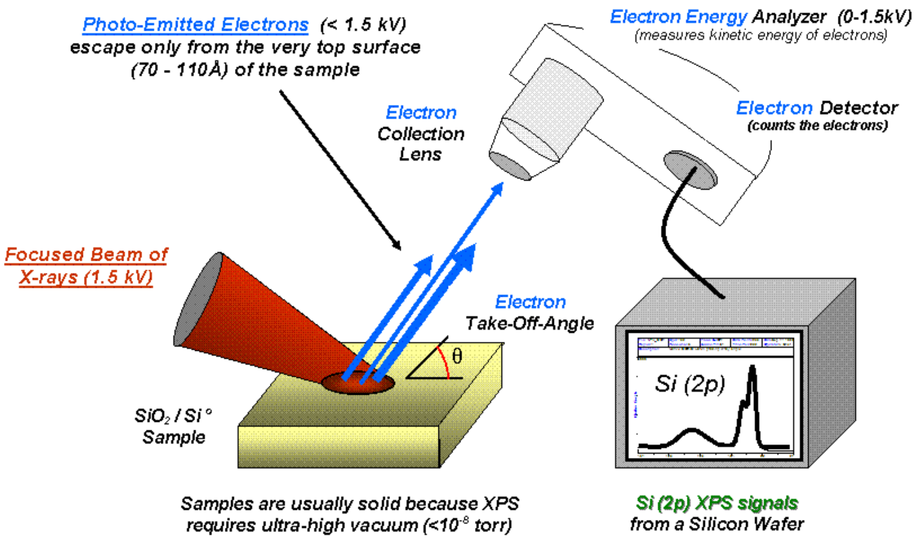

Figure 16 Schematic representations of a monochromatic XPS system.[95]

The oxidation states of each element of the catalyst were determined with XPS. The measurements were performed using a Perkin-Elmer PHI 5000 VersaProbe III – Scanning XPS Mircoprobe^{TM} apparatus (X-ray source AlK$_\alpha$ radiation with energy 1486.6 eV). The binding energy of C*1s* at 284.8 eV was used to calibrate the system before performing narrow scan measurements.

2.3.6 Temperature-programmed desorption with CO_2 (CO_2-TPD) and O_2 (O_2-TPD)

Temperature Programmed Desorption (TPD) is a characterization method used to study the surface adsorption features of a material, by employing specific gaseous carry molecules to investigate characteristic adsorption sites (basic or acid sites, O-vacancies, …). The solid is first scrubbed with an inert gas at high temperatures to remove any previous adsorbate (H_2O, CO_2, …), to then be saturated with the probe molecule of interest; at this point, a constant temperature gradient is applied to desorb at a characteristic temperature according to the adsorption strength, the desorbed probe molecules that are detected through a mass spectrometer (MS). In this thesis, the probe molecules that have been studied were CO_2 and O_2 to study, respectively, CO_2-adsorption sites of various nature and O-vacancies present in the catalyst surface.[96]

CO_2-TPD and O_2-TPD measurements were performed using a calorimeter (Sensys DSC, SETARAM instrumentation) coupled with a mass spectrometer (HPR-20 QIC, Hidden analytical). The sieved catalyst (approximately 50 mg for CO_2-TPD and 30 mg for O_2-TPD, with a particle size of 180-250 µm) was loaded in a quartz fixed-bed reactor (inner diameter 4 mm).

2.3.6.1 CO_2-TPD

The catalyst was pre-treated at 300 °C for 30 min (temperature ramp 5 °C min^{-1}) in Ar (20 mL min^{-1}) and then cooled to 25 °C. A flow of 20 mL min^{-1} of 5000 ppm CO_2/Ar was then introduced to the reactor for 1 h in the adsorption step. After that, the reactor was purged with 20 mL min^{-1} of Ar for 30 min to remove the weak adsorbed CO_2. The temperature was subsequently ramped from 25 to 700 °C (with a rate of 10 °C min^{-1}) and held at 700 °C for 15 min in Ar flow. CO_2 was tracked by a mass number m/z = 44.

2.3.6.2 O_2-TPD

O_2-TPD measurements were performed in a similar procedure as CO_2-TPD, except for the adsorption step a flow of 20 mL min^{-1} of 2500 ppm O_2/Ar was used instead of CO_2. In the desorption step, the temperature was ramped from 25 to 800 °C (with a rate of 10 °C min^{-1}) and held at 800 °C for 15 min in Ar flow. O_2 was tracked by a mass number m/z = 32.

2.3.7 Temperature-programmed reduction with H_2 (H_2-TPR)

The H_2-Temperature Programmed Reduction (H_2-TPR) is employed to investigate the redox properties of a material's surface and its apparatus works similarly to the TPD one: after a preliminary scrub, H_2 is introduced in the line, and the temperature is then ramped with a constant temperature gradient; in this analysis, though, adsorption does not play a role and the signal detected is not the carry molecule desorbed, but the H_2 consumption by the solid, therefore, a negative signal.[97]

H_2-TPR measurements were performed using the same instrument setup as CO_2-TPD and O_2-TPD. Approximately 20 mg of the catalyst was pre-treated at 300 °C for 30 min (temperature ramp 5 °C min^{-1}) in Ar (20 mL min^{-1}) and then cooled to 25 °C. A flow of 20 mL min^{-1} of 1 vol.% H_2/Ar was then introduced to the reactor for 30 min at 25 °C. After that, the temperature was subsequently ramped from 25 to 800 °C (with a rate of 10 °C min^{-1}) and held at 800 °C for 15 min in Ar flow. H_2 was tracked by the mass number m/z = 2.

2.3.8 CO chemisorption

Pd dispersions in the Pd-containing catalysts were determined with CO chemisorption using an ASAP2020 Plus instrument (Micromeritics). Approximately 0.1 g of catalyst (180 – 250 µm particle size) was loaded in a U-shape quartz reactor and then pre-treated in He, evacuated in vacuum at 110 °C, and reduced in H_2 at 400 °C for 1 h. The reactor was subsequently evacuated to 5 µmHg at 400 °C for 30 min and cooled to 35 °C. After that, the reactor was further evacuated to 5 µmHg at 35 °C and a leak test was performed. The sample was again evacuated to 5 µmHg. The first adsorption isotherm (total isotherm) was performed in the pressure range from 100 to 600 mmHg (interval of 25 mmHg). After the first isotherm was completed, the reactor was evacuated to remove physically adsorbed CO before the second adsorption isotherm was repeated. The isotherm of chemisorbed CO was obtained by subtracting the difference between the two isotherms.[98] The intercept of a linear regression curve fit from the isotherm of chemisorbed CO was attributed to the amount of adsorbed CO on a monolayer of the metal surface. The dispersion was calculated with Equation 4:

Equation 4

$$D_M(\%) = \frac{F_S\, N_{CO}}{N_M} . 100$$

where N_M is the total number of atoms of metal, N_{CO} is the number of CO molecules adsorbed on the monolayer, and F_s is a stoichiometric factor considering the form of CO adsorption on the metal. The stoichiometry factor was 2 for Pd.[99] The crystallite size was reported based on the assumption of hemispheric particles.

2.4 Catalytic tests

The CO_2 hydrogenation to methanol was performed in a pressurized, continuous-flow, and fixed-bed tubular stainless-steel reactor (VINCI Technologies, France), with an inner diameter of 1.27 cm and length of 21.5 cm. The reactor total volume was 12.1 cm^3 and it was vertically positioned, with a thermocouple attached to its bottom that ran up to the center (Figure 17).

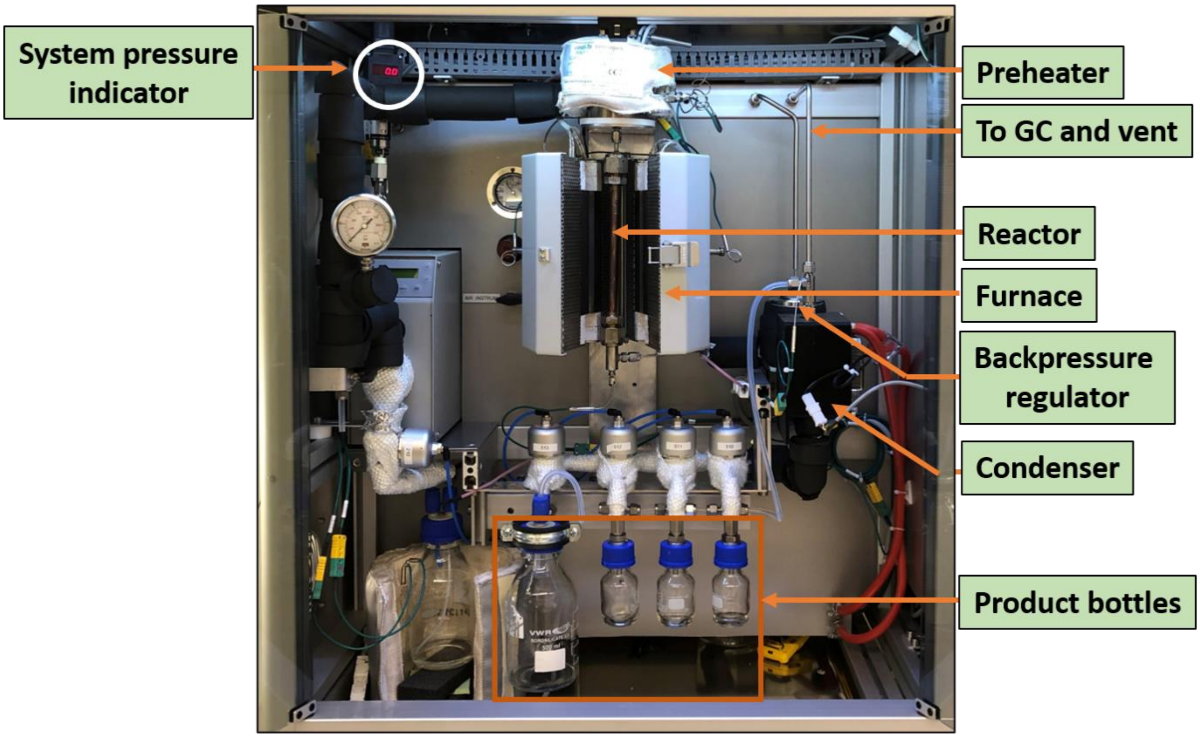

Figure 17 Reactor´s apparatus.

All catalysts were pelletized and a fraction of particle size between 250 and 500 μm was collected and used for the activity tests to avoid the pressure drop issue. For comparison purposes, the activity tests were designed by keeping the same amount of In metal (500 mg) in each sample. This required 605 mg of In_2O_3, 873 mg of In_2O_3-ZrO_2 and in the case of Pd-containing catalysts, it was 875 mg, 877 mg, and 882 mg of In_2O_3-ZrO_2-Pd 0.25 wt.%, 0.50 wt.%, and 1.0 wt.%, respectively. In this way, all tests had the same Weight Hourly Space Velocity (WHSV) of 12000 mL g_{In}^{-1} h^{-1}.

Regarding the reference catalyst CuO-ZnO-Al_2O_3, the total amount of metal (Cu, Zn, and Al) was kept the same as in the In-based catalysts (4.35 mmol g^{-1} which correspond to 336 mg of the reference catalyst).[72]

The catalyst was packed inside the reactor at the vertical center position of the reactor such that the bottom thermocouple tip was in contact with the catalyst bed and the remaining portions of the reactor were filled with SiC (500 μm size particles). For easy separation, the catalytic bed was placed between two thin layers of quartz wool both upstream and downstream so that the catalytic bed was separated from the extra-filling portions of SiC.

2.4.1 Pre-treatment and running conditions

The reactor was placed inside a furnace. H_2 and CO_2 were fed through separate mass flow controllers upstream from the reactor.

After a leak test at 40 bars, the catalyst was pre-treated by heating from room temperature to 350 °C (with a ramp of 5 °C min^{-1}) and maintained at 350 °C for 1 h in Ar flow of 150 NmL min^{-1}. The feed gas was then switched to a mixture of 25 NmL min^{-1} of CO_2 and 75 NmL min^{-1} of H_2 (molar ratio of CO_2:H_2 = 1:3) and the reactor was pressurized to 40 bars. The catalytic tests were conducted at five temperatures from 250 to 350 °C (interval step of 25 °C) at Weight Hourly Space Velocity (WHSV) of 12000 mL g_{In}^{-1} h^{-1}.

The reference catalyst CuO-ZnO-Al_2O_3 was tested under the same condition, except it was reduced with a flow of 5% H_2/Ar before doing the catalytic test.[42]

Immediately downstream from the reactor, a back pressure regulating valve was installed near the exit of the reactor to reduce the pressure of the effluent gas to near atmospheric pressure before it flowed into a condenser at room temperature.

The effluent gas from the reactor was quantitatively analyzed online using a gas chromatograph (GC, SCION 456) equipped with both thermal conductivity (TCD) and flame ionization detectors (FID). The FID data was not taken into consideration in this thesis work. The GC was calibrated with varying concentrations of absolute methanol, CO_2, CO, and CH_4. All calculations were performed with the data collected after the steady-state conditions were reached, obtained in approximately 50 minutes.

2.4.2 Parameters

Carbon balances were all greater than 95 % for all experiments. CO_2 conversion (X_{CO2}) was calculated based on the molar flow rates as:

Equation 5

$$X_{CO_2} = \frac{F_{CO_2,in} - F_{CO_2,out}}{F_{CO_2,in}} \times 100\ \%$$

where $F_{CO2,\ in}$ and $F_{CO2,\ out}$ are the molar CO_2 flow rates at the inlet and outlet respectively.

The selectivities to methanol (S_{CH3OH}) and its side products CO (S_{CO}) and CH_4 (S_{CH4}) are calculated as follows:

Equation 6

$$S_{CH_3OH} = \frac{F_{CH_3OH,out}}{F_{CO_2,in} - F_{CO_2,out}} \times 100\ \%$$

Equation 7

$$S_{CO} = \frac{F_{CO,out}}{F_{CO_2,in} - F_{CO_2,out}} \times 100\ \%$$

Equation 8

$$S_{CH_4} = \frac{F_{CH_4\ out}}{F_{CO_2,in} - F_{CO_2,out}} \times 100\ \%$$

where $F_{CH3OH,out}$, $F_{CO,out}$, and $F_{CH4,out}$ are the corresponding outlet molar flow rates of methanol, CO, and CH_4 respectively.

3. Result and discussions

3.1 Compositional study

3.1.1 Elemental analysis through Inductively Coupled Plasma (ICP)

For each catalyst, the theoretical amount of calcined material was aimed to be 4 g. All synthesis methods provided approximately 3.7 – 3.9 g of the products (92.5-97.5% yields) except for the two samples synthesized by the urea combustion method (ca. 2.2 g and 55% yield). A significant loss in yield of the products prepared by the combustion method did not allow interpreting the elemental composition of these products. Therefore, elemental analysis was conducted by using Inductively Coupled Plasma (ICP) Spectroscopy to verify the compositions of the samples prepared by the combustion method as well as the Pd contents of the IZP series and the possible presence of trace Na in the IZ-carb and IZ-oxa which used Na-containing precipitating agents.

Table 3 Inductively Coupled Plasma (ICP) analysis results for the In_2O_3-ZrO_2 and In_2O_3-ZrO_2-Pd catalysts series.

	In molar %	Zr molar %	Pd wt.%	ppm Na
IZ-comb	48.23	51.77		
IZ-hydro	66.11	33.89		
IZ-ammo	64.91	35.09		
IZ-carb	66.98	33.02		<50
IZ-oxa	65.21	34.79		<50
IZP-0.25	64.78	35.22	0.07	
IZP-0.50	65.82	34.18	0.14	
IZP-1.0	66.6	33.4	0.23	
Theoretical values	66.67	33.33		

As shown in Table 3, all the catalysts showed a molar ratio of In:Zr of approximately 2:1 which is close to the expected value (In_2O_3:ZrO_2 of 1:1 or In:Zr of 2:1), except for the IZ-comb which had a molar ratio of In:Zr = 1:1. A significantly lower ratio of In:Zr indicates that Indium was clearly lost during the combustion process during the synthesis of IZ-comb and most probably I-comb, which showed the same weight loss after the synthesis. This is perhaps due to the loss of Indium precursor, e.g., in the vent line after the ignition during the combustion process.

The Pd contents were 0.07, 0.14 and 0.23 wt.% for IZP-0.25, IZP-0.5, and IZP-1.0 (Table 3), respectively. These values were significantly lower than the expected values, of around four times. The urea hydrolysis synthesis method involves the slow urea hydrolysis that carries the pH solution to higher values thanks to the NH_4OH production, together with CO_2. The reason for this unexpected Pd content is most probably the formation of a stable and water-soluble complex of Pd and ammonia ($[Pd(NH_3)_4]^{2+}$) that has a high stability constant ($\beta \approx 10^{33}$) in the alkaline environment containing ammonia,[100] and that suppressed partially the complete precipitation of $Pd(OH)_2$ in the mixed hydroxides. However, the correlation of the nominal and actual values for the Pd content is linear, suggesting that the Pd content could be controlled with this synthesis method, but not without a partial loss of Pd.

The Na contents of the two samples IZ-carb and IZ-oxa, synthesized using Na-containing precipitating agents, were below the Limit Of Detection (LOD) of the instrument employed (50 ppm) (Table 3). This indicates that post-synthesis washing is effective for Na removal, thus allowing us to compare the activity directly without the interference of Na, which is a potentially active species in the CO_2 hydrogenation reaction.[101]

3.1.2 CO chemisorption

CO chemisorption analysis was conducted for the three samples of the IZP series to determine the Pd dispersions. The results are shown in Table 4. The three catalysts had a Pd dispersion from 23 to 25%, corresponding to the particle sizes of approximately 5 nm. A very narrow range of Pd loadings (0.07 – 0.23 wt.%) resulted in a similar dispersion of Pd among three catalysts, therefore no substantial difference was detected.

Table 4 CO chemisorption analysis results for the In_2O_3-ZrO_2-Pd catalysts series.

	Dispersion (%)	**Particle size (nm)**
IZP-0.25	22.90	4.9
IZP-0.50	25.00	4.5
IZP-1.0	24.40	4.6

3.2 Phase study

3.2.1 X-Ray Diffraction (XRD)

XRD measurements were performed to investigate the crystalline phases of the catalysts. The data were organized into three sets to have a better comparison of the impact of the preparation methods on the structure of the catalysts:

1. Three main preparation methods (comb, hydro, and ammo) for ZrO_2 (Z), In_2O_3 (I), and In_2O_3-ZrO_2 (IZ).
2. Five methods (comb, hydro, ammo, carb, and oxa) for the In_2O_3-ZrO_2 (IZ) series.
3. The urea hydrolysis for the In_2O_3-ZrO_2-Pd (IZP) series with different Pd loadings.

This 3-set grouping will be repurposed in the following paragraphs, for a good comparison for the 3 different series.

The crystallites sizes reported hereafter, were calculated with the Scherrer equation (Equation 2) using the input information of the plane (431) of In_2O_3 at a 2θ of 45.5°.

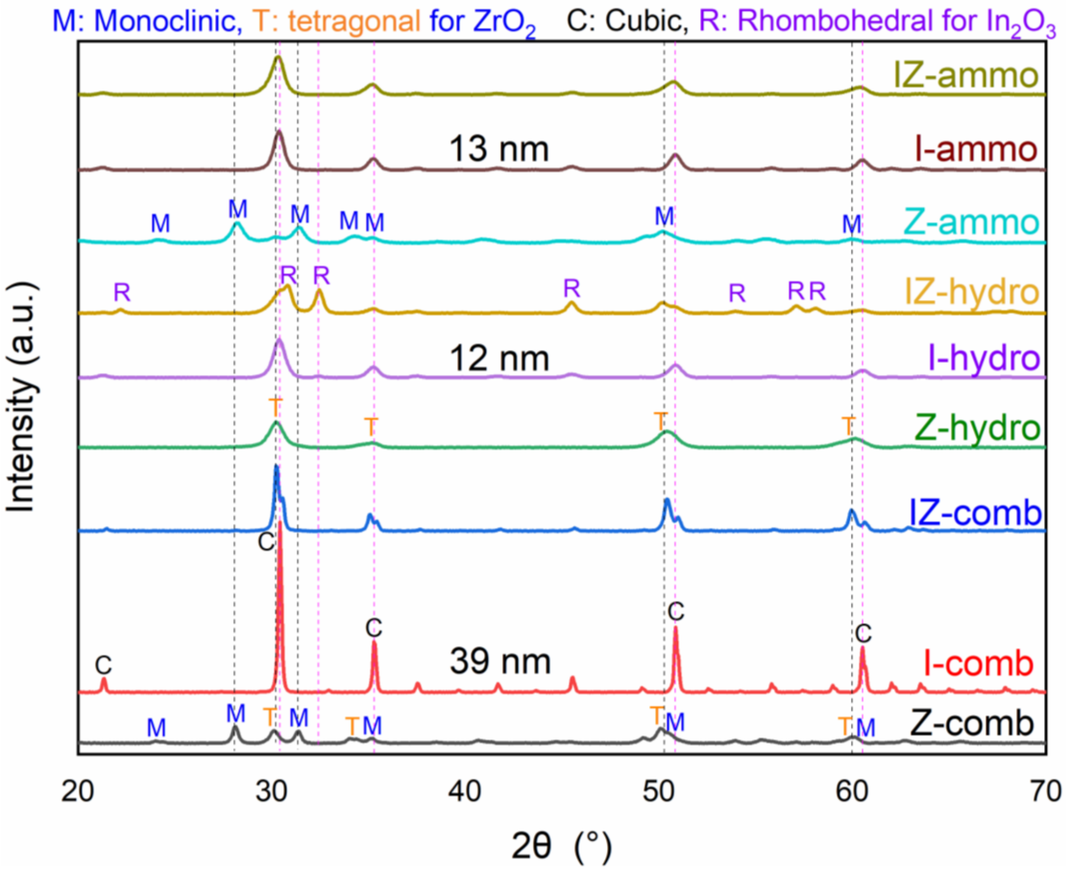

Figure 18 X-Ray Diffraction (XRD) patterns of ZrO_2, In_2O_3, and In_2O_3-ZrO_2 prepared by the urea combustion (comb), urea hydrolysis (hydro), and precipitation using ammonia solution (ammo).

Figure 18 presents the XRD patterns of ZrO_2, In_2O_3, and In_2O_3-ZrO_2 prepared by the urea combustion (comb), urea hydrolysis (hydro), and precipitation using ammonia solution (ammo). The reflections of a cubic structure (space group Ia-3 (206), PDF 00-006-0146) were found for three samples of In_2O_3 regardless of the synthesis method. This structure has also been reported in the literature.[41,42,72] However, the preparation method significantly influenced the crystalline sizes: the combustion method generated the In_2O_3 with a crystallite size of 39 nm (I-comb), which was almost three-fold larger than those prepared by the urea hydrolysis (I-hydro, 12 nm) and precipitation with ammonia (I-ammo, 13 nm). In contrast with In_2O_3, the synthesis methods had a substantial impact on the structure of ZrO_2. Z-hydro showed a tetragonal (T) phase (space group P42/nmc (137), PDF-00-065-0729);[41] while Z-ammo shows a monoclinic (M) phase (P21/a (14), PDF 00-065-0728);[42,47] Z-comb had a mixed phase of both T and M.

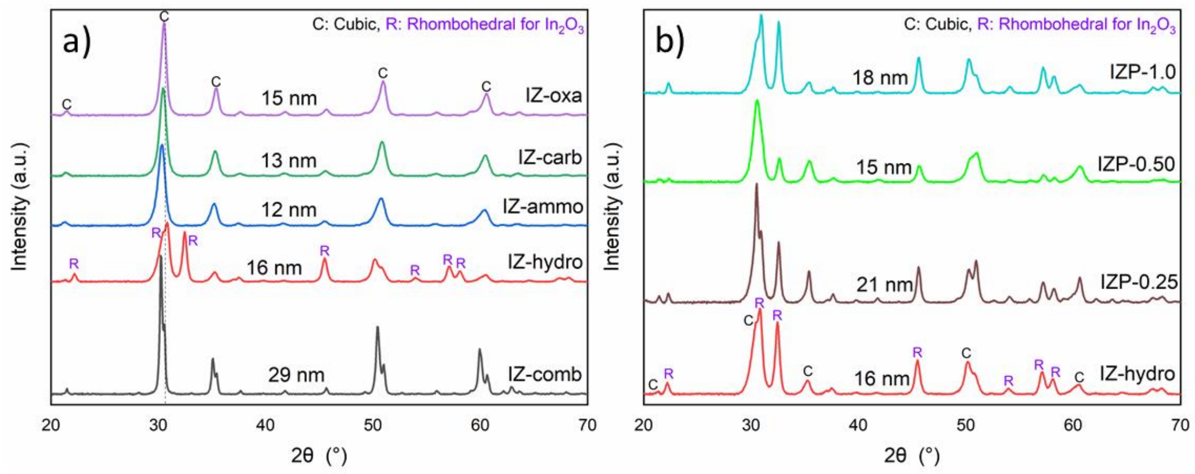

Figure 19 X-Ray Diffraction (XRD) patterns of (a) In_2O_3-ZrO_2 series prepared by the urea combustion (comb), urea hydrolysis (hydro) and precipitation using ammonia solution (ammo), carbonate solution (carb), and oxalate solution (oxa); (b) XRD patterns of In_2O_3-ZrO_2-Pd series prepared by urea hydrolysis (hydro) with different Pd loading (0.25, 0.50 and 1.0 wt.%).

For In_2O_3- ZrO_2 catalysts (Figure 19a), IZ-ammo shows a solid solution of In_2O_3 and ZrO_2 with a cubic structure (like $Zr_{0.18}In_{1.75}O_3$, PDF 04-006-0768), or it could be that the reflections of ZrO_2 masked the reflection of In_2O_3.[47,102] This structure was also found in the IZ-hydro sample and IZ-carb, as well as IZ-oxa. However, the IZ-hydro catalyst also had a rhombohedral phase (also known as “hexagonal” phase in literature) of In_2O_3 (PDF 04-001-8476).[79,103] By contrast, the patterns of IZ-comb showed a mixture of both cubic phase of In_2O_3 and tetragonal of ZrO_2 without a solid solution. The effect of the synthesis methods on the crystallite sizes of In_2O_3-ZrO_2 catalysts was similar to In_2O_3. The IZ-comb showed the size of 29 nm whereas other samples had the particle size in a range of 12 – 16 nm.

Figure 19b presents the XRD patterns of the IZP catalysts. Three Pd-containing samples had both cubic phase of In_2O_3-ZrO_2 and rhombohedral phase of In_2O_3 which was similar to the structure of the IZ-hydro catalyst. This implied that the Pd presence did not modify the phase of the samples. However, the crystallite sizes of the Pd-containing samples were increased slightly to some extent with the IZ-hydro catalyst.

3.3 Morphology study

3.3.1 SEM (Scanning Electron Microscopy) and EDS (Energy-Dispersive X-ray Spectroscopy)

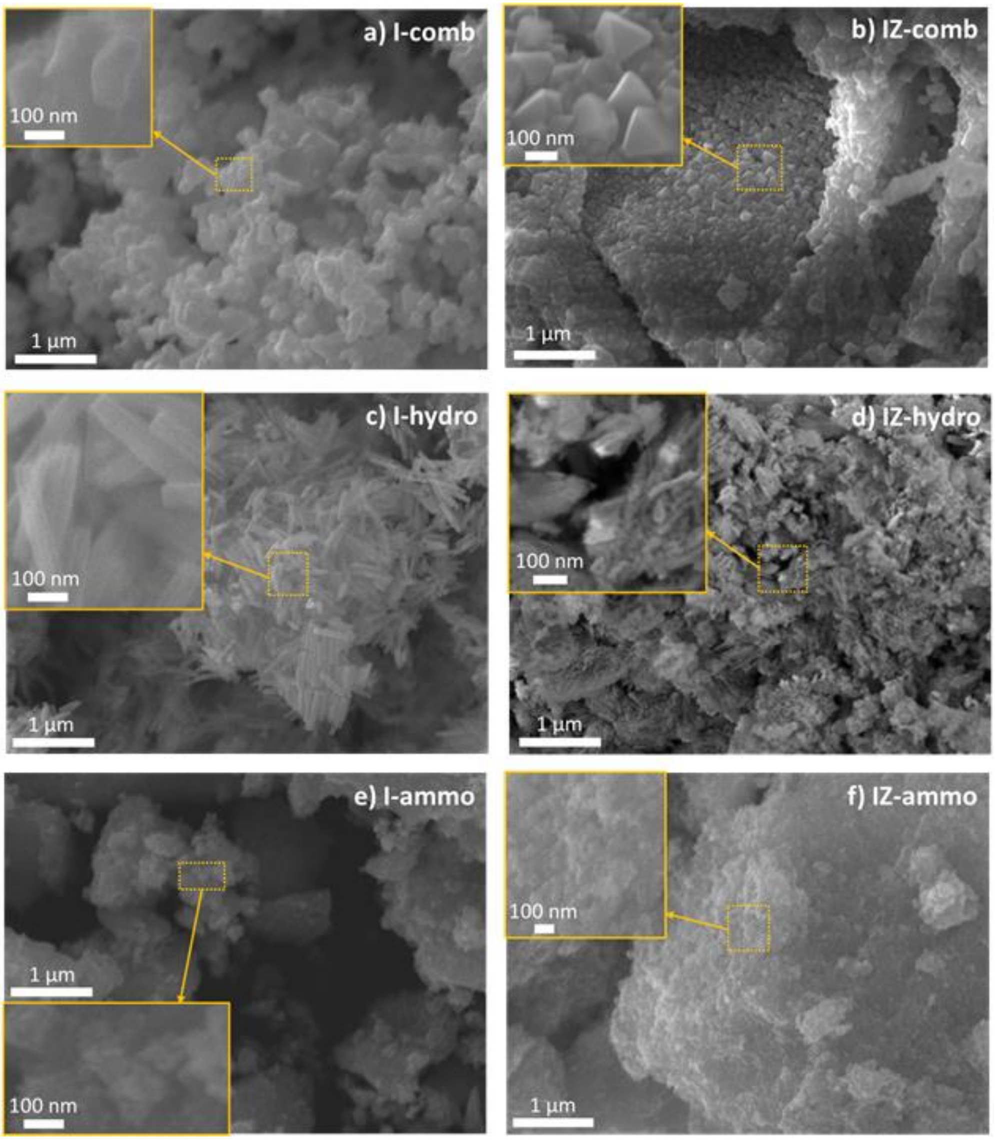

Figure 20 Scanning Electron Microscopy (SEM) images of In_2O_3 and In_2O_3-ZrO_2: (a) I-comb; (b) IZ-comb;(c) I-hydro; (d) IZ-hydro; (e) I-ammo; (f) IZ-ammo.

SEM measurements were performed to investigate the morphology of the catalysts. Figure 20 displays the SEM images of In_2O_3 and In_2O_3-ZrO_2 catalysts prepared by the combustion, urea hydrolysis, and precipitation using ammonia solution. The I-comb showed an agglomeration of small bended-grains, around 200 nm long (Figure 20a). This morphology was also found in the IZ-comb sample, together with well-defined tetragonal crystals (Figure 20b); these tetragonal crystals perhaps belonged to the tetragonal phase of ZrO_2, which would be consistent with the XRD data as both cubic phase of In_2O_3 and tetragonal ZrO_2 were identified in the XRD pattern of the IZ-comb. I-hydro showed rod particles with a length of roughly half of a micron (Figure 20c). The rod morphology was also partially observed in the IZ-hydro, together with a cluster non-well-defined structure (Figure 20d). Compared with the phase identified from XRD, it is hypothesized that the rod particles could be, perhaps, associated with the cubic structure of the solid solution of In_2O_3 and ZrO_2 whereas the cluster morphology belonged to the hexagonal phase (rhombohedral). The I-ammo has a non-well-defined morphology, with big and compact clusters agglomeration (Figure 20e) whereas the IZ-ammo also showed a similar morphology but with smaller clusters (Figure 20f).

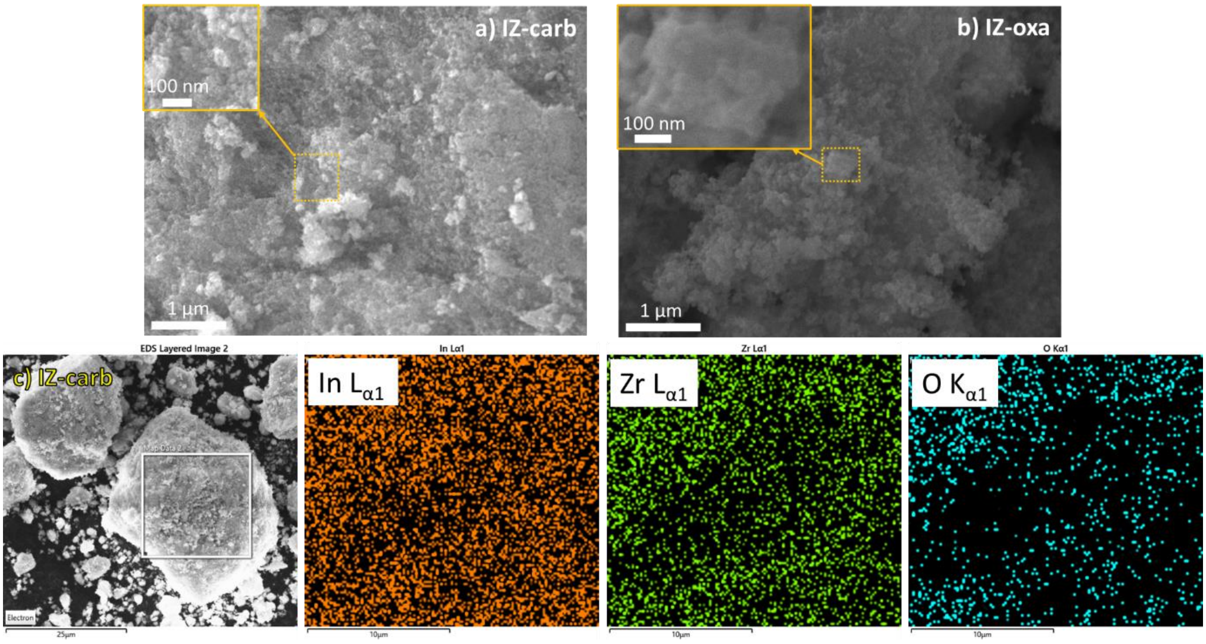

Figure 21 Scanning Electron Microscopy (SEM) images of In_2O_3-ZrO_2 prepared by precipitation using (a) carbonate solution (carb) and (b) precipitation using oxalate solution (oxa). (c) Energy-Dispersive X-ray Spectroscopy (EDS) analysis of IZ-carb.

Both IZ-carb and IZ-oxa showed a similar morphology to the IZ-ammo (Figure 21a and Figure 21b).

Additionally, to analyze the element distribution and homogeneity in the IZ-carb sample, Energy-Dispersive X-ray Spectroscopy (EDS) analysis was performed and the elemental maps are displayed in Figure 21c: overlapped signals of In and Zr were observed, suggesting a homogeneous distribution in the area selected; this result coherently agrees with the XRD data in which a solid solution between Zr and In oxides was identified.

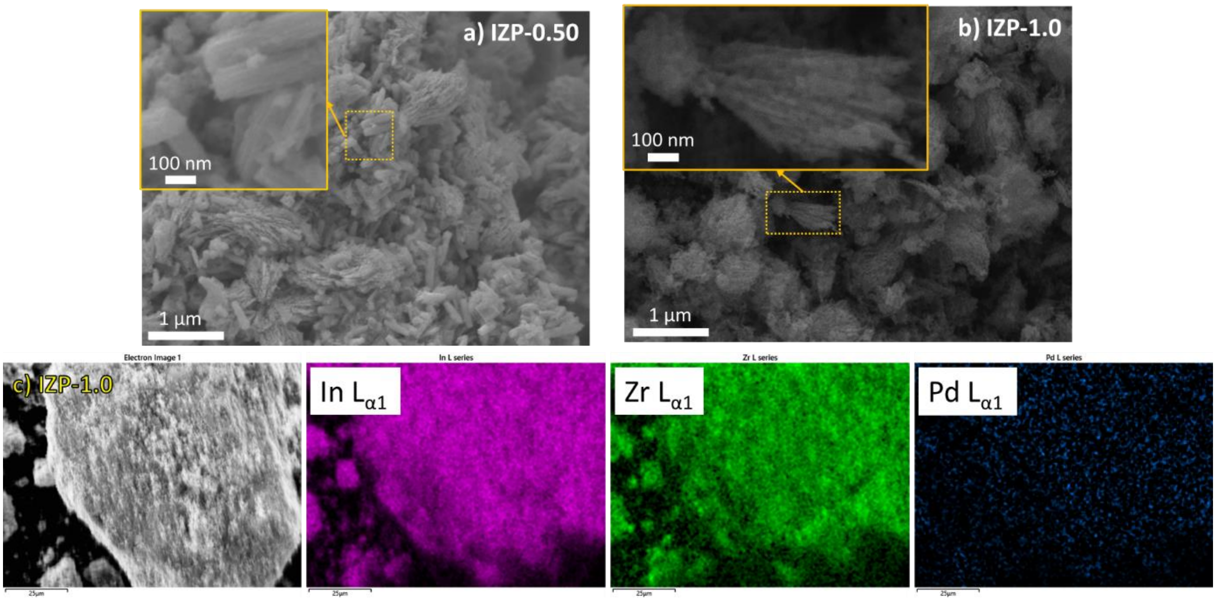

Figure 22 Scanning Electron Microscopy (SEM) images of In$_2$O$_3$-ZrO$_2$-Pd prepared by urea hydrolysis (hydro) method with a Pd loading of (a) 0.50 wt.% and (b) 1.0 wt.%. (c) Energy-Dispersive X-ray Spectroscopy (EDS) analysis of IZP-1.0.

For the Pd-containing samples, both IZP-0.50 and IZP-1.0 have rods smaller than half a micron and some axial layered agglomerate (Figure 22a and Figure 22b), similar to the morphology of the IZ-hydro (Figure 20). The elemental maps of In, Zr, and Pd in the IZP-1.0 sample show overlapping signals between the three elements indicating their homogeneous distributions in the sample (Figure 22c).

3.4 Surface area study

Table 5 Summary characterization table of all the synthesized catalysts: XRD, N_2 adsorption-desorption, CO_2-TPD and O_2-TPD. ”n.d.” stands for ”non-detected”.

Name	***Real Pd wt%***	***XRD***	***N_2 adsorption-desorption***		***CO_2-TPD***	***O_2-TPD***	
		Crystallite size (nm)	**S_{BET} [m^2/g]**	**Total pore V [cm^3]**	**CO_2 adsorbed [µmol/g]**	**O_2 adsorbed [µmol/g]**	**CO_2 released during TPD [µmol/g]**
I-comb	-	39	4.4	0.008	55	*n.d.*	-
I-hydro	-	12	47.4	0.095	149	27	-
I-ammo	-	13	54.8	0.128	274	34	-
IZ-comb	-	29	5.2	0.012	78	*n.d.*	-
IZ-hydro	-	16	58.4	0.145	242	27	-
IZ-ammo	-	12	69.6	0.184	399	28	-
IZ-carb	-	13	69.3	0.298	509	27	51
IZ-oxa	-	15	34.1	0.130	53	7	45
IZP-0.25	0.07	21	41.9	0.112	178	22	-
IZP-0.50	0.14	15	58.4	0.136	206	45	-
IZP-1.0	0.23	18	49.2	0.123	169	40	-
CZA-bench	-	-	39.3	0.136	-	-	-
Z-comb	-	-	3.0	0.009	-	-	-
Z-hydro	-	-	69.4	0.061	144	7	-
Z-ammo	-	-	54.3	0.123	279	8	-

3.4.1 N_2 adsorption-desorption analysis

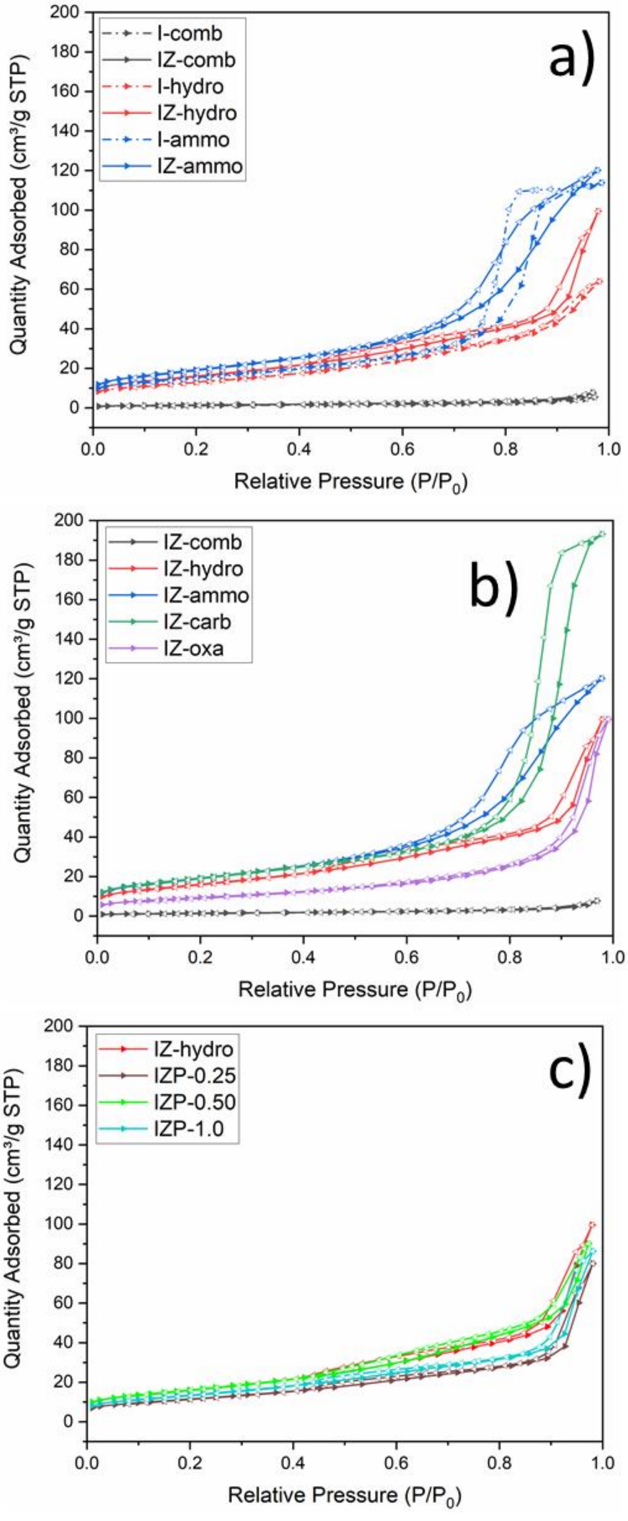

Figure 23 Isotherms of all the different catalysts synthesized: (a) In_2O_3 and In_2O_3-ZrO_2 prepared by comb, hydro and ammo methods; (b) the whole In_2O_3-ZrO_2 catalysts series and (c) In_2O_3-ZrO_2-Pd series prepared by hydro.

Table 6 N_2 adsorption-desorption data.

	S_{BET} [m^2/g]
I-comb	4.4
I-hydro	47.4
I-ammo	54.8
IZ-comb	5.2
IZ-hydro	58.4
IZ-ammo	69.6
IZ-carb	69.3
IZ-oxa	34.1
IZP-0.25	41.9
IZP-0.50	58.4
IZP-1.0	49.2

Figure 23 presents the N_2-physisorption isotherms of the different catalysts. The isotherms of the two combustion samples were attributed to type II, indicating a nonporous or macroporous solid. The isotherms of all the remaining catalysts were classified to type IV with H2 hysteresis loop according to IUPAC classification, which showed a characteristic of mesoporous materials.[104] The combustion method generated the materials having the specific surface area significantly lower than those prepared by the urea hydrolysis and the precipitation. The specific surface areas of I-comb and IZ-comb were 4.4 and 5.2 m^2 g^{-1}, respectively (Table 6Table 5). These values were about 10-15-fold lower than those of other counterparts, e.g., 47.4 m^2 g^{-1} of I-hydro and 69.6 m^2 g^{-1} of IZ-ammo. Remarkably, the mixed oxides of In_2O_3-ZrO_2 catalysts always had higher specific surface areas than their In_2O_3 counterparts for all three synthesis methods. This implied that the inclusion of ZrO_2 improved the specific surface area of the catalysts. For the precipitation using different Na-containing precipitating agents, the IZ-carb had a specific surface area almost the same as the IZ-ammo whereas the IZ-oxa had a surface area of only half of the IZ-carb. For the IZP series, the IZP-0.5 had the same surface area of 58.4 m^2 g^{-1} as the IZ-hydro (the one without Pd) whereas IZP-0.25 and IZP-1.0 had surface areas of 41.9 and 49.2 m^2 g^{-1}, respectively.

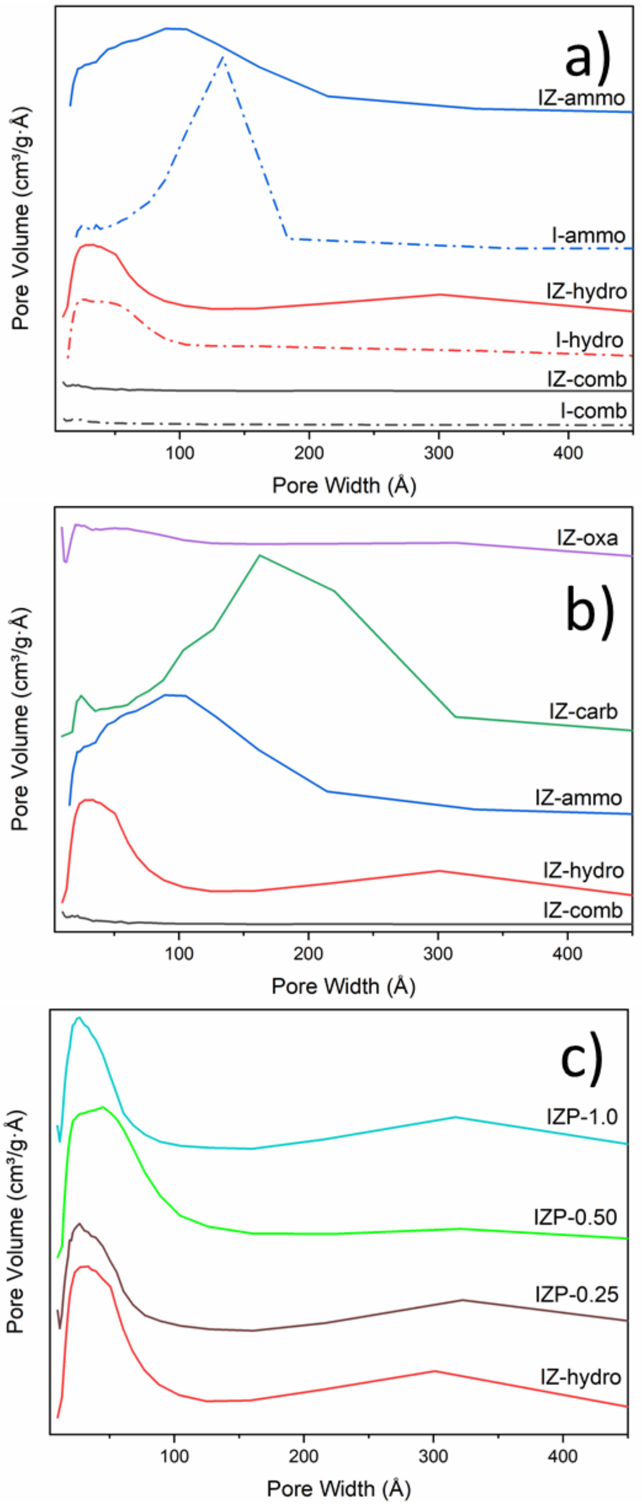

Figure 24 Pore Size Distribution (PSD) of all the different catalysts synthesized: (a) In_2O_3 and In_2O_3-ZrO_2 prepared by comb, hydro and ammo methods; (b) the whole In_2O_3-ZrO_2 catalysts series and (c) In_2O_3-ZrO_2-Pd series prepared by hydro.

The adsorption branch of the isotherms was used to calculate the pore distribution using the BJH method and the results are shown in Figure 24: both two samples prepared by the combustion method (I-comb and IZ-comb) showed a negligible pore volume; I-ammo and I-hydro showed an average pore size of 5 and 14 nm, respectively; IZ-hydro had not only the main pore distribution around 14 nm as the I-hydro but also a broad peak around 30 nm; IZ-ammo showed a broader peak than that of the I-ammo but a smaller average pore size of I-ammo (10 nm versus 14 nm). These results indicate that the presence of Zr modified the porosity of the mixed oxides compared to pure In_2O_3 oxides (Figure 24a).

Both IZ-carb and IZ-oxa had a wide range of pore distribution. However, the former showed two typical peaks at 4 and 19 nm whereas the latter showed no clear peak (Figure 24b). For the IZP series, three Pd-containing samples showed a narrow intensive peak around 14 nm and one broad weak at 30 nm (Figure 24c).

3.4.2 CO_2-TPD (Temperature Programmed Desorption)

Table 7 CO_2 released by different catalysts during CO_2-TPD, previously adsorbed in the analysis.

	CO_2 adsorbed [µmol/g_{cat}]
I-comb	55
I-hydro	149
I-ammo	274
IZ-comb	78
IZ-hydro	242
IZ-ammo	399
IZ-carb	509
IZ-oxa	53
IZP-0.25	178
IZP-0.50	206
IZP-1.0	169

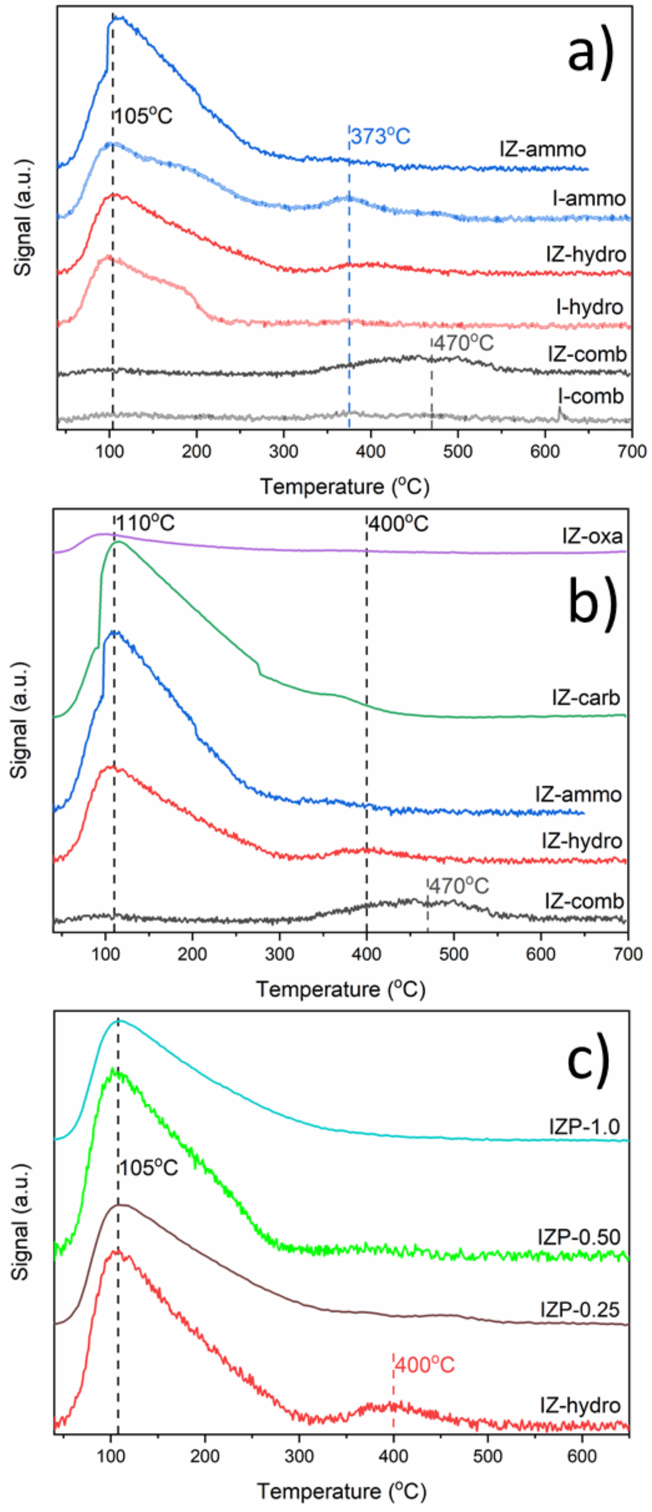

Figure 25 CO_2 Temperature Programmed Desorption (CO_2-TPD) graphs that depict the CO_2 desorbed, during a temperature ramp, by: (a) In_2O_3 and In_2O_3-ZrO_2 prepared by comb, hydro, and ammo methods; (b) the whole In_2O_3-ZrO_2 catalysts series and (c) In_2O_3-ZrO_2-Pd series prepared by hydro.

Figure 25 presents the CO_2-TPD profiles of different catalysts. For In_2O_3, the profile of the I-comb was almost flat while the profiles of I-ammo and I-hydro showed one broad and overlapped peak centered at around 105 °C and one weak peak around 373 °C. The CO_2 uptake of I-ammo and I-hydro was 5-fold and 3-fold higher than that of the I-comb (Table 7). The IZ-comb, IZ-hydro, and IZ-ammo had a similar CO_2-TPD profile to the profiles of their In_2O_3 counterparts, being, however, more intense (Figure 25a). As a result, the CO_2 uptakes of the IZ samples were about 41 - 62 % higher than those of the pure In_2O_3 counterparts (Table 7). The IZ-oxa showed a very weak profile of CO_2-TPD while the IZ-carb had the broadest peak (up to 450 °C, Figure 25b). As a result, the IZ-carb had the highest uptake of CO_2 (509 μmol g^{-1}) which was almost 10-fold higher than that of the IZ-oxa. For the IZP series, the profiles of the Pd-containing samples showed only one broad peak at around 105 °C with an absence of a second peak at high temperature as observed in the profile of IZ-hydro, without Pd (Figure 25c). The CO_2 uptakes of the IZP samples were in a range of 169 – 178 μmol g^{-1}) and without a clear trend in correlation with Pd loading (Table 7).

3.4.3 O_2-TPD (Temperature Programmed Desorption)

Table 8 O_2 released by different catalysts during O_2-TPD, previously adsorbed in the analysis. "n.d." stands for "non-detected".

	O_2 adsorbed [μmol/g_{cat}]
I-comb	*n.d.*
I-hydro	27
I-ammo	34
IZ-comb	*n.d.*
IZ-hydro	27
IZ-ammo	28
IZ-carb	27
IZ-oxa	7
IZP-0.25	22
IZP-0.50	45
IZP-1.0	40

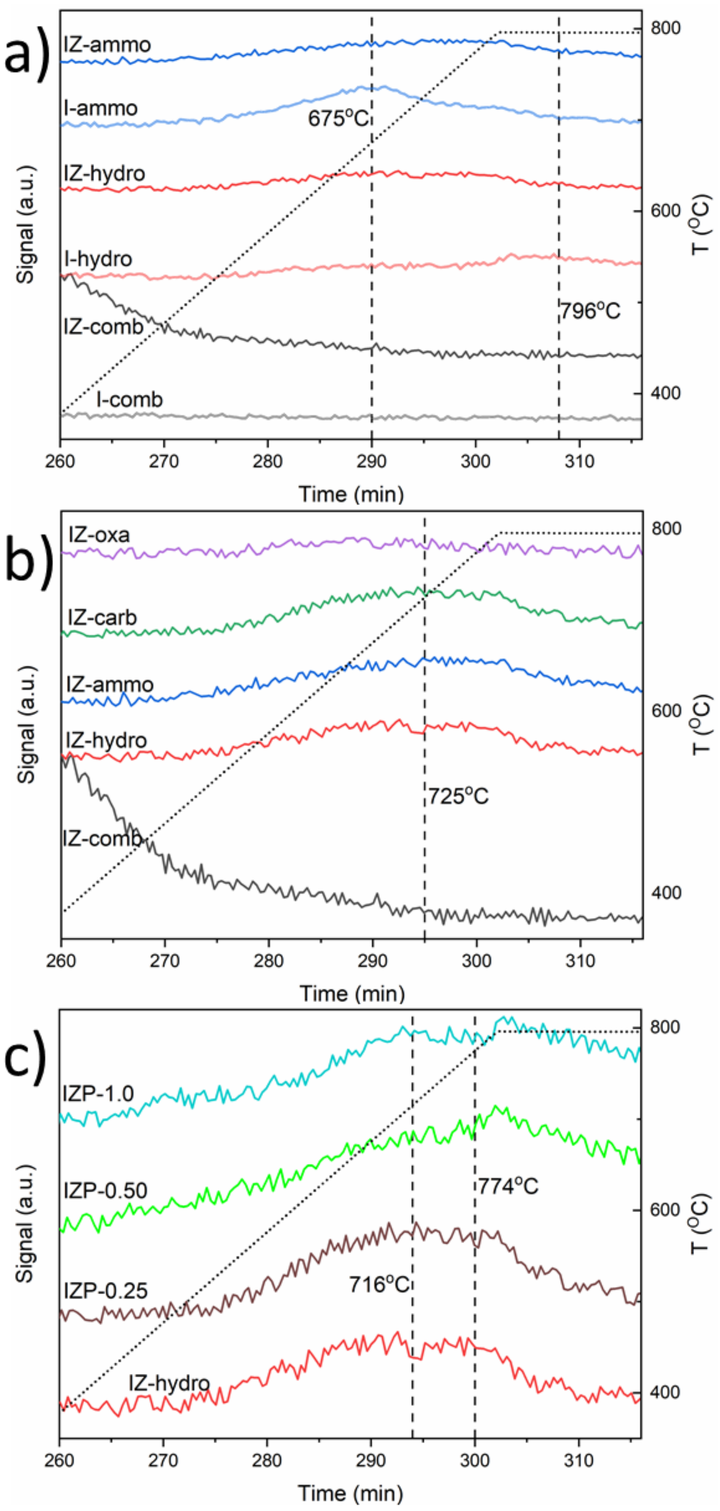

Figure 26 O_2 Temperature Programmed Desorption (O_2-TPD) graphs that depict the O_2 desorbed, during a temperature ramp, by: (a) In_2O_3 and In_2O_3-ZrO_2 prepared by comb, hydro, and ammo methods; (b) the whole In_2O_3-ZrO_2 catalysts series and (c) In_2O_3-ZrO_2-Pd series prepared by hydro.

Figure 26 presents the O_2-TPD profiles of different catalysts. All the profiles showed O_2 desorption peaks above 670 °C which is far from the temperature range between 250 and 350 °C for the catalytic test. The O_2 desorbed values were around 30 µmol/g, except for I-comb, IZ-comb, and IZ-oxa whose had negligible uptakes of O_2. The IZP-0.5 and IZP-1.0 had higher uptake of O_2, perhaps due to the release of O_2 from PdO.[105]

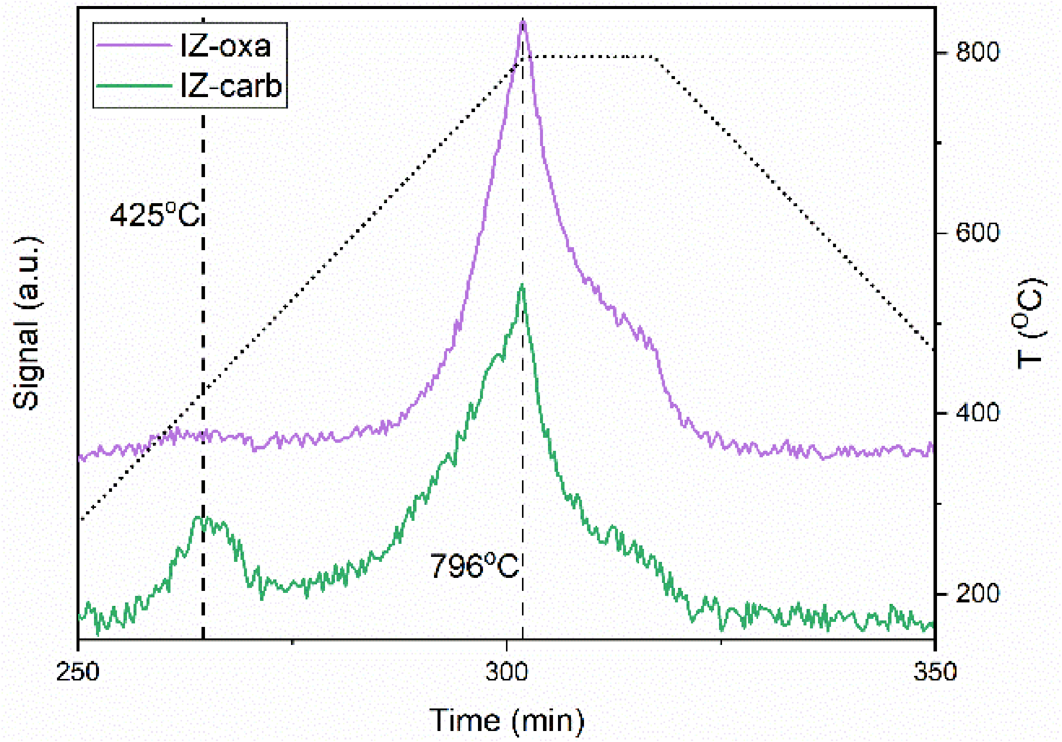

Figure 27 CO_2 released by IZ-carb and IZ-oxa during the O_2-TPD, caused by residues of the C-containing precipitating agents used during their synthesis.

The mass number of CO_2 (m/z = 44) was also tracked to investigate whether CO_2 could be released during the O_2-TPD measurements for IZ-carb and IZ-oxa since C-containing precipitating agents (sodium carbonate and sodium oxalate) were used during the catalyst preparation. The IZ-oxa showed two distinct peaks of CO_2 desorption at 425 and 780 °C whereas the IZ-carb released CO_2 with one peak at around 780 °C (Figure 27). It was noted that these catalysts were calcined at 500 °C for 6 h. The data suggested that a part of carbon sources was still stable in the structure of the catalyst above the calcination temperature at 500 °C and this was desorbed at 780 °C as observed in the O_2-TPD. Moreover, after calcination, the IZ-oxa might adsorb again CO_2 from the atmosphere and this perhaps explained the desorption of CO_2 at 425 °C observed in the O_2-TPD profile.

3.5 Redox properties study

3.5.1 H_2-TPR (Temperature Programmed Reduction)

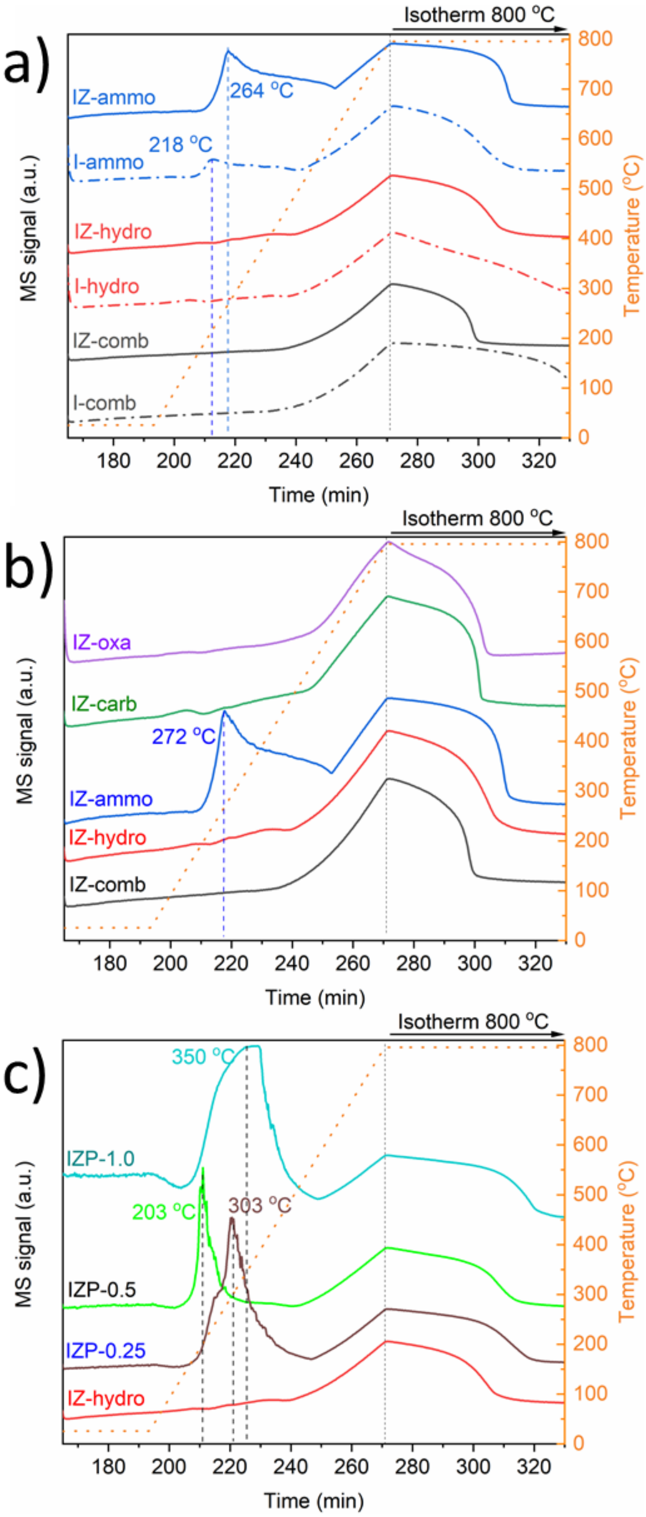

Figure 28 Temperature Programmed Reduction (H_2-TPR) of (a) In_2O_3 and In_2O_3-ZrO_2 prepared by comb, hydro and ammo methods; (b) the whole In_2O_3-ZrO_2 catalysts series and (c) In_2O_3-ZrO_2-Pd series prepared by hydro.

H_2-TPR is a useful technique to study the redox properties of a solid sample: Figure 28 presents the H_2-TPR profiles of different catalysts. Pure ZrO_2 showed a negligible consumption of H_2 with a flat profile during the analysis. The profile of I-comb and I-hydro showed only one reduction feature at a high-temperature range of 400 – 800 °C whereas the profile of I-ammo had also another peak at around 270 – 295 °C (Figure 28a). The peak at low temperature is associated with the reduction of surface In_2O_3 while the peak at high temperatures could be attributed to the reduction of bulk In_2O_3.[45,102] The profiles of IZ samples showed similar features as their pure In_2O_3 counterparts. The synthesis method using ammonia solution as precipitating agent facilitates a reduction of In_2O_3 at lower temperatures, on the contrary of all the other preparation methods (Figure 28b). For the IZP series, all three Pd-containing samples showed two temperature peaks in the profile, unlike the one without Pd (IZ-hydro) which had only one reduction peak at high temperature (Figure 28c). This could be attributed to the reduction of either PdO or the surface In_2O_3. However, PdO was usually reduced at temperatures lower than 200 °C[65,66,106] and the loadings of Pd were substantially low. Therefore, the low-temperature peaks in these catalysts were likely involved in the reduction of surface In_2O_3, indicating that Pd can induce such a reduction.

3.5.2 X-ray Photoelectron Spectroscopy (XPS) analysis

Table 9 Ratio (%) of different oxygen (O) species deconvoluted from O1s binding energy

	Lattice O (%)	O-defect (%)	Surface O (%)
I-comb	72	17	12
I-hydro	68	21	11
I-ammo	71	18	12
IZ-comb	62	29	9
IZ-hydro	67	24	9
IZ-ammo	86	7	7
IZ-oxa	78	18	7
IZ-carb	77	19	5
IZP-1.0	71	21	9

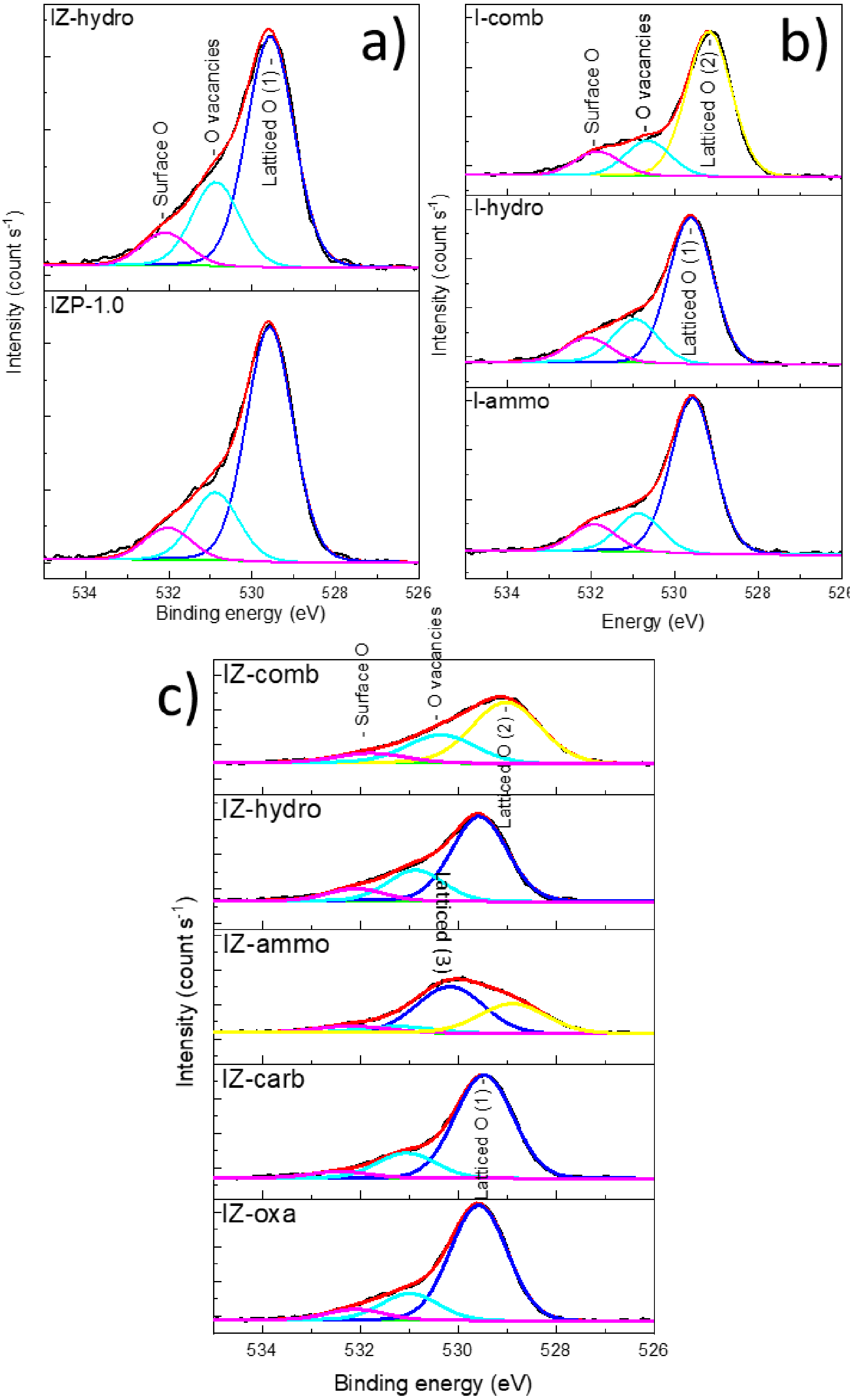

Figure 29 X-ray Photoelectron Spectroscopy (XPS) O1s of (a) In_2O_3-ZrO_2 and In_2O_3-ZrO_2-Pd prepared by hydro (IZ-hydro and IZP-1.0); (b) the whole In_2O_3 catalysts series and (c) the whole In_2O_3-ZrO_2 series.

X-ray Photoelectron Spectroscopy (XPS) was performed to investigate the redox surface properties of the catalysts. The O1s core level spectra of the catalysts are shown in Figure 29. The peak of O1s of each sample can be deconvoluted into three peaks around 529 – 530 eV, 530.5 – 531.5 eV, and 532 – 533 eV corresponding to O-lattice, O-defect (O_v), and O-adsorbed species, respectively.[42,107] All the samples showed a similar distribution of oxygen species (Table 9): 62 - 77 % for lattice O, 5 – 12 % of surface O, and 18 – 29 % of O_v. The only exception appears to be IZ-ammo, with an 86 % of O-lattice (considering both In_2O_3 and ZrO_2), 7 % of O-defect, and another 7 % as O_v.

The $In3d_{5/2}$ showed the binding energy around 444 eV which attributed to the oxidation state of +3 of In in all the samples. The XPS-Pd of IZP-1.0 had too much background noise and the Pd signal was too weak to be detected, most certainly for the low wt.% loading of Pd in the catalyst.

3.6 Catalytic test

The catalytic activity of different catalysts for CO_2 hydrogenation was performed in a fixed-bed reactor operated in a temperature range from 250 to 350 °C and pressure of 40 bars. The mass of each catalyst was normalized to obtain the same amount of 500 mg of Indium for comparison purposes. During the tests, CH_3OH was produced via CO_2 hydrogenation (Reaction (7)) and CO was generated via reverse water-gas shift reaction (RWGS, Reaction (8)):

(7) $CO_2 + 3H_2 \rightleftharpoons CH_3OH + H_2O$, $\Delta H° = -49.4$ kJ mol^{-1}

(8) $CO_2 + H_2 \rightleftharpoons CO + H_2O$, $\Delta H° = -41.2$ kJ mol^{-1}

The reaction (7) generally follows the formate (HCOO*) pathway[49,56] and thus CH_4 is likely formed as a by-product (Reaction (9)), since hydrogenation of CO_2 to methane is possibly involved in a similar pathway:[108]

(9) $CO_2 + 4H_2 \rightleftharpoons CH_4 + 2H_2O$, $\Delta H° = -165.0$ kJ mol^{-1}

In all the catalytic tests in this study, CH_3OH and CO were the main products whereas CH_4 was only found in some cases. However, the maximum selectivity of CH_4 was lower than 2.5% in all tests, and hence the selectivity in CH_4 was not reported in the results to simplify the evaluation. The comparison of the catalytic activity between the catalysts was assessed in terms of CO_2 conversion (X_{CO2}), CH_3OH selectivity (S_{CH3OH}), and space-time yield of CH_3OH (STY_{CH3OH}). For comparison purposes, the catalytic test of the benchmark CZA-bench catalyst was also performed.

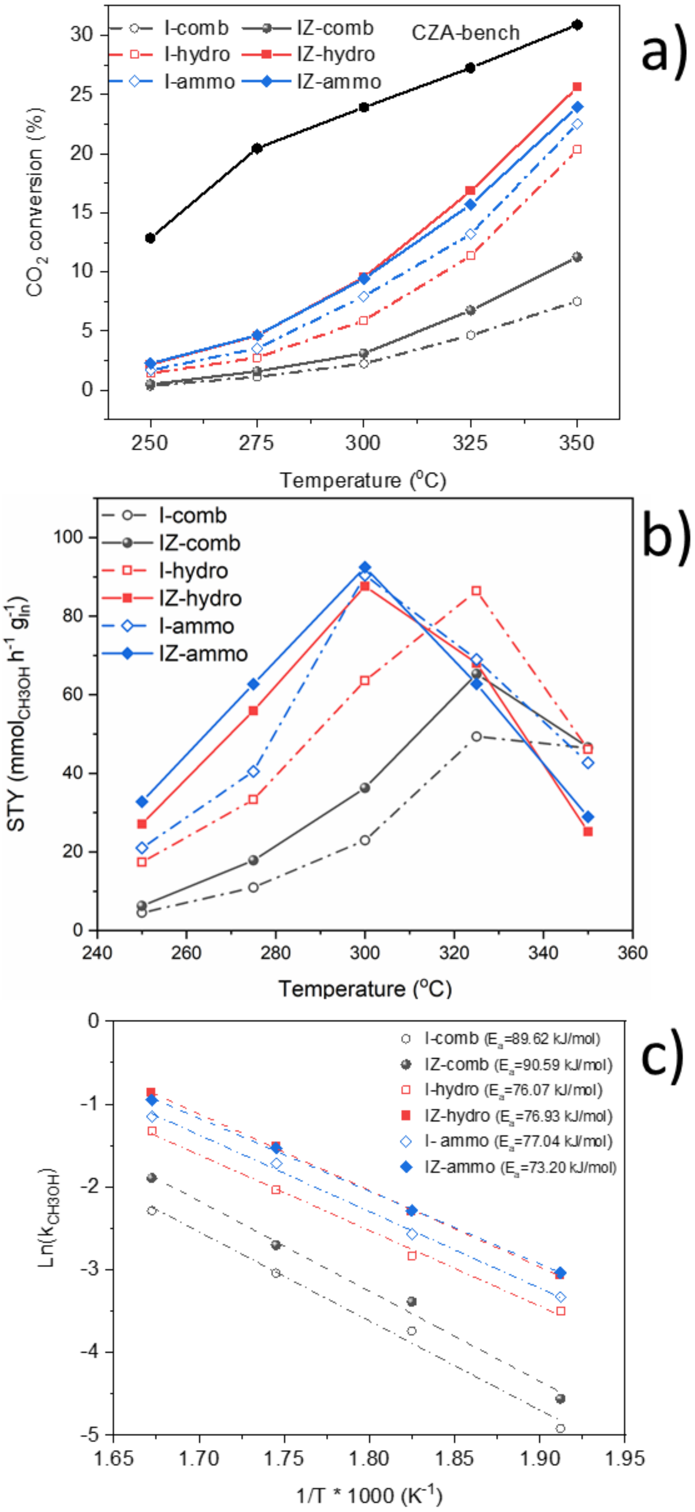

Figure 30 Comparison of In_2O_3 and In_2O_3-ZrO_2 catalysts on (a) CO_2 conversion, (b) STY of CH_3OH, and (c) apparent activation energy.

Figure 30 presents the activity performance of In_2O_3 and In_2O_3-ZrO_2 prepared by combustion, urea hydrolysis, and precipitation with NH_4OH solution. For all catalysts, CO_2 conversion increased substantially as increasing temperature from 250 to 350 °C (Figure 30a). For sole In_2O_3, the CO_2 conversion increased with an order of I-comb << I-hydro < I-ammo in the whole range of temperature from 250 to 350 °C (Figure 30a, dashed lines).

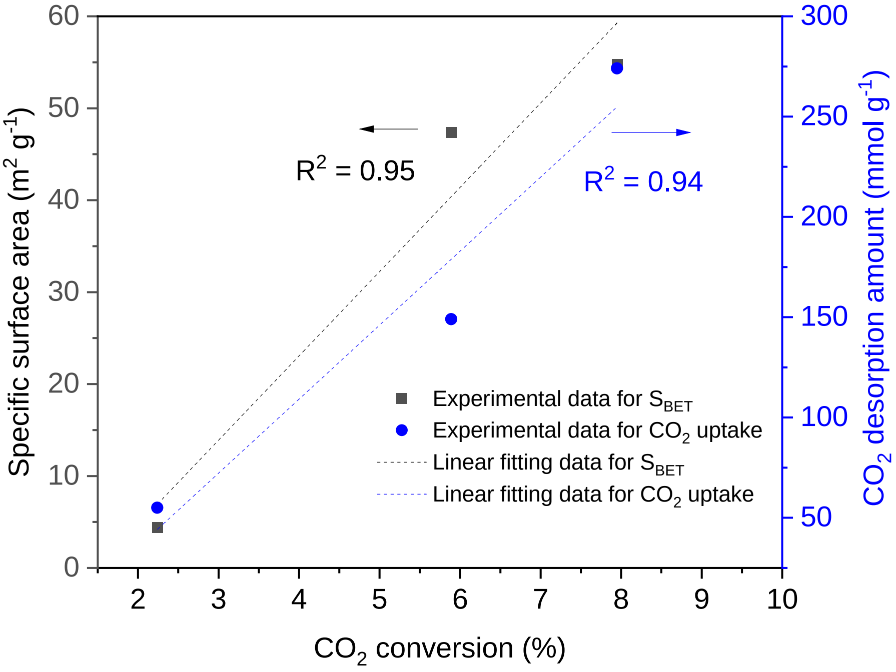

Figure 31 Fitting of CO_2 conversion with both the specific surface areas and CO_2 desorption amount during CO_2-TPD.

The CO_2 conversions were linearly fit with both the specific surface areas and CO_2 desorption amount (Figure 31), suggesting the specific surface area plays a crucial role in the CO_2 conversion since all three catalysts had the same cubic structure of In_2O_3 (Figure 18). Significantly low conversion of CO_2 on I-comb catalyst was accounted by a substantially low specific surface area of the catalyst. It is noted that the CO_2 conversions of I-hydro and I-ammo are better to some extent than those reported in the literature under similar or milder reaction conditions (Table 10). For example, In_2O_3 prepared by the precipitation with Na_2CO_3 showed a conversion of 11.8% at 350 °C under similar reaction conditions,[109] whereas other works reported much lower CO_2 conversion even under milder reaction conditions (e.g., lower WHSH, reactants diluted with inert gasses, …).[102,110] Both I-hydro and I-ammo catalysts showed CH_3OH selectivity of 42-45% for temperature 250-300 °C and the selectivity decreased rapidly with a further increase in temperatures due to thermodynamic favor for RWGS reaction. The I-comb catalyst also had a similar value of CH_3OH selectivity as I-hydro and I-ammo at temperatures from 250-350 °C but it lost CH_3OH selectivity when the temperature was higher than 325 °C. The yield of CH_3OH production on each catalyst is a trade-off between the CO_2 conversion and CH_3OH selectivity due to a competition between the methanol generation reaction and the RWGS reaction. As a result, the maximum CH_3OH production rate calculated per gram of Indium ($mmol_{CH3OH}\ g_{In}^{-1}\ h^{-1}$) was ranked in increasing order of I-comb (49.37 at 325 °C) < I-hydro (86.44 at 325 °C) < I-ammo (90.42 at 300 °C). The CH_3OH production rates normalized with the mass of the catalysts were 40.80, 71.43, and 74.73 $mmol_{CH3OH}\ g_{cat}^{-1}\ h^{-1}$ for I-comb, I-hydro, and I-ammo, respectively. This implies that the preparation method strongly influences the catalytic performance for CO_2 hydrogenation to CH_3OH. It is noted that the CH_3OH production rates for I-hydro and I-ammo are promising compared to those reported for In_2O_3 catalysts in the literature (Table 10). In the literature, CO_2 conversion, methanol selectivity, and methanol formation are usually correlated to the content of O vacancy;[35,44,52] however, in this work the correlation between O vacancy and the methanol production rate was not clear.

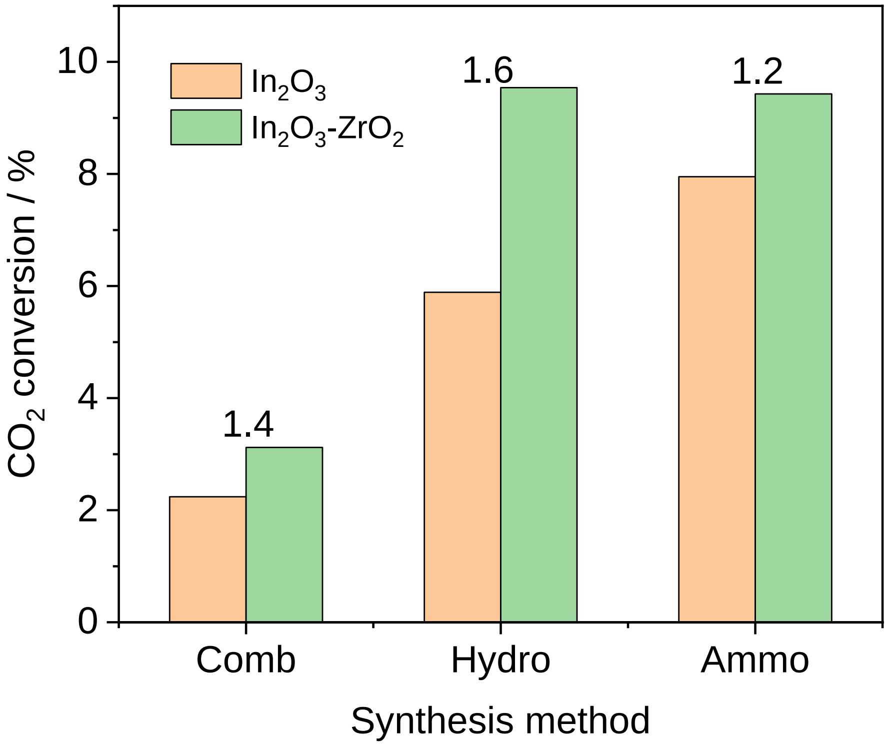

Figure 32 Comparison of In_2O_3's and In_2O_3-ZrO_2's CO_2 conversion of catalysts synthesized with the same preparation method.

The apparent activation energies calculated from Arrhenius plots (for the conversion of CO_2 below 20%) were approximately 90, 76, and 77 kJ mol^{-1} for I-comb, I-hydro, and I-ammo, respectively (Figure 30c). Different values of activation energy for CO_2 hydrogenation on cubic In_2O_3 catalysts have been reported in the literature,[110] e.g., from 55 to 101 kJ mol^{-1}. It should be noted that it is only fair when comparing the apparent activation energy for catalysts tested under similar reaction conditions because the apparent activation energy values depend on not only the type of catalysts but also the operating conditions, i.e., feed compositions and treatment conditions.[111] Similar values of activation energy for I-hydro and I-ammo suggest that the reaction mechanism was perhaps similar for both catalysts.

Each mixed oxide of In_2O_3-ZrO_2 catalyst prepared by three different methods showed higher CO_2 conversion than that on its In_2O_3 counterpart (Figure 32; Figure 30a, each lines pair with the same color). This indicated the advantage of ZrO_2 support in the mixed oxide In_2O_3-ZrO_2 catalysts. IZ-hydro and IZ-ammo catalysts showed very similar CO_2 conversion up to 300 °C but IZ-hydro gets over IZ-ammo at higher temperatures (Figure 30a, solid lines). Both catalysts outperformed the IZ-comb for the conversion of CO_2 from 250 to 35 °C. This indicates that the preparation method significantly influences the CO_2 conversion for In_2O_3-ZrO_2 catalysts likely for the In_2O_3 series. Both IZ-hydro and IZ-ammo showed the maximum rate of CH_3OH at 300 °C, 87.61 and 92.44 mmol g_{In}^{-1} h^{-1}, respectively, whereas IZ-comb had the maximum rate of CH_3OH about 65.30 mmol g_{In}^{-1} h^{-1} at 325 °C. It is noted that the IZ-hydro had a mixed phase of rhombohedral and cubic In_2O_3 while IZ-ammo possessed only cubic In_2O_3; however, they had similar CO_2 conversion and CH_3OH yield, suggesting that there seemed to have no significant difference in the activity between the two phases. In the literature, cubic In_2O_3 has been reported to be more active than rhombohedral In_2O_3 without support.[110] The discrepancy may be related to the role of ZrO_2 in our catalysts. A high CH_3OH formation rate for In_2O_3-ZrO_2 than the In_2O_3 counterpart was correlated to the enhancement of ZrO_2 to the specific surface area and CO_2 adsorbed amount. Furthermore, the apparent activation energy of In_2O_3-ZrO_2 was close to that of In_2O_3 counterpart prepared with the same synthesis method, indicating a similar reaction pathway between each pair of the catalysts.

The catalytic performance of a benchmark CuZnAl catalyst (Cu/Zn/Al = 60/30/10 molar ratio) was also performed and compared with In_2O_3 and In_2O_3-ZrO_2 catalysts. The CuZnAl catalyst had a much higher CO_2 conversion than the Indium-based catalyst. However, this catalyst favored strongly the RWGS, especially at a temperature higher than 300 °C and as a result, it showed a lower CH_3OH yield than IZ-hydro, IZ-ammo, and I-ammo from 300 to 350 °C (Figure 30b). This is the advantage of an Indium-based catalyst compared to a Cu-based catalyst for CO_2 hydrogenation to CH_3OH.[112]

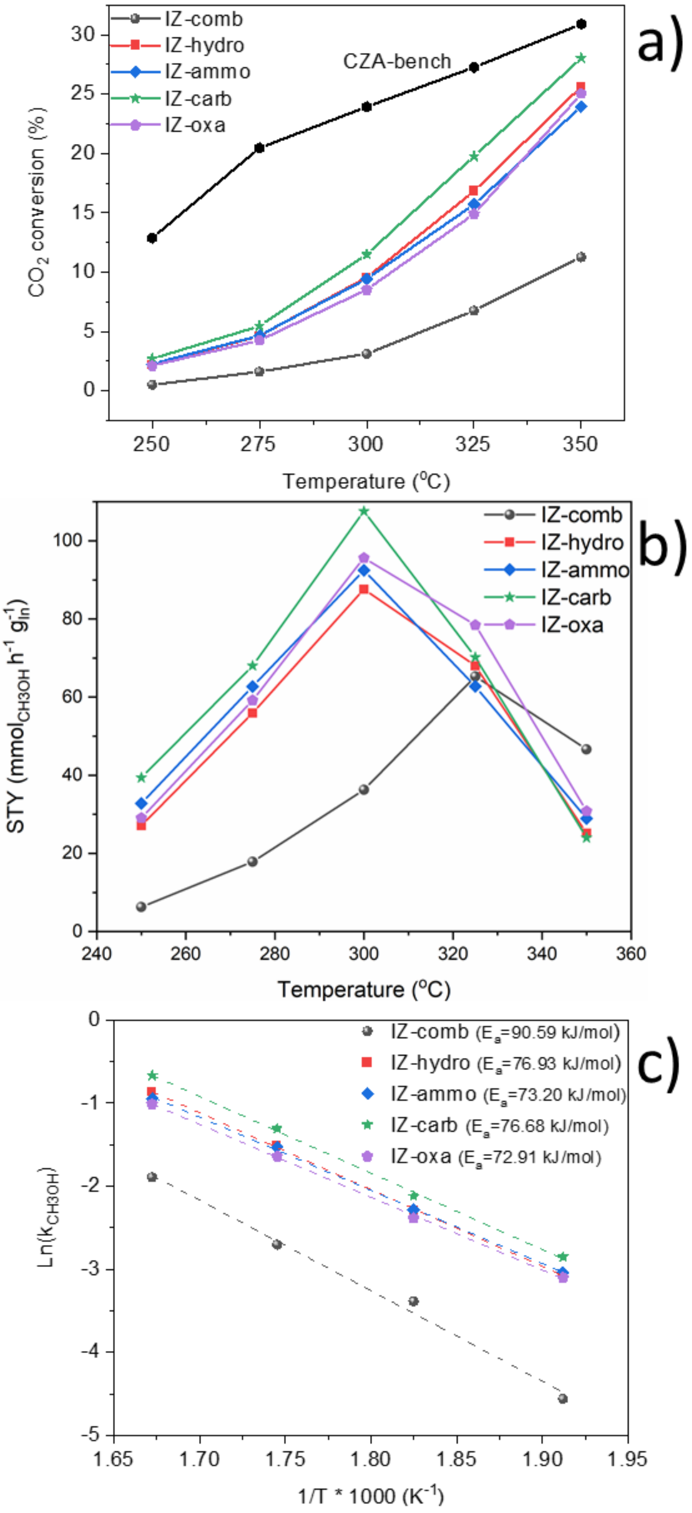

Figure 33 Comparison of In_2O_3-ZrO_2 catalysts on (a) CO_2 conversion, (b) STY of CH_3OH, and (c) apparent activation energy.

Three synthesis methods, namely combustion, urea hydrolysis, and precipitation with NH_4OH, are free-sodium routes. To extend further the effect of the synthesis method, other two catalysts of In_2O_3-ZrO_2 were synthesized with precipitation using Na_2CO_3 and $Na_2C_2O_4$ as precipitating agents and tested for CO_2 hydrogenation to CH_3OH. A comparison of the catalytic performance of these two catalysts IZ-carb and IZ-oxa with others is shown in Figure 33. IZ-oxa showed comparable performance with IZ-hydro and IZ-ammo in terms of CO_2 conversion (Figure 33a), CH_3OH yield, and formation rate whereas the IZ-carb was the best among five samples of In_2O_3-ZrO_2. This catalyst had an 11.49 % conversion of CO_2, 4.22 % yield of CH_3OH at 300 °C, and a methanol STY of 107.54 mmol g_{In}^{-1} h^{-1}. The best activity of IZ-carb may be related to the textural properties, for example, large specific surface and substantially large in total pore volume compared to those of the others (Table 5). However, the textural properties may not account entirely for a comparable rate of CH_3OH formation with the IZ-hydro and IZ-ammo since the IZ-oxa had a specific surface area of approximately half of IZ-hydro and IZ-ammo.

In this study, three catalysts of In_2O_3-ZrO_2 with different Pd loadings were prepared with the urea hydrolysis method and the results of the catalytic activity are shown in Figure 34. Note that the real loading of Pd in each sample was lower than the nominal one with a factor of 4.8 (Table 3). Both IZP-0.25 and IZP-0.5 had a higher conversion and CH_3OH selectivity than the sample without Pd (IZ-hydro) whereas the IZP-1.0 had lower CH_3OH selectivity at temperatures higher than 275 °C. Overall, the maximum rate of CH_3OH formation was ranked in increasing order of IZ-hydro < IZP-1.0 < IZP-0.25 < IZP-0.5. All catalysts had comparable apparent activation energy in a range of 73-77 kJ mol^{-1} indicating a similar reaction mechanism (Figure 34c). The catalytic performance suggests that the incorporation of Pd enhanced the CH_3OH selectivity but with a certain loading, e.g., 0.14 wt.%, whereas a high loading (e.g., 0.25 wt.%) favored more CO selectivity and thus decreased the space-time yield of CH_3OH. We hypothesized that the best performance of IZP-0.5 is perhaps related to three main factors including high specific surface area, ease of reduction, and its optimum cluster size of Pd compared to IZP-1.0. It has been reported in the literature that the size of the Pd cluster is very important to restrict the RWGS reaction on Pd sites and the Pd cluster size strongly depends on the preparation method.[66] The CH_3OH formation rate of IZP-0.5 was very promising compared to those reported in the literature for Pd-containing catalysts (Table 10).

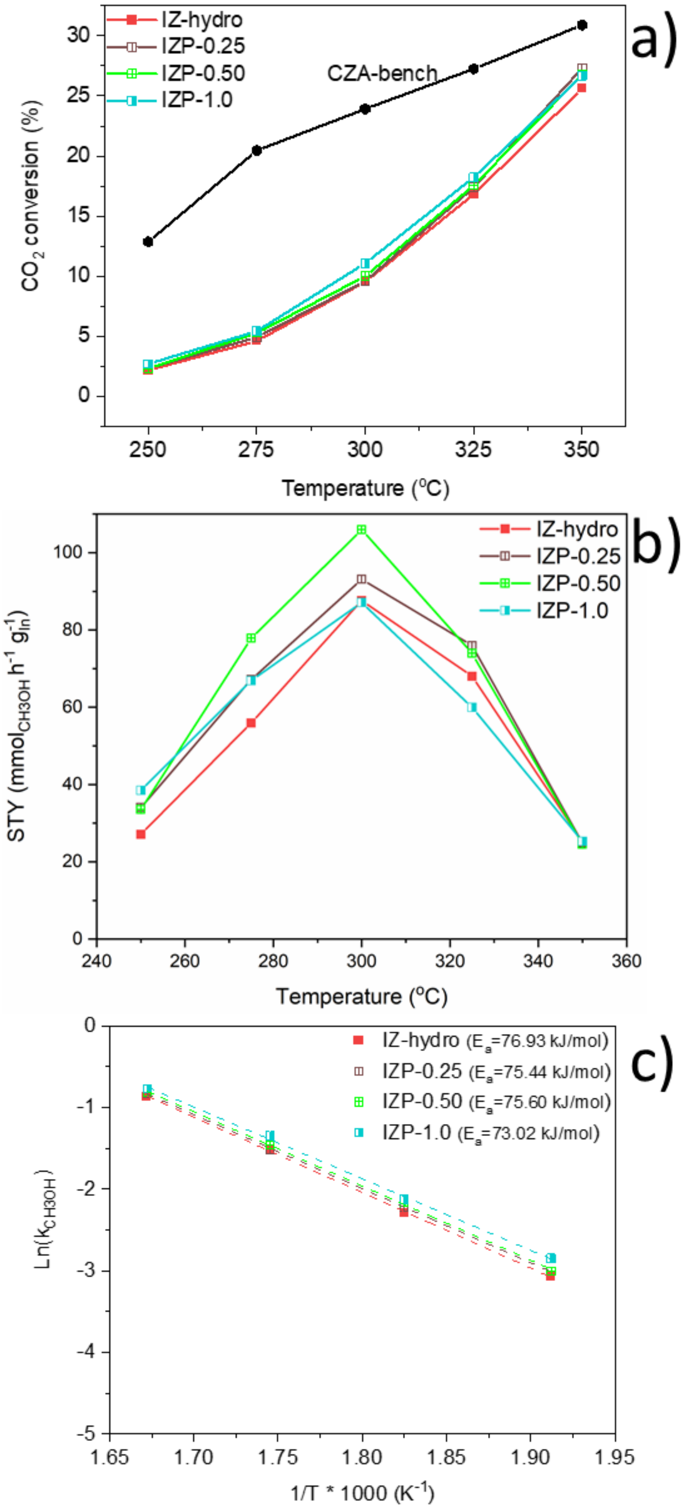

Figure 34 Comparison of In_2O_3-ZrO_2-Pd catalysts on (a) CO_2 conversion, (b) STY of CH_3OH, and (c) apparent activation energy.

3.6.1 Activity comparison with literature

In Table 10 below, there is a summary table that compares the activity performances of the catalysts studied in this project (bottom of the table) and the catalysts studied in the recent literature (top of the table):

*Table 10 Comparison of the activity performance of the catalysts reported in this study and recent literature (*per grams of In).*

Catalysts	**CO_2/H_2/inert (v/v)**	**Space velocity**		**Pressure (MPa)**	**Temperature (K)**	**CO_2 conversion (%)**	**CH_3OH formation**		**Ref**
		GHSV (h^{-1})	**WHSV ($L\ g^{-1}\ h^{-1}$)**				**STY ($mmol\ g_{cat}^{-1}\ h^{-1}$)**	**Selectivity (%)**	
In_2O_3	1/4	16000	26	5	573	-	ca. 6.3	100	42
In_2O_3/ZrO_2	1/4	16000	26	5	573	5.2	9.2	100	
$In_{2.5}$/ZrO_2	1/4/1.67	24000		5	523	0.9	1.1	74	55
Hexagonal-In_2O_3	1/3/0.55	-	21.6	4	598	4.4	6.3	68	113
Pd/In_2O_3 (precipitate)	1/4/0	-	21	5	573	20	27.8	70	45
Pd/In_2O_3 (Impregnation)	1/4/0	-	21	5	573	18	25.0	70	
In:Pd (2:1)/SiO_2	1/4/1.5	-	7.5	4	573	-	18.4	61	65
Pd- In_2O_3 (CP)	1/4/0	-	48	4	553	-	31.6	78	66
1.5Y9In/ZrO_2	1:4/1.5	-	52	4	573	7.6	13.1	69	107
3La10In/ZrO_2	1/4/1.5	-	52	4	573	7.7	13.1	66	
In_2O_3	1/3/1	-	9	2	593	~5	14.6	~39	102
20In/ZrO_2-800	1/3/1	-	9	2	593	~5	59.6	~51	
c-In_2O_3	1/4/0	-	16	4	613	~ 12	3.0	20	110
rh-In_2O_3	1/4/0	-	16	4	613	~ 5	1.8	30	
In_2O_3-commercial	1/3/1	-	15	4	543	1.1	0.8	55	43
In_2O_3-commercial	1/3/1	-	15	4	603	7.1	3.7	40	
In_2O_3 (hydrolysis)	1/3/0	-	12*	4	598	11.4	2.8*	31	This work
In_2O_3 (carbonate)	1/3/0	-	12*	4	573	9.5	2.8*	36	
In_2O_3-ZrO_2-hydro	1/3/0	-	12*	4	573	11.5	3.5*	37	
Pd- In_2O_3-ZrO_2-hydro	1/3/0	-	12*	4	573	10.0	3.4*	42	

3.6.2 Stability test

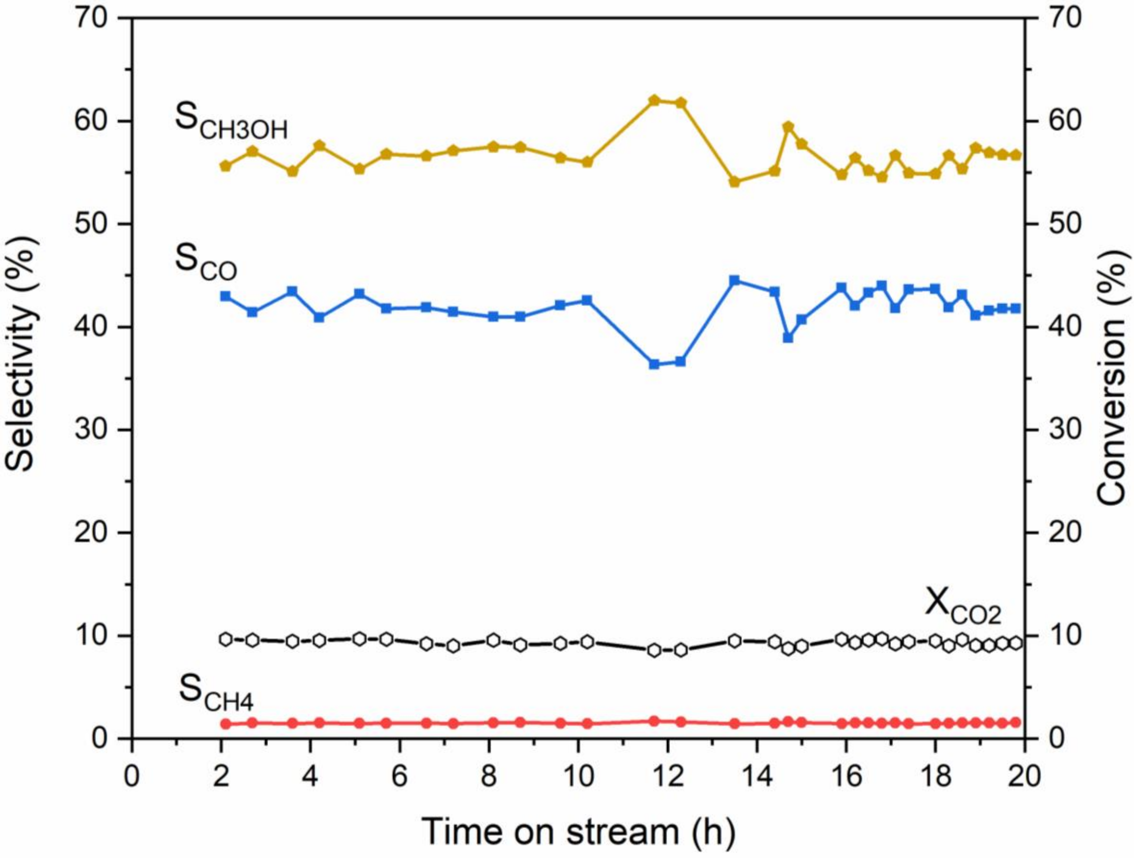

Figure 35 IZP-0.50 stability test over 20 hours.

A stability test was performed on the catalyst IZP-0.50 at 300 °C for 20 h and the data are presented in Figure 35. At the beginning of the test, the conversion of CO_2 (X_{CO2}) was approximately 9.6 % and the selectivity in CH_3OH (S_{CH3OH}) and CO (S_{CO}) was 42.3 % and 56.2 %, respectively. The selectivity in CH_4 (S_{CH4}) was negligible (less than 1.5 %). Almost the same values of CO_2 conversion and the selectivity were observed after 20 h of time-on-stream, suggesting that the catalyst was stable during the test: X_{CO2} was 9.3 %, S_{CH3OH}, $S_{CO,}$ and S_{CH4} were 41.8 %, 56.7 %, and 1.6 %, respectively. The selectivity in CH_4 was negligible (less than 1.5 %). Under this condition, the space-time yield of CH_3OH of the IZP-0.5 catalyst was 1.89 g_{MeOH} h^{-1} $g^{-1}_{catalyst}$ (3.32 g_{MeOH} h^{-1} g^{-1}_{Indium}), higher than the successful stability test result with a Pd-promoted In_2O_3 catalyst, reported by Frei, *et al.*[66] in 2019 (0.96 g_{MeOH} h^{-1} $g^{-1}_{catalyst}$), that employed different operating conditions.

3.7 Post-reaction characterization

Some of the used catalysts were selected and analyzed with XRD, N_2 physisorption, and XPS to investigate any changes in the structure and surface composition of the catalysts after the reactions. The properties of the different spent catalysts are listed in Table 11 hereafter:

Table 11 Characterization table of different spent catalysts

	Fresh catalyst		**Spent catalyst**	
	XRD crystallites size (nm)	**S_{BET} [m^2/g]**	**XRD crystallites size (nm)**	**S_{BET} [m^2/g]**
I-hydro	12	47.4	14	25.2
I-ammo	13	54.8	17	32.2
IZ-hydro	16	58.4	21	35.5
IZ-ammo	12	69.6	14	58.6
IZ-carb	13	69.3	12	58.5
IZ-oxa	15	34.1	-	29.4
IZP-0.25	21	41.9	-	28.4
IZP-0.50	15	58.4	15	34.6
IZP-1.0	18	49.2	21	32.9

3.7.1 X-Ray Diffraction (XRD)

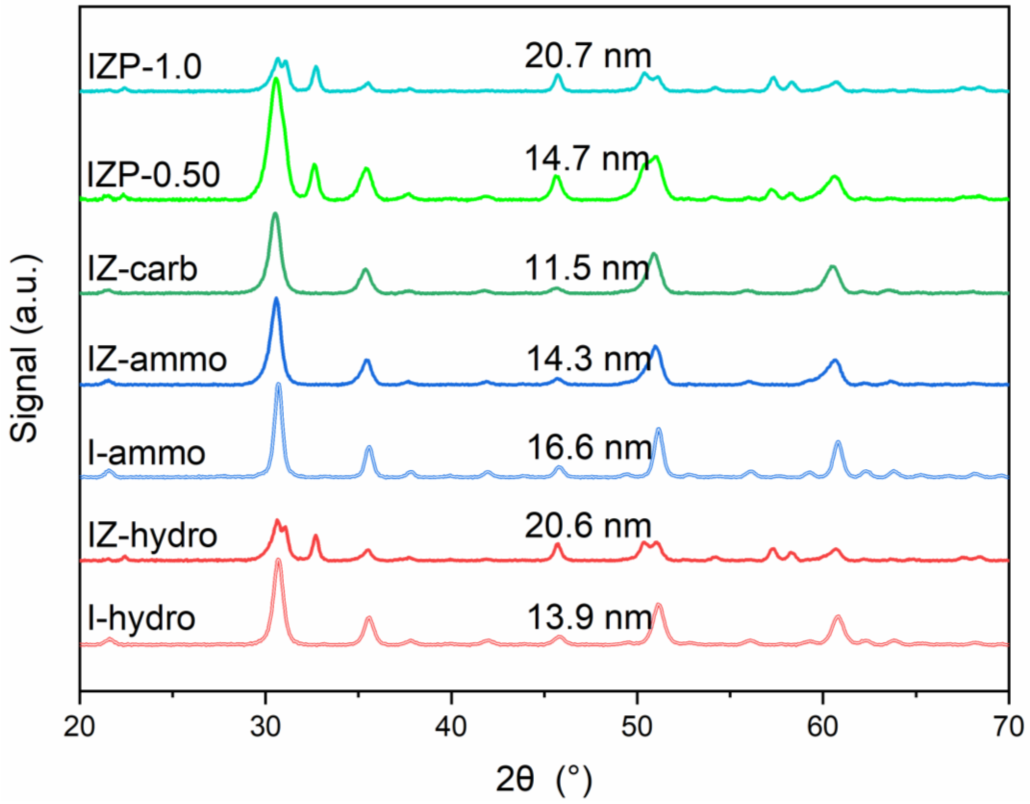

Figure 36 X-Ray Diffraction (XRD) of different spent catalysts. The crystallites sizes, calculated for the plane (431), are marked in the graph.

Figure 36 presents the XRD patterns of the spent catalysts. The used catalyst showed the same XRD pattern as its fresh counterpart, suggesting there was no change in the structure of the catalyst after the reaction. However, the crystalline size calculated from the Scherrer equation for the plane (431) was slightly increased from 1-5 nm due to the sintering phenomenon, except for IZ-carb and IZP-0.50 (Table 11).

3.7.2 N_2 adsorption-desorption analysis

The porosity of the mesoporous material has not been modified with the catalytic test. Nevertheless, the specific surface areas were decreased by almost a half for all the catalysts and the total pore size volume drastically decreased for most of the catalysts studied, except for IZ-oxa, which did not show any change (Table 11).

3.7.3 X-ray Photoelectron Spectroscopy (XPS) analysis

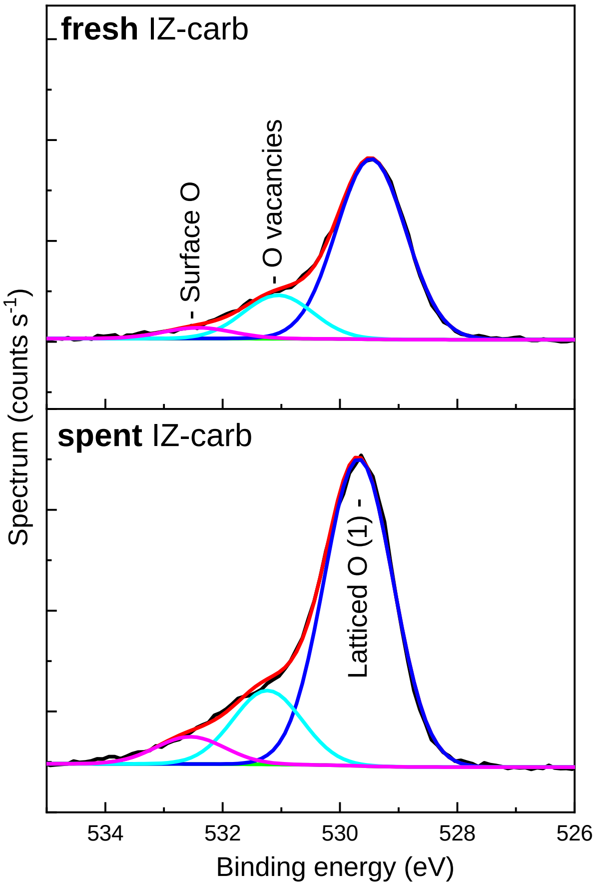

Figure 37 XPS of fresh and spent IZ-carb.

Table 12 XPS areas signal ratio for fresh and spent IZ-carb

Peak notation	Chemical states	IZ-carb-Fresh	IZ-carb-spent
O1s	In_2O_3	77 %	75 %
	Oxy. Vac. in ZrO_2 -rich/-like structure	18 %	18 %
	Zr-OH	5 %	7 %

XPS was carried out with the sample IZ-carb, both fresh and spent, after the catalytic test: its data suggested that the oxidation state of In remained identical, but since this XPS has been operated *ex-situ*, a re-oxidation by atmospheric conditions should not be excluded. The percentage of oxygen vacancy, as well, was not changed substantially (Figure 37 and Table 12); a similar trend in the O1s spectra has been reported previously.[114]

4. Conclusions

All the preparation methods adopted in this thesis were reliable for the synthesis of In-based catalysts, with the only exception of the urea combustion method (comb). During the comb synthesis, an In mass loss occurred together with the formation of two different oxides phases instead of the most common solid solution of In_2O_3 and ZrO_2; additionally, the comb samples had poor catalytic performance and poor textural properties. The same structure of cubic In_2O_3 was found on the pure oxide samples regardless of the preparation methods, whereas all the other methods gave origin to a solid solution of In_2O_3 and ZrO_2 with a cubic structure. This is not true for the urea hydrolysis method (hydro), which showed the formation of a different rhombohedral phase of In_2O_3, alongside the cubic solution, and a different morphology, of rods around 500 nm and some axial-layered agglomerate. In the In_2O_3-ZrO_2 series, the lower yield of methanol of the hydro sample, compared with the ammonia solution (ammo) and carbonate solution (carb) precipitation, might be related to the formation of the rhombohedral In_2O_3 phase.

Looking at parameters as surface area, porosity, CO_2 adsorption capabilities, and activity (STY, and X_{CO2}), the preparation methods are ranked in this order: comb < oxa (oxalate solution precipitation) < hydro < ammo < carb, with the only exception of $STY_{IZ\text{-}oxa}$, second only to $STY_{IZ\text{-}carb}$. This last catalyst showed 11.5 % conversion of CO_2, 4.2 % yield of CH_3OH at 300 °C, and a methanol STY of 108 mmol g_{In}^{-1} h^{-1}. The precipitation by using a carbonate solution as precipitating agent generated superior textural properties and remarkable activity. Finally, only the synthesis method using ammonia solution precipitation interestingly facilitates an In_2O_3 reduction at lower temperatures.

The loading of Pd was smaller than expected, for the urea hydro method, which turned out to be unsuitable: Pd most probably formed a stable and water-soluble complex of Pd and ammonia that hindered its precipitation. As expected, the introduction of ZrO_2 as a support by coprecipitation method is more than beneficial for the bulk In_2O_3. In some cases, In_2O_3-ZrO_2 also lowered the temperature at which the maximum yield of methanol was achieved. On the other hand, the loading Pd in the mixed oxide In_2O_3-ZrO_2 just had a limited effect among the tested samples due to the substantially narrow range distribution of the Pd loadings. IZ-hydro has better textural properties (0 wt.% of Pd loading) than the In_2O_3-ZrO_2-Pd samples, which showed this trend: IZP-1.0 ≈ IZP-0.25 < IZP-0.50 < IZ-hydro. Despite this, the STY of methanol improved with the Pd loading: IZ-hydro ≈ IZP-1.0 < IZP-0.25 < IZP-0.50. IZP-0.50

had very promising performances compared to literature and excellent stability in a 20h-TOS stability test. The best performance of IZP-0.50 is perhaps related to three main factors including high specific surface area, ease of reduction, and its optimum Pd cluster size compared to IZP-1.0. All three Pd-containing samples showed a reduction at lower temperatures, possibly attributed to the reduction of either PdO or the surface In_2O_3.

For the spent catalysts we observed an overall increase in the crystallite size, except for IZ-carb and IZP-0.50, while the surface area decreased by almost half of the original value.

Bibliography

(1) United Nations. UN Sustainable Development Goals https://sdgs.un.org/ (accessed 2021 -11 -02).

(2) UNFCCC. *Conference of the Parties (COP): Adoption of the Paris Agreement. Proposal by the President*; Geneva, Switzerland, 2015.

(3) Walsh, B.; Ciais, P.; Janssens, I. A.; Peñuelas, J.; Riahi, K.; Rydzak, F.; van Vuuren, D. P.; Obersteiner, M. Pathways for Balancing CO2 Emissions and Sinks. *Nature Communications* **2017**, *8* (1), 14856. https://doi.org/10.1038/ncomms14856.

(4) Centi, G.; Perathoner, S. CO2-Based Energy Vectors for the Storage of Solar Energy. *Greenhouse Gases: Science and Technology* **2011**, *1* (1), 21–35. https://doi.org/https://doi.org/10.1002/ghg3.3.

(5) Lovelock, C. E.; Duarte, C. M. Dimensions of Blue Carbon and Emerging Perspectives. *Biology Letters* **2019**, *15* (3), 20180781. https://doi.org/10.1098/rsbl.2018.0781.

(6) Friedlingstein, P.; Cox, P.; Betts, R.; Bopp, L.; von Bloh, W.; Brovkin, V.; Cadule, P.; Doney, S.; Eby, M.; Fung, I.; Bala, G.; John, J.; Jones, C.; Joos, F.; Kato, T.; Kawamiya, M.; Knorr, W.; Lindsay, K.; Matthews, H. D.; Raddatz, T.; Rayner, P.; Reick, C.; Roeckner, E.; Schnitzler, K.-G.; Schnur, R.; Strassmann, K.; Weaver, A. J.; Yoshikawa, C.; Zeng, N. Climate–Carbon Cycle Feedback Analysis: Results from the C4MIP Model Intercomparison. *Journal of Climate* **2006**, *19* (14), 3337–3353. https://doi.org/10.1175/JCLI3800.1.

(7) De, S.; Dokania, A.; Ramirez, A.; Gascon, J. Advances in the Design of Heterogeneous Catalysts and Thermocatalytic Processes for CO2 Utilization. *ACS Catalysis* **2020**, *10* (23), 14147–14185. https://doi.org/10.1021/acscatal.0c04273.

(8) Rahman, F. A.; Aziz, M. M. A.; Saidur, R.; Bakar, W. A. W. A.; Hainin, M. R.; Putrajaya, R.; Hassan, N. A. Pollution to Solution: Capture and Sequestration of Carbon Dioxide (CO2) and Its Utilization as a Renewable Energy Source for a Sustainable Future. *Renewable and Sustainable Energy Reviews* **2017**, *71*, 112–126. https://doi.org/https://doi.org/10.1016/j.rser.2017.01.011.

(9) mac Dowell, N.; Fennell, P. S.; Shah, N.; Maitland, G. C. The Role of CO2 Capture and Utilization in Mitigating Climate Change. *Nature Climate Change* **2017**, *7* (4), 243–249. https://doi.org/10.1038/nclimate3231.

(10) Centi, G.; Quadrelli, E. A.; Perathoner, S. Catalysis for CO2 Conversion: A Key Technology for Rapid Introduction of Renewable Energy in the Value Chain of Chemical Industries. *Energy & Environmental Science* **2013**, *6* (6), 1711–1731. https://doi.org/10.1039/C3EE00056G.

(11) Navarro, R. M.; Peña, M. A.; Fierro, J. L. G. Hydrogen Production Reactions from Carbon Feedstocks: Fossil Fuels and Biomass. *Chemical Reviews* **2007**, *107* (10), 3952–3991. https://doi.org/10.1021/cr0501994.

(12) Dincer, I.; Acar, C. Review and Evaluation of Hydrogen Production Methods for Better Sustainability. *International Journal of Hydrogen Energy* **2015**, *40* (34), 11094–11111. https://doi.org/https://doi.org/10.1016/j.ijhydene.2014.12.035.

(13) Zhao, G.; Huang, X.; Wang, X.; Wang, X. Progress in Catalyst Exploration for Heterogeneous CO2 Reduction and Utilization: A Critical Review. *Journal of Materials Chemistry A* **2017**, *5* (41), 21625–21649. https://doi.org/10.1039/C7TA07290B.

(14) Roy, S.; Cherevotan, A.; Peter, S. C. Thermochemical CO2 Hydrogenation to Single Carbon Products: Scientific and Technological Challenges. *ACS Energy Letters* **2018**, *3* (8), 1938–1966. https://doi.org/10.1021/acsenergylett.8b00740.

(15) Zheng, T.; Jiang, K.; Wang, H. Recent Advances in Electrochemical CO2-to-CO Conversion on Heterogeneous Catalysts. *Advanced Materials* **2018**, *30* (48), 1802066. https://doi.org/https://doi.org/10.1002/adma.201802066.

(16) Jiang, X.; Nie, X.; Guo, X.; Song, C.; Chen, J. G. Recent Advances in Carbon Dioxide Hydrogenation to Methanol via Heterogeneous Catalysis. *Chemical Reviews* **2020**, *120* (15), 7984–8034. https://doi.org/10.1021/acs.chemrev.9b00723.

(17) Zhong, J.; Yang, X.; Wu, Z.; Liang, B.; Huang, Y.; Zhang, T. State of the Art and Perspectives in Heterogeneous Catalysis of CO2 Hydrogenation to Methanol. *Chemical Society Reviews* **2020**, *49* (5), 1385–1413. https://doi.org/10.1039/C9CS00614A.

(18) Ye, R.-P.; Ding, J.; Gong, W.; Argyle, M. D.; Zhong, Q.; Wang, Y.; Russell, C. K.; Xu, Z.; Russell, A. G.; Li, Q.; Fan, M.; Yao, Y.-G. CO2 Hydrogenation to High-Value

Products via Heterogeneous Catalysis. *Nature Communications* **2019**, *10* (1), 5698. https://doi.org/10.1038/s41467-019-13638-9.

(19) IEA. The Future of Petrochemicals https://www.iea.org/reports/the-future-of-petrochemicals (accessed 2021 -11 -29).

(20) The Methanol Institute. The Methanol Institute https://www.methanol.org/ (accessed 2021 -11 -30).

(21) Lucía Fernández. Production capacity of methanol worldwide from 2018 to 2020, with a forecast for 2030 https://www.statista.com/statistics/1065891/global-methanol-production-capacity/ (accessed 2021 -11 -30).

(22) Räuchle, K.; Plass, L.; Wernicke, H.-J.; Bertau, M. Methanol for Renewable Energy Storage and Utilization. *Energy Technology* **2016**, *4* (1), 193–200. https://doi.org/https://doi.org/10.1002/ente.201500322.

(23) Álvarez, A.; Bansode, A.; Urakawa, A.; Bavykina, A. v; Wezendonk, T. A.; Makkee, M.; Gascon, J.; Kapteijn, F. Challenges in the Greener Production of Formates/Formic Acid, Methanol, and DME by Heterogeneously Catalyzed CO2 Hydrogenation Processes. *Chemical Reviews* **2017**, *117* (14), 9804–9838. https://doi.org/10.1021/acs.chemrev.6b00816.

(24) Song, J.; Liu, S.; Yang, C.; Wang, G.; Tian, H.; Zhao, Z.; Mu, R.; Gong, J. The Role of Al Doping in Pd/ZnO Catalyst for CO2 Hydrogenation to Methanol. *Applied Catalysis B: Environmental* **2020**, *263*, 118367. https://doi.org/https://doi.org/10.1016/j.apcatb.2019.118367.

(25) Behrens, M.; Schlögl, R. How to Prepare a Good Cu/ZnO Catalyst or the Role of Solid State Chemistry for the Synthesis of Nanostructured Catalysts. *Zeitschrift für anorganische und allgemeine Chemie* **2013**, *639* (15), 2683–2695. https://doi.org/https://doi.org/10.1002/zaac.201300356.

(26) Roode-Gutzmer, Q. I.; Kaiser, D.; Bertau, M. Renewable Methanol Synthesis. *ChemBioEng Reviews* **2019**, *6* (6), 209–236. https://doi.org/https://doi.org/10.1002/cben.201900012.

(27) Stangeland, K.; Li, H.; Yu, Z. Thermodynamic Analysis of Chemical and Phase Equilibria in CO2 Hydrogenation to Methanol, Dimethyl Ether, and Higher Alcohols.

Industrial & Engineering Chemistry Research **2018**, *57* (11), 4081–4094. https://doi.org/10.1021/acs.iecr.7b04866.

(28) Kunkes, E. L.; Studt, F.; Abild-Pedersen, F.; Schlögl, R.; Behrens, M. Hydrogenation of CO2 to Methanol and CO on Cu/ZnO/Al2O3: Is There a Common Intermediate or Not? *Journal of Catalysis* **2015**, *328*, 43–48. https://doi.org/https://doi.org/10.1016/j.jcat.2014.12.016.

(29) Liang, B.; Ma, J.; Su, X.; Yang, C.; Duan, H.; Zhou, H.; Deng, S.; Li, L.; Huang, Y. Investigation on Deactivation of Cu/ZnO/Al2O3 Catalyst for CO2 Hydrogenation to Methanol. *Industrial & Engineering Chemistry Research* **2019**, *58* (21), 9030–9037. https://doi.org/10.1021/acs.iecr.9b01546.

(30) Makertiharta, I. G. B. N.; Dharmawijaya, P. T.; Wenten, I. G. Current Progress on Zeolite Membrane Reactor for CO2 Hydrogenation. *AIP Conference Proceedings* **2017**, *1788* (1), 040001. https://doi.org/10.1063/1.4968389.

(31) Studt, F.; Sharafutdinov, I.; Abild-Pedersen, F.; Elkjær, C. F.; Hummelshøj, J. S.; Dahl, S.; Chorkendorff, I.; Nørskov, J. K. Discovery of a Ni-Ga Catalyst for Carbon Dioxide Reduction to Methanol. *Nature Chemistry* **2014**, *6* (4), 320–324. https://doi.org/10.1038/nchem.1873.

(32) Bavykina, A.; Yarulina, I.; al Abdulghani, A. J.; Gevers, L.; Hedhili, M. N.; Miao, X.; Galilea, A. R.; Pustovarenko, A.; Dikhtiarenko, A.; Cadiau, A.; Aguilar-Tapia, A.; Hazemann, J.-L.; Kozlov, S. M.; Oud-Chikh, S.; Cavallo, L.; Gascon, J. Turning a Methanation Co Catalyst into an In–Co Methanol Producer. *ACS Catalysis* **2019**, *9* (8), 6910–6918. https://doi.org/10.1021/acscatal.9b01638.

(33) Malik, A. S.; Zaman, S. F.; Al-Zahrani, A. A.; Daous, M. A.; Driss, H.; Petrov, L. A. Development of Highly Selective PdZn/CeO2 and Ca-Doped PdZn/CeO2 Catalysts for Methanol Synthesis from CO2 Hydrogenation. *Applied Catalysis A: General* **2018**, *560*, 42–53. https://doi.org/https://doi.org/10.1016/j.apcata.2018.04.036.

(34) Jiang, X.; Nie, X.; Wang, X.; Wang, H.; Koizumi, N.; Chen, Y.; Guo, X.; Song, C. Origin of Pd-Cu Bimetallic Effect for Synergetic Promotion of Methanol Formation from CO2 Hydrogenation. *Journal of Catalysis* **2019**, *369*, 21–32. https://doi.org/https://doi.org/10.1016/j.jcat.2018.10.001.

(35) Wang, J.; Zhang, G.; Zhu, J.; Zhang, X.; Ding, F.; Zhang, A.; Guo, X.; Song, C. CO2 Hydrogenation to Methanol over In2O3-Based Catalysts: From Mechanism to Catalyst Development. *ACS Catalysis* **2021**, *11* (3), 1406–1423. https://doi.org/10.1021/acscatal.0c03665.

(36) Collins, S. E.; Chiavassa, D. L.; Bonivardi, A. L.; Baltanás, M. A. Hydrogen Spillover in Ga2O3–Pd/SiO2 Catalysts for Methanol Synthesis from CO2/H2. *Catalysis Letters* **2005**, *103* (1), 83–88. https://doi.org/10.1007/s10562-005-6507-5.

(37) Yang, S.-C.; Pang, S. H.; Sulmonetti, T. P.; Su, W.-N.; Lee, J.-F.; Hwang, B.-J.; Jones, C. W. Synergy between Ceria Oxygen Vacancies and Cu Nanoparticles Facilitates the Catalytic Conversion of CO2 to CO under Mild Conditions. *ACS Catalysis* **2018**, *8* (12), 12056–12066. https://doi.org/10.1021/acscatal.8b04219.

(38) Roode-Gutzmer, Q. I.; Kaiser, D.; Bertau, M. Renewable Methanol Synthesis. *ChemBioEng Reviews* **2019**, *6* (6), 209–236. https://doi.org/https://doi.org/10.1002/cben.201900012.

(39) Kattel, S.; Yan, B.; Chen, J. G.; Liu, P. CO2 Hydrogenation on Pt, Pt/SiO2 and Pt/TiO2: Importance of Synergy between Pt and Oxide Support. *Journal of Catalysis* **2016**, *343*, 115–126. https://doi.org/https://doi.org/10.1016/j.jcat.2015.12.019.

(40) Yang, X.; Kattel, S.; Senanayake, S. D.; Boscoboinik, J. A.; Nie, X.; Graciani, J.; Rodriguez, J. A.; Liu, P.; Stacchiola, D. J.; Chen, J. G. Low Pressure CO2 Hydrogenation to Methanol over Gold Nanoparticles Activated on a CeOx/TiO2 Interface. *Journal of the American Chemical Society* **2015**, *137* (32), 10104–10107. https://doi.org/10.1021/jacs.5b06150.

(41) Frei, M. S.; Mondelli, C.; Cesarini, A.; Krumeich, F.; Hauert, R.; Stewart, J. A.; Curulla Ferré, D.; Pérez-Ramírez, J. Role of Zirconia in Indium Oxide-Catalyzed CO2 Hydrogenation to Methanol. *ACS Catalysis* **2020**, *10* (2), 1133–1145. https://doi.org/10.1021/acscatal.9b03305.

(42) Martin, O.; Martín, A. J.; Mondelli, C.; Mitchell, S.; Segawa, T. F.; Hauert, R.; Drouilly, C.; Curulla-Ferré, D.; Pérez-Ramírez, J. Indium Oxide as a Superior Catalyst for Methanol Synthesis by CO2 Hydrogenation. *Angewandte Chemie International Edition* **2016**, *55* (21), 6261–6265. https://doi.org/https://doi.org/10.1002/anie.201600943.

(43) Sun, K.; Fan, Z.; Ye, J.; Yan, J.; Ge, Q.; Li, Y.; He, W.; Yang, W.; Liu, C. Hydrogenation of CO2 to Methanol over In2O3 Catalyst. *Journal of CO2 Utilization* **2015**, *12*, 1–6. https://doi.org/https://doi.org/10.1016/j.jcou.2015.09.002.

(44) Dou, M.; Zhang, M.; Chen, Y.; Yu, Y. Theoretical Study of Methanol Synthesis from CO2 and CO Hydrogenation on the Surface of ZrO2 Supported In2O3 Catalyst. *Surface Science* **2018**, *672–673*, 7–12. https://doi.org/https://doi.org/10.1016/j.susc.2018.02.013.

(45) Rui, N.; Wang, Z.; Sun, K.; Ye, J.; Ge, Q.; Liu, C. CO2 Hydrogenation to Methanol over Pd/In2O3: Effects of Pd and Oxygen Vacancy. *Applied Catalysis B: Environmental* **2017**, *218*, 488–497. https://doi.org/https://doi.org/10.1016/j.apcatb.2017.06.069.

(46) Wu, P.; Yang, B. Intermetallic PdIn Catalyst for CO2 Hydrogenation to Methanol: Mechanistic Studies with a Combined DFT and Microkinetic Modeling Method. *Catalysis Science & Technology* **2019**, *9* (21), 6102–6113. https://doi.org/10.1039/C9CY01242G.

(47) Tsoukalou, A.; Abdala, P. M.; Armutlulu, A.; Willinger, E.; Fedorov, A.; Müller, C. R. Operando X-Ray Absorption Spectroscopy Identifies a Monoclinic ZrO2:In Solid Solution as the Active Phase for the Hydrogenation of CO2 to Methanol. *ACS Catalysis* **2020**, *10* (17), 10060–10067. https://doi.org/10.1021/acscatal.0c01968.

(48) Porosoff, M. D.; Yan, B.; Chen, J. G. Catalytic Reduction of CO2 by H2 for Synthesis of CO, Methanol and Hydrocarbons: Challenges and Opportunities. *Energy & Environmental Science* **2016**, *9* (1), 62–73. https://doi.org/10.1039/C5EE02657A.

(49) Ye, J.; Liu, C.; Mei, D.; Ge, Q. Active Oxygen Vacancy Site for Methanol Synthesis from CO2 Hydrogenation on In2O3(110): A DFT Study. *ACS Catalysis* **2013**, *3* (6), 1296–1306. https://doi.org/10.1021/cs400132a.

(50) Wang, W.; Zhang, Y.; Wang, Z.; Yan, J.; Ge, Q.; Liu, C. Reverse Water Gas Shift over In2O3–CeO2 Catalysts. *Catalysis Today* **2016**, *259*, 402–408. https://doi.org/https://doi.org/10.1016/j.cattod.2015.04.032.

(51) Sun, Q.; Ye, J.; Liu, C.; Ge, Q. In2O3 as a Promising Catalyst for CO2 Utilization: A Case Study with Reverse Water Gas Shift over In2O3. *Greenhouse Gases: Science and Technology* **2014**, *4* (1), 140–144. https://doi.org/https://doi.org/10.1002/ghg.1401.

(52) Dang, S.; Gao, P.; Liu, Z.; Chen, X.; Yang, C.; Wang, H.; Zhong, L.; Li, S.; Sun, Y. Role of Zirconium in Direct CO2 Hydrogenation to Lower Olefins on Oxide/Zeolite Bifunctional Catalysts. *Journal of Catalysis* **2018**, *364*, 382–393. https://doi.org/https://doi.org/10.1016/j.jcat.2018.06.010.

(53) Chuasiripattana, K.; Warschkow, O.; Delley, B.; Stampfl, C. Reaction Intermediates of Methanol Synthesis and the Water–Gas-Shift Reaction on the ZnO(0001) Surface. *Surface Science* **2010**, *604* (19), 1742–1751. https://doi.org/https://doi.org/10.1016/j.susc.2010.06.025.

(54) Álvarez, A.; Borges, M.; Corral-Pérez, J. J.; Olcina, J. G.; Hu, L.; Cornu, D.; Huang, R.; Stoian, D.; Urakawa, A. CO2 Activation over Catalytic Surfaces. *ChemPhysChem* **2017**, *18* (22), 3135–3141. https://doi.org/https://doi.org/10.1002/cphc.201700782.

(55) Chen, T.; Cao, C.; Chen, T.; Ding, X.; Huang, H.; Shen, L.; Cao, X.; Zhu, M.; Xu, J.; Gao, J.; Han, Y.-F. Unraveling Highly Tunable Selectivity in CO2 Hydrogenation over Bimetallic In-Zr Oxide Catalysts. *ACS Catalysis* **2019**, *9* (9), 8785–8797. https://doi.org/10.1021/acscatal.9b01869.

(56) Frei, M. S.; Capdevila-Cortada, M.; García-Muelas, R.; Mondelli, C.; López, N.; Stewart, J. A.; Curulla Ferré, D.; Pérez-Ramírez, J. Mechanism and Microkinetics of Methanol Synthesis via CO2 Hydrogenation on Indium Oxide. *Journal of Catalysis* **2018**, *361*, 313–321. https://doi.org/https://doi.org/10.1016/j.jcat.2018.03.014.

(57) Dou, M.; Zhang, M.; Chen, Y.; Yu, Y. DFT Study of In2O3-Catalyzed Methanol Synthesis from CO2 and CO Hydrogenation on the Defective Site. *New Journal of Chemistry* **2018**, *42* (5), 3293–3300. https://doi.org/10.1039/C7NJ04273F.

(58) Tsoukalou, A.; Abdala, P. M.; Stoian, D.; Huang, X.; Willinger, M.-G.; Fedorov, A.; Müller, C. R. Structural Evolution and Dynamics of an In2O3 Catalyst for CO2 Hydrogenation to Methanol: An Operando XAS-XRD and In Situ TEM Study. *Journal of the American Chemical Society* **2019**, *141* (34), 13497–13505. https://doi.org/10.1021/jacs.9b04873.

(59) Li, K.; Chen, J. G. CO2 Hydrogenation to Methanol over ZrO2-Containing Catalysts: Insights into ZrO2 Induced Synergy. *ACS Catalysis* **2019**, *9* (9), 7840–7861. https://doi.org/10.1021/acscatal.9b01943.

(60) Gao, P.; Dang, S.; Li, S.; Bu, X.; Liu, Z.; Qiu, M.; Yang, C.; Wang, H.; Zhong, L.; Han, Y.; Liu, Q.; Wei, W.; Sun, Y. Direct Production of Lower Olefins from CO2 Conversion via Bifunctional Catalysis. *ACS Catalysis* **2018**, *8* (1), 571–578. https://doi.org/10.1021/acscatal.7b02649.

(61) Zhang, M.; Dou, M.; Yu, Y. Theoretical Study of the Promotional Effect of ZrO2 on In2O3 Catalyzed Methanol Synthesis from CO2 Hydrogenation. *Applied Surface Science* **2018**, *433*, 780–789. https://doi.org/https://doi.org/10.1016/j.apsusc.2017.10.097.

(62) Thomas, J. M. Handbook Of Heterogeneous Catalysis. 2., Completely Revised and Enlarged Edition. Vol. 1–8. Edited by G. Ertl, H. Knözinger, F. Schüth, and J. Weitkamp. *Angewandte Chemie International Edition* **2009**, *48* (19), 3390–3391. https://doi.org/https://doi.org/10.1002/anie.200901598.

(63) Poutsma, M. L.; Elek, L. F.; Ibarbia, P. A.; Risch, A. P.; Rabo, J. A. Selective Formation of Methanol from Synthesis Gas over Palladium Catalysts. *Journal of Catalysis* **1978**, *52* (1), 157–168. https://doi.org/https://doi.org/10.1016/0021-9517(78)90131-8.

(64) Matsumura, Y.; Shen, W.-J.; Ichihashi, Y.; Okumura, M. Low-Temperature Methanol Synthesis Catalyzed over Ultrafine Palladium Particles Supported on Cerium Oxide. *Journal of Catalysis* **2001**, *197* (2), 267–272. https://doi.org/https://doi.org/10.1006/jcat.2000.3094.

(65) Snider, J. L.; Streibel, V.; Hubert, M. A.; Choksi, T. S.; Valle, E.; Upham, D. C.; Schumann, J.; Duyar, M. S.; Gallo, A.; Abild-Pedersen, F.; Jaramillo, T. F. Revealing the Synergy between Oxide and Alloy Phases on the Performance of Bimetallic In–Pd Catalysts for CO2 Hydrogenation to Methanol. *ACS Catalysis* **2019**, *9* (4), 3399–3412. https://doi.org/10.1021/acscatal.8b04848.

(66) Frei, M. S.; Mondelli, C.; García-Muelas, R.; Kley, K. S.; Puértolas, B.; López, N.; Safonova, O. v; Stewart, J. A.; Curulla Ferré, D.; Pérez-Ramírez, J. Atomic-Scale Engineering of Indium Oxide Promotion by Palladium for Methanol Production via CO2 Hydrogenation. *Nature Communications* **2019**, *10* (1), 3377. https://doi.org/10.1038/s41467-019-11349-9.

(67) Jiang, H.; Lin, J.; Wu, X.; Wang, W.; Chen, Y.; Zhang, M. Efficient Hydrogenation of CO2 to Methanol over Pd/In2O3/SBA-15 Catalysts. *Journal of CO2 Utilization* **2020**, *36*, 33–39. https://doi.org/https://doi.org/10.1016/j.jcou.2019.10.013.

(68) Rui, N.; Zhang, F.; Sun, K.; Liu, Z.; Xu, W.; Stavitski, E.; Senanayake, S. D.; Rodriguez, J. A.; Liu, C.-J. Hydrogenation of CO2 to Methanol on a Auδ+–In2O3–x Catalyst. *ACS Catalysis* **2020**, *10* (19), 11307–11317. https://doi.org/10.1021/acscatal.0c02120.

(69) Shen, C.; Sun, K.; Zhang, Z.; Rui, N.; Jia, X.; Mei, D.; Liu, C. Highly Active Ir/In2O3 Catalysts for Selective Hydrogenation of CO2 to Methanol: Experimental and Theoretical Studies. *ACS Catalysis* **2021**, *11* (7), 4036–4046. https://doi.org/10.1021/acscatal.0c05628.

(70) Han, Z.; Tang, C.; Wang, J.; Li, L.; Li, C. Atomically Dispersed Ptn+ Species as Highly Active Sites in Pt/In2O3 Catalysts for Methanol Synthesis from CO2 Hydrogenation. *Journal of Catalysis* **2021**, *394*, 236–244. https://doi.org/https://doi.org/10.1016/j.jcat.2020.06.018.

(71) Dostagir, N. H. M. D.; Thompson, C.; Kobayashi, H.; Karim, A. M.; Fukuoka, A.; Shrotri, A. Rh Promoted In2O3 as a Highly Active Catalyst for CO2 Hydrogenation to Methanol. *Catalysis Science & Technology* **2020**, *10* (24), 8196–8202. https://doi.org/10.1039/D0CY01789B.

(72) García-Trenco, A.; Regoutz, A.; White, E. R.; Payne, D. J.; Shaffer, M. S. P.; Williams, C. K. PdIn Intermetallic Nanoparticles for the Hydrogenation of CO2 to Methanol. *Applied Catalysis B: Environmental* **2018**, *220*, 9–18. https://doi.org/https://doi.org/10.1016/j.apcatb.2017.07.069.

(73) Karazhanov, S. Zh.; Ravindran, P.; Vajeeston, P.; Ulyashin, A.; Finstad, T. G.; Fjellvåg, H. Phase Stability, Electronic Structure, and Optical Properties of Indium Oxide Polytypes. *Physical Review B* **2007**, *76* (7), 75129. https://doi.org/10.1103/PhysRevB.76.075129.

(74) Ye, J.; Ge, Q.; Liu, C. Effect of PdIn Bimetallic Particle Formation on CO2 Reduction over the Pd–In/SiO2 Catalyst. *Chemical Engineering Science* **2015**, *135*, 193–201. https://doi.org/https://doi.org/10.1016/j.ces.2015.04.034.

(75) Gurlo, A.; Kroll, P.; Riedel, R. Metastability of Corundum-Type In2O3. *Chemistry – A European Journal* **2008**, *14* (11), 3306–3310. https://doi.org/https://doi.org/10.1002/chem.200701830.

(76) Liu, D.; Lei, W. W.; Zou, B.; Yu, S. D.; Hao, J.; Wang, K.; Liu, B. B.; Cui, Q. L.; Zou, G. T. High-Pressure x-Ray Diffraction and Raman Spectra Study of Indium Oxide. *Journal of Applied Physics* **2008**, *104* (8), 083506. https://doi.org/10.1063/1.2999369.

(77) Wang, J.; Liu, C.-Y.; Senftle, T. P.; Zhu, J.; Zhang, G.; Guo, X.; Song, C. Variation in the In2O3 Crystal Phase Alters Catalytic Performance toward the Reverse Water Gas Shift Reaction. *ACS Catalysis* **2020**, *10* (5), 3264–3273. https://doi.org/10.1021/acscatal.9b04239.

(78) Shanshan, D.; Bin, Q.; Yong, Y.; Hui, W.; Jun, C.; Yong, H.; Shenggang, L.; Peng, G.; Yuhan, S. Rationally Designed Indium Oxide Catalysts for CO2 Hydrogenation to Methanol with High Activity and Selectivity. *Science Advances* **2021**, *6* (25), eaaz2060. https://doi.org/10.1126/sciadv.aaz2060.

(79) Shi, Z.; Tan, Q.; Wu, D. Mixed-Phase Indium Oxide as a Highly Active and Stable Catalyst for the Hydrogenation of CO2 to CH3OH. *Industrial & Engineering Chemistry Research* **2021**, *60* (9), 3532–3542. https://doi.org/10.1021/acs.iecr.0c04688.

(80) Bachiller-Baeza, B.; Rodriguez-Ramos, I.; Guerrero-Ruiz, A. Interaction of Carbon Dioxide with the Surface of Zirconia Polymorphs. *Langmuir* **1998**, *14* (13), 3556–3564. https://doi.org/10.1021/la970856q.

(81) Morterra, C.; Orio, L. Surface Characterization of Zirconium Oxide. II. The Interaction with Carbon Dioxide at Ambient Temperature. *Materials Chemistry and Physics* **1990**, *24* (3), 247–268. https://doi.org/https://doi.org/10.1016/0254-0584(90)90089-S.

(82) Gao, P.; Li, S.; Bu, X.; Dang, S.; Liu, Z.; Wang, H.; Zhong, L.; Qiu, M.; Yang, C.; Cai, J.; Wei, W.; Sun, Y. Direct Conversion of CO2 into Liquid Fuels with High Selectivity over a Bifunctional Catalyst. *Nature Chemistry* **2017**, *9* (10), 1019–1024. https://doi.org/10.1038/nchem.2794.

(83) Wang, J.; Tang, C.; Li, G.; Han, Z.; Li, Z.; Liu, H.; Cheng, F.; Li, C. High-Performance MaZrOx (Ma = Cd, Ga) Solid-Solution Catalysts for CO2 Hydrogenation to Methanol. *ACS Catalysis* **2019**, *9* (11), 10253–10259. https://doi.org/10.1021/acscatal.9b03449.

(84) Pavese, M.; Biamino, S. Mesoporous Alumina Obtained by Combustion Synthesis without Template. *Journal of Porous Materials* **2009**, *16* (1), 59–64. https://doi.org/10.1007/s10934-007-9168-5.

(85) Chen, H.; Yin, A.; Guo, X.; Dai, W.-L.; Fan, K.-N. Sodium Hydroxide–Sodium Oxalate-Assisted Co-Precipitation of Highly Active and Stable Cu/ZrO2 Catalyst in the Partial Oxidation of Methanol to Hydrogen. *Catalysis Letters* **2009**, *131* (3), 632–642. https://doi.org/10.1007/s10562-009-0008-x.

(86) Behrens, M.; Schlögl, R. How to Prepare a Good Cu/ZnO Catalyst or the Role of Solid State Chemistry for the Synthesis of Nanostructured Catalysts. *Zeitschrift für anorganische und allgemeine Chemie* **2013**, *639* (15), 2683–2695. https://doi.org/https://doi.org/10.1002/zaac.201300356.

(87) Lee, H.-C. Review of Inductively Coupled Plasmas: Nano-Applications and Bistable Hysteresis Physics. *Applied Physics Reviews* **2018**, *5* (1), 011108. https://doi.org/10.1063/1.5012001.

(88) Dutrow, B. L. X-ray Powder Diffraction (XRD) https://serc.carleton.edu/research_education/geochemsheets/techniques/XRD.html (accessed 2021 -10 -25).

(89) Kuhlmann, K. Development and Commissioning of a Prototype Neutron Backscattering Spectrometer with an Energy Resolution Enhanced by an Order of Magnitude Using GaAs Single Crystals, Erlangen, Germany, 2018.

(90) Wikipedia. Scanning electron microscope https://en.wikipedia.org/wiki/Scanning_electron_microscope#cite_note-Stokes-1 (accessed 2021 -11 -15).

(91) McMullan, D. Scanning Electron Microscopy 1928–1965. *Scanning* **1995**, *17* (3), 175–185. https://doi.org/https://doi.org/10.1002/sca.4950170309.

(92) Brunauer, S.; Emmett, P. H.; Teller, E. Adsorption of Gases in Multimolecular Layers. *Journal of the American Chemical Society* **1938**, *60* (2), 309–319. https://doi.org/10.1021/ja01269a023.

(93) Fan, M.; Fu, F. *Advanced High Strength Natural Fibre Composites in Construction*; Elsevier Science, Wodhead Publishing, 2016.

(94) Centre National de la Recherche Scientifique (CNRS). XPS: X-ray Photoelectron Spectroscopy http://www.lasurface.com/xps/index.php (accessed 2021 -11 -16).

(95) Wikipedia. X-ray Photoelectron Spectroscopy https://en.wikipedia.org/wiki/X-ray_photoelectron_spectroscopy (accessed 2021 -11 -16).

(96) Ishii, T.; Kyotani, T. Chapter 14 - Temperature Programmed Desorption. In *Materials Science and Engineering of Carbon*; Inagaki, M., Kang, F., Eds.; Butterworth-Heinemann, 2016; pp 287–305. https://doi.org/https://doi.org/10.1016/B978-0-12-805256-3.00014-3.

(97) Hiden Analytical CATLAB-PCS. Temperature Programmed Reduction (TPR) - A Guide.

(98) Webb, P. A. *Introduction to Chemical Adsorption Analytical Techniques and Their Applications to Catalysis*; Norcross, Georgia, 2003.

(99) Canton, P.; Fagherazzi, G.; Battagliarin, M.; Menegazzo, F.; Pinna, F.; Pernicone, N. Pd/CO Average Chemisorption Stoichiometry in Highly Dispersed Supported Pd/γ-Al2O3 Catalysts. *Langmuir* **2002**, *18* (17), 6530–6535. https://doi.org/10.1021/la015650a.

(100) Mech, K.; Żabiński, P.; Kowalik, R.; Fitzner, K. Voltammetric Study of Electro-Reduction of Tetraamminepalladium(II) onto Gold Electrode. *Journal of Electroanalytical Chemistry* **2012**, *685*, 15–20. https://doi.org/https://doi.org/10.1016/j.jelechem.2012.08.035.

(101) Tsiotsias, A. I.; Charisiou, N. D.; Yentekakis, I. v; Goula, M. A. The Role of Alkali and Alkaline Earth Metals in the CO2 Methanation Reaction and the Combined Capture and Methanation of CO2. *Catalysts* **2020**, *10* (7). https://doi.org/10.3390/catal10070812.

(102) Numpilai, T.; Kidkhunthod, P.; Cheng, C. K.; Wattanakit, C.; Chareonpanich, M.; Limtrakul, J.; Witoon, T. CO2 Hydrogenation to Methanol at High Reaction Temperatures over In2O3/ZrO2 Catalysts: Influence of Calcination Temperatures of ZrO2 Support. *Catalysis Today* **2021**, *375*, 298–306. https://doi.org/https://doi.org/10.1016/j.cattod.2020.03.011.

(103) Shanshan, D.; Bin, Q.; Yong, Y.; Hui, W.; Jun, C.; Yong, H.; Shenggang, L.; Peng, G.; Yuhan, S. Rationally Designed Indium Oxide Catalysts for CO2 Hydrogenation to

Methanol with High Activity and Selectivity. *Science Advances* **2021**, *6* (25), eaaz2060. https://doi.org/10.1126/sciadv.aaz2060.

(104) Thommes, M.; Kaneko, K.; Neimark, A. v; Olivier, J. P.; Rodriguez-Reinoso, F.; Rouquerol, J.; Sing, K. S. W. Physisorption of Gases, with Special Reference to the Evaluation of Surface Area and Pore Size Distribution (IUPAC Technical Report). *Pure and Applied Chemistry* **2015**, *87* (9–10), 1051–1069. https://doi.org/doi:10.1515/pac-2014-1117.

(105) Salanov, A. N.; Suprun, E. A. Oxygen Desorption from Polycrystalline Palladium: Thermal Desorption of O2 from a Chemisorbed Layer of Oads in the Course of the Decomposition of PdO Surface Oxide and in the Release of Oxygen from the Bulk of Palladium. *Kinetics and Catalysis* **2010**, *51* (3), 416–427. https://doi.org/10.1134/S0023158410030158.

(106) Letichevsky, S.; Zonetti, P. C.; Reis, P. P. P.; Celnik, J.; Rabello, C. R. K.; Gaspar, A. B.; Appel, L. G. The Role of M-ZrO2 in the Selective Oxidation of Ethanol to Acetic Acid Employing PdO/m-ZrO2. *Journal of Molecular Catalysis A: Chemical* **2015**, *410*, 177–183. https://doi.org/https://doi.org/10.1016/j.molcata.2015.09.012.

(107) Chou, C.-Y.; Lobo, R. F. Direct Conversion of CO2 into Methanol over Promoted Indium Oxide-Based Catalysts. *Applied Catalysis A: General* **2019**, *583*, 117144. https://doi.org/https://doi.org/10.1016/j.apcata.2019.117144.

(108) Vogt, C.; Monai, M.; Kramer, G. J.; Weckhuysen, B. M. The Renaissance of the Sabatier Reaction and Its Applications on Earth and in Space. *Nature Catalysis* **2019**, *2* (3), 188–197. https://doi.org/10.1038/s41929-019-0244-4.

(109) Ghosh, S.; Sebastian, J.; Olsson, L.; Creaser, D. Experimental and Kinetic Modeling Studies of Methanol Synthesis from CO2 Hydrogenation Using In2O3 Catalyst. *Chemical Engineering Journal* **2021**, *416*, 129120. https://doi.org/https://doi.org/10.1016/j.cej.2021.129120.

(110) Yang, B.; Li, L.; Jia, Z.; Liu, X.; Zhang, C.; Guo, L. Comparative Study of CO2 Hydrogenation to Methanol on Cubic Bixbyite-Type and Rhombohedral Corundum-Type Indium Oxide. *Chinese Chemical Letters* **2020**, *31* (10), 2627–2633. https://doi.org/https://doi.org/10.1016/j.cclet.2020.05.031.

(111) Mutschler, R.; Moioli, E.; Luo, W.; Gallandat, N.; Züttel, A. CO2 Hydrogenation Reaction over Pristine Fe, Co, Ni, Cu and Al2O3 Supported Ru: Comparison and Determination of the Activation Energies. *Journal of Catalysis* **2018**, *366*, 139–149. https://doi.org/https://doi.org/10.1016/j.jcat.2018.08.002.

(112) Gao, P.; Zhang, L.; Li, S.; Zhou, Z.; Sun, Y. Novel Heterogeneous Catalysts for CO2 Hydrogenation to Liquid Fuels. *ACS Central Science* **2020**, *6* (10), 1657–1670. https://doi.org/10.1021/acscentsci.0c00976.

(113) Chen, P.; Tao, L.; Zhu, J.; Zhao, G.; Liu, Y.; Lu, Y. Morphology-Controllable Hexagonal-Phase Indium Oxide In Situ Structured onto a Thin-Felt Al2O3/Al-Fiber for the Hydrogenation of CO2 to Methanol. *Energy Technology* **2019**, *7* (3), 1800747. https://doi.org/https://doi.org/10.1002/ente.201800747.

(114) Regalado Vera, C. Y.; Manavi, N.; Zhou, Z.; Wang, L.-C.; Diao, W.; Karakalos, S.; Liu, B.; Stowers, K. J.; Zhou, M.; Luo, H.; Ding, D. Mechanistic Understanding of Support Effect on the Activity and Selectivity of Indium Oxide Catalysts for CO2 Hydrogenation. *Chemical Engineering Journal* **2021**, *426*, 131767. https://doi.org/https://doi.org/10.1016/j.cej.2021.131767.

Acknowledgments

I am eternally grateful to my parents and my brother, who have always looked after me, all my life, relentlessly, no matter what, no questions asked.

I would like to thank my supervisor Prof. Patricia Benito Martin for the opportunity that she gave me, her assistance, and, most important, her infinite patience.

Thanks should also go to all the research team that supervised me at Chalmers University for their guidance and unwavering support: Prof. Louise Olsson, Prof. Derek Creaser, Dr. Phuoc Hoang Ho, Dr. Sreetama Ghosh, and Dr. Wei Di. I would also like to extend my gratitude to the Swedish company Perstorp AB for supporting this thesis project.

Special thanks go to Phuoc, for being the best supervisor I could have asked for. I was fortunate enough to meet the most thoughtful researcher, the most patient teacher, and above all, a good friend.

I am extremely grateful to the Climate-KIC community, supported by the European Institute of Innovation and Technology (EIT), that alongside the University of Bologna, gave me the opportunity to enroll in the Climate-KIC curriculum of my Master’s degree Low Carbon Technologies and Sustainable Chemistry.

Finally, my gratitude goes to several friends, and more, who have always been there for me, with pieces of advice, laughs, and love, directly or indirectly helping me to complete this Master’s degree.

Thank you.

Giovanni Tizzanini